
3 Hydrate Formation and Dissociation Processes

The most challenging and intriguing questions regarding hydrates concern how hydrates form, dissociate, and are inhibited with time. The previous chapter provides the foundation required to understand these time-dependent processes. Time-dependent hydrate phenomena are substantially more challenging than time-independent phenomena of structure and thermodynamics. One can expect a decrease in accuracy of time-dependent measurements and models by at least one order of magnitude relative to their thermodynamic counterparts, as found in [Chapters 4 through 6](#).

Due to the difficulty of quantifying time-dependent phenomena, the present chapter deals with hydrate formation and dissociation in laboratory systems. The principles are extended to hydrate formation/dissociation/inhibition in pipelines in [Chapter 8](#) on hydrates in production, processing, and transportation. Dissociation in porous media, such as the assessment of gas evolution from *in situ* hydrate reserves using hydrate reservoir models is discussed in [Chapter 7](#) on hydrates in the earth. The present chapter is also restricted mostly to the time-dependent properties of structures I and II due to the limited time-dependent data on structure H. The experimental tools that have been applied to measure hydrate time-dependent phenomena are presented in Chapter 6.

The purpose of this chapter is to provide the reader with an understanding of time-dependent phenomena for the following:

1. Hydrate nucleation (Section 3.1), which is a *stochastic process*, describing
 - the knowledge base for hydrate nucleation (Section 3.1.1)
 - conceptual pictures of hydrate nucleation (Section 3.1.2)
 - the stochastic nature of heterogeneous nucleation (HEN) (Section 3.1.3)
 - correlations of nucleation (Section 3.1.4)
 - the memory effect phenomenon (Section 3.1.5)
 - the state-of-the-art for hydrate nucleation (Section 3.1.6)
2. Hydrate growth (Section 3.2), which may be controlled by kinetic, heat, and mass transfer limitations, describing
 - the conceptual picture of hydrate growth (Section 3.2.1)
 - crystal growth processes (Section 3.2.2)
 - correlations of growth, including models for intrinsic kinetics, and mass and heat transfer (Section 3.2.3)
 - the state-of-the-art for hydrate growth (Section 3.2.4)

3. Dissociation (Section 3.3), which is typically heat transfer limited with hydrate plug/cores generally dissociating radially, describing
 - the conceptual picture of hydrate dissociation (Section 3.3.1)
 - correlations of dissociation (Section 3.3.2)
 - the anomalous self-preservation phenomenon (Section 3.3.3)
 - the state-of-the-art for hydrate dissociation (Section 3.3.4)

Two questions of hydrate time-dependent phenomena are essential to both industry and researcher: (1) When will hydrates nucleate? (2) Once nucleated, how rapidly will hydrates grow or dissociate?

As an example of hydrate nucleation and growth, consider the gas consumption versus time trace in [Figure 3.1a](#) for an agitated system operated at constant pressure and temperature. An autoclave cell (e.g., 300 cm³) containing water (e.g., 150 cm³) is pressurized with gas and brought to hydrate formation (*P*, *T*) conditions. The gas is added from a reservoir to maintain *constant pressure* as hydrates form with time. The rate of consumption of gas is the hydrate formation rate that can be controlled by kinetics, or heat or mass transfer.

The induction time is marked as 1 and includes the time taken for crystal nuclei to form which are not visible to macroscopic probes. The induction time is defined in practice as the time elapsed until the appearance of a detectable volume of hydrate phase or, equivalently, until the consumption of a detectable number of moles of hydrate former gas. The induction time is often also termed the hydrate nucleation or lag time (Section 3.1). (The induction or lag time is the time taken for hydrates to be detected macroscopically, after nucleation and onset of growth have occurred, whereas nucleation occurs on too small a size scale to be detected. Therefore, the term nucleation time will not be used in this context. Instead, the term induction time or induction period will be used. The induction time is most likely to be dominated by the nucleation period, but also includes growth up to the point at which hydrates are first detected.)

During the induction period, the temperature and pressure conditions are within the hydrate stable region. However, hydrate does not form within this period because of metastability (i.e., the ability of a nonequilibrium state to persist for a long period of time). The growth period (in region 2) is where very rapid hydrate growth occurs (Section 3.2). During the growth period, gas is being concentrated in the hydrate cages—hydrated gas molecules are more densely packed than those in the vapor. As the water is consumed by hydrate formation, the slope of the gas consumption trace eventually decreases with time (Points 3–4). Hydrate dissociation is not shown in the figure.

An alternative hydrate formation and dissociation experiment is shown in the temperature and pressure trace of [Figure 3.1b](#). In this case, the volume is constant and the temperature is changed during the experiment. In the experimental apparatus an agitated autoclave cell (e.g., 300 cm³) housing a sight glass window contains water (e.g., 150 cm³) that is pressurized with methane gas to the upper

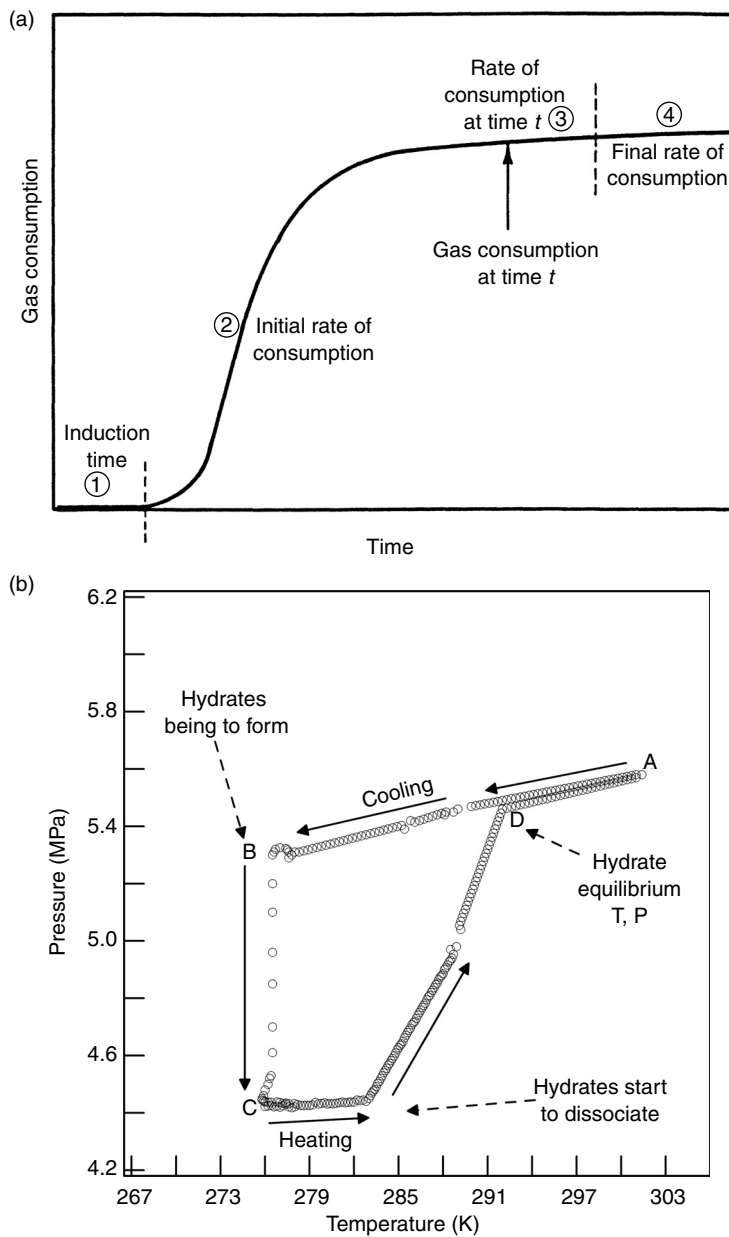


FIGURE 3.1 (a) Gas consumption vs. time for hydrate formation. (Reproduced from Lederhos, J.P., Long, J.P., Sum, A., Christiansen, R.L., Sloan, E.D., *Chem. Eng. Sci.*, **51**, 1221 (1996). With permission from Elsevier Science Ltd.) (b) Temperature and pressure trace for formation of simple methane hydrates. (Reproduced from Ouar, H., Cha, S.B., Wildeman, T.R., Sloan, E.D., *Trans I Chem. E.*, **70A**, 48 (1992). With permission from the American Chemical Society.)

rightmost temperature and pressure. As the cell temperature is lowered the pressure decreases, principally due to gas contraction as well as increased gas solubility upon cooling *at constant volume*. Neither gas nor water is added to the system during the experiment.

The metastability of the system prevents hydrate forming immediately at Point D (at the hydrate equilibrium temperature and pressure; [Figure 3.1b](#)). Instead the system pressure continues to decrease linearly with temperature for a number of hours, without hydrate formation occurring (A to B is the induction period, cf. 1 in [Figure 3.1a](#)). At Point B, hydrates begin to form. The pressure drops rapidly to Point C (about 1.01 MPa or 10 atm in 0.5 h). B to C is the catastrophic growth period (cf. 2 in [Figure 3.1a](#)).

Hydrate dissociation begins when the cell is heated from Point C in [Figure 3.1b](#), so that the system pressure increases, at first slowly and then sharply along the steep dissociation line (between Points C and D). Finally at Point D, the hydrates are completely dissociated, as confirmed visually through the sight glass. The hydrate equilibrium condition (or hydrate dissociation temperature and pressure) is given by Point D ([Section 3.3](#)).

Usually 1–2 days (for reactors on this scale) of experimental effort are required to traverse the loop as shown in [Figure 3.1b](#). In order to avoid obtaining an erroneous dissociation temperature and pressure, the dissociation part of the loop must be performed at a sufficiently slow heating rate (about 0.12 K/h) to allow the system to reach equilibrium (Tohidi et al., 2000; Rovetto et al., 2006). The temperature difference between the temperature at Point D to that at Point B is called the subcooling [more properly the supercooling, ΔT_{sub} , where $\Delta T_{\text{sub}} = T_{\text{eqm}}(\text{D}) - T(\text{B})$].

As illustrated in [Figure 3.1b](#), there is a fundamental difference in hydrate initiation and dissociation due to the associated gas and liquid phases being disorderly on a molecular level, while the hydrate crystals are orderly in nature. Entropy favors disorder over order, so the initial hydrate formation is hindered by a long, metastable period (induction period). During this period, the disorderly gas and liquid water begin to rearrange into the orderly hydrate crystal structure. Conversely, dissociation begins relatively rapidly after the hydrate is removed from the temperature and pressure stability region.

3.1 HYDRATE NUCLEATION

Hydrate nucleation is the process during which small clusters of water and gas (hydrate nuclei) grow and disperse in an attempt to achieve critical size for continued growth. The nucleation step is a microscopic phenomenon involving tens to thousands of molecules (Mullin, 1993, p. 173) and is difficult to observe experimentally. Current hypotheses for hydrate nucleation are based upon the better-known phenomena of water freezing, the dissolution of hydrocarbons in water, and computer simulations of both phenomena. Evidence from experiments shows that nucleation is a statistically probable (not deterministically certain; see [Section 3.1.3](#)) process.

3.1.1 Knowledge Base for Hydrate Nucleation

Nucleation thermodynamics were published by Ginns in 1928 based upon his work at the end of the last century. Volmer and Weber (1926) indicated that the growth and decay of clusters of molecules played a major role in nucleation kinetics. The most recent reviews of hydrate nucleation are by Kashchiev and Firoozabdi (2002a,b).

In order to achieve some understanding of the nucleation of hydrate crystals from supercooled water + gas systems, it is useful to briefly review the key properties of supercooled water (Section 3.1.1.1), hydrocarbon solubility in water (Section 3.1.1.2), and basic nucleation theory of ice, which can be applied to hydrates (since hydrate nucleation kinetics may be considered analogous, to some extent, to that of ice; Section 3.1.1.3). The three subsections of 3.1.1 (i.e., supercooled water, solubility of gas in water, and nucleation) are integral parts of conceptual pictures of nucleation detailed in Section 3.1.2.

3.1.1.1 Key properties of supercooled water

Water is considered to be supercooled when it exists as a liquid at lower temperatures than its melting point, for example, at less than 0°C at atmospheric pressure. In this state, the supercooled water is metastable. The properties of supercooled water have been examined in detail in excellent reviews by Angell (1982, 1983) and Debenedetti (1996, 2003). A brief review of the properties of supercooled pure liquid water and the different liquid water models are discussed in this section. These structures comprise hydrogen-bonded water networks and/or water clusters (“cages”) that are the starting points to hydrate formation.

The anomalies of liquid water become more pronounced when it is supercooled. For example, the volume and entropy fluctuations of liquid water become more pronounced as the temperature decreases. This is in contrast to most other liquids, in which the volume and entropy fluctuations become smaller as the temperature is lowered. Furthermore, the volume and entropy fluctuations in water at less than 4°C are anticorrelated, that is, the increase in volume which occurs when water is cooled results in a decrease in entropy (Debenedetti, 2003).

The anticorrelation between entropy and volume for liquid water has been attributed to the formation of an open hydrogen-bonded network, in which a decrease in orientational entropy is accompanied by a volume increase (Debenedetti, 2003). This network is transient and short-ranged in liquid water (rather than being permanent and long-ranged in ice), and is the microscopic basis for water’s negative thermal expansion. This open hydrogen-bonded network has a profound influence on the thermodynamics of liquid water (Debenedetti, 2003).

In order to understand the behavior of supercooled water it is useful to briefly review the different liquid water models:

1. The “hydrogen-bonded network” picture of Rahman and Stillinger (1973, 1974) is the most favored model. Stillinger (1980) also described water as a “macroscopically connected (three dimensional) random

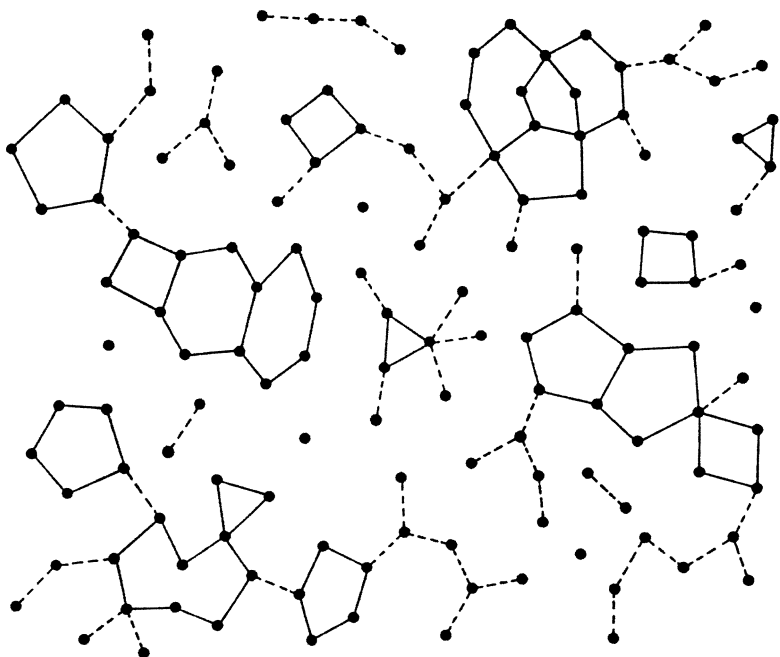


FIGURE 3.2 Networks of water molecules from molecular dynamics. (Reproduced from Rahman, A., Stillinger F.H., *J. Am. Chem. Soc.*, **95**, 7943 (1973). With permission from the American Chemical Society.)

network of hydrogen bonds, with frequent strained and broken bonds, that is continually undergoing topological reformation.” A schematic of such a random network, which includes polygons (most commonly five and six member polygons), is provided in Figure 3.2.

2. The flickering “iceberg” theory of Frank and coworkers (1945, 1957, 1968, 1970) and Nemethy and Scheraga (1962): this model of water comprises an equilibrium mixture of short-lived (10^{-10} s) hydrogen-bonded clusters, together with a nonhydrogen-bonded dense phase (also see Section 2.1.1.4). Consistent with this flickering “iceberg” model is Pauling’s (1959) model of water, consisting of a complex of 5^{12} cavities, in which the guest molecule is water.

The most favored model for supercooled water is based on model (1) for liquid water the “hydrogen-bonded network.” The latter forms the basis of the open hydrogen-bonded network model mentioned previously for supercooled water. Support for this model is based on data and simulations of highly supercooled water (Speedy, 1987; Dore, 1988; Poole et al., 1993; Stanley et al., 1993; Sastry et al., 1996; Angell, 1999; Franzese and Stanley, 2002).

An alternative model of supercooled water comprises clathrate-like entities, which is consistent with model (2) for liquid water. Sorenson (1994) and Walrafen

and coworkers (1995, 1997) suggested support for this model on the basis of Raman spectroscopic measurements on supercooled water (at -33°C) and sII THF hydrate. It should be noted that the water scientific community refer to short-lived liquid cavities (not unit crystals sI, sII, or sH) as clathrate-like structures in water.

Measurements of the properties of highly supercooled water (Speedy, 1987; Speedy et al., 1987; Angell, 1999) indicated that the vital parameter was the concentration and spatial distribution of several unstrained hydrogen-bonded polyhedra (such as the 5^{12} cavity) embedded within the random network of molecules. The hydrogen-bond angles in these polyhedra make it thermodynamically favorable for them to share edges and faces without the introduction of strain. As a result unstrained polyhedra are shown to exhibit an attraction for each other. The sharing of polyhedral faces and edges in supercooled water is suggestive of prenucleation phenomena for hydrates. Further support for the so-called cage effect for supercooled water comes from Mode-Coupling Theory (Chen et al., 1997).

Truskett and Dill (2002) proposed a two-dimensional water-like model to interpret the thermodynamics of supercooled water. This model is consistent with model (1) for liquid water. Cage-like and dense fluid configurations correspond to transient structured and unstructured regions, observed in molecular simulations of water (Errington and Debenedetti, 2001). Truskett and Dill's model provides a microscopic theory for the global phase behavior of water, which predicts the liquid-phase anomalies and expansion upon freezing.

Makogon (1974) was the first to incorporate the above concepts into a hydrate nucleation mechanism, indicating that water molecules cluster with a decrease in temperature.

3.1.1.2 Solubility of natural gases in water

The solubility of nonpolar gases in liquid water is very small, at pressures both above and below the hydrate formation point. Miller and Hildebrand (1968) indicate that the solubility of nonpolar gases in water is at least an order of magnitude lower than the corresponding solubility of nonpolar gases in cyclohexane. Values for solubilities, as well as infinite dilution enthalpies, entropies, and heat capacities of solution at 298 K are given in **Table 3.1**. Examining the solubility and thermodynamics of nonpolar gases in liquid water can provide insight into why certain gases form more stable hydrates than others. These properties may also explain why hydration shells or cage-like clusters can form around the nonpolar molecule.

Since $\Delta G = \Delta H - T\Delta S$, a large negative (unfavorable) entropy of solution overcomes the negative (favorable) enthalpy of solution to yield a small positive value of ΔG of solution. Large negative entropy changes and large positive heat capacity changes are unique to aqueous solutions of nonpolar gases. Himmelblau (1959) noted a dramatic decrease in the entropy of solution for hydrate formers, in contrast to the small nonhydrate formers such as He, H₂, and Ne, is an indication of some special solubility phenomenon associated with size. It is now

TABLE 3.1
Solution Properties of Natural Gas Hydrate Components at 298 K

Component	Solubility ^a $10^5 x_2$	$-\Delta H_{\text{soln}}$ ^b kJ/mol	$-\Delta S_{\text{soln}}$ ^c J/(K mol)	ΔC_p ^d kJ/(K mol)
Methane	2.48	13.26	44.5	55
Ethane	3.10	16.99	57.0	66
Propane	2.73	21.17	71.0	70
Iso-butane ^e	1.69	25.87	86.8	NA
Nitrogen	1.19	10.46	35.1	112
Hydrogen sulfide ^f	177.9	26.35	88.4	36
Carbon dioxide ^g	60.8	19.43	65.2	34

^aSolubility at 101.3 kPa from Miller and Hildebrand (1968) except i-C₄H₁₀, H₂S, and CO₂, as indicated below.

^b $\bar{H}_{\text{L2}}^0 - \bar{H}_G^*$, transfer from gas to infinite dilution liquid, from Franks and Reid (1973).

^c $S_{\text{L2}}^0 - S_G^*$, transfer from gas to liquid, standard state, fugacity = 101.3 kPa.

^dC_p from Alexander et al. (1971) except CH₄, C₂H₆, and H₂S from D'Orazio and Wood (1963).

^ei-C₄H₁₀ properties calculated from Wetlaufer et al. (1964).

^fH₂S properties calculated from Carroll (1990), Selleck et al. (1952), and hypothetical ΔH_{soln} , ΔS_{soln} extrapolated below Q₂ (302 K).

^gCO₂ properties calculated from Alexander et al. (1971).

known that He, H₂, and Ne can form sII hydrate, albeit at very high pressures (Section 2.1.2.2.5).

Entropy is a measure of disorder. The largest negative entropy of solution in Table 3.1 is generally considered as evidence of the creation of structure (increased order) within the body of water. More recently it has been suggested that the creation of a cavity can explain the entropy decrease. Large heat capacity changes also indicate the structuring effect of the solute on the water molecules. The size of the solute molecule has a substantial effect on solubility.

In a review of the thermodynamics of water, Franks and Reid (1973) showed that the optimum molecular size range for maximum solubility was similar to hydrate stability. Franks and Reid noted, "this is not intended to imply that long-lived clathrate structures exist in solution—only that the stabilization of the water structure by the apolar solutes resembles the stabilization of water in a clathrate lattice." Glew (1962) noted that, within experimental error, the heat of solution for ten hydrate formers (including methane, ethane, propane, and hydrogen sulfide) was the same as the heat of hydrate formation from gas and ice, thereby suggesting the coordination of the aqueous solute with surrounding water molecules.

The most popular explanation of such changes in solubility stems from the hypothesis of Frank and Evans (1945), that the presence of the solute molecule causes an increase in the order of bulk water molecules, with the formation of water hydration shells around solute molecules. This is with the caution that such ordering

should not be considered as long-lived or complete in any sense. This hypothesis has been traditionally referred to as the “iceberg” model and has been reexamined and extended numerous times over the past decades (see [Section 2.1.1.4](#) for more details).

The lifetimes of the cage-like water clusters in solution have been also investigated using molecular dynamics (MD) simulations (Guo et al., 2005). Statistical analyses were performed to determine the lifetimes of 5^{12} and $5^{12}6^2$ cage-like clusters, with 200 analyses performed for each cluster. Varying the hydrogen-bond topology of these cage-like clusters was found to have no significant effect on the lifetimes of these clusters that on average ranged from 24.7 to 27.9 picoseconds (ps).

Stillinger (1980) indicated that in the above cage-like clusters around solutes, any nonbonded hydrogens always point outward from the convex structure, thereby encouraging further bonding beyond the cage. This is illustrated in the stereographic pictures in [Figure 3.3](#) of clathrate-like clusters. During the reorientation of water molecules to accommodate the solute molecule, the bonds are calculated to be stronger in the solvation cages compared to pure water, and possess many of the geometrical properties of the 5^{12} cavity (see [Section 2.1.2.1](#)).

The sharing of imperfect cluster faces of the clathrate-like clusters can be viewed as a thermodynamic tendency to minimize the negative entropies of solution. The tendency for face- or edge-sharing of individual solvation clusters, as Stillinger (1980) pointed out, is the same as the tendency for clustering of pure supercooled water.

3.1.1.3 Nucleation theory for ice and hydrates

Hydrate nucleation and growth may have direct analogies in crystallization processes such as the precipitation of salt from solution. Metastability in salt crystallization was hypothesized to occur through supersaturation by Ostwald (1900). (A supersaturated solution is one in which the liquid [solvent] contains more dissolved solute than can be ordinarily accommodated at that temperature; the greater the degree of supersaturation, the greater number of crystal nuclei that will form in solution.) Miers and Isaac (1907) experimentally proved metastability and postulated that for each solute–solvent pair, a concentration–temperature relationship exists that defines the metastable limit, formally called the thermodynamic spinodal.

[Figure 3.4a](#) shows a normal crystallization curve with the spinodal (supersaturation limit) curve (CD) and equilibrium curve (AB). At point P neither nuclei nor crystal growth will occur since the solution is superheated by the amount RP. Once the saturation line (AB) is crossed, either through cooling or increase in concentration, nuclei and crystals may or may not form in the metastable region. Metastable point Q is shown between point R and the crosshatched line CD.

The induction time or lag time is the period between cooling (i.e., supercooling as in 3.1.1.1) to the left of Point R in [Figure 3.4a](#), until the time of solid formation.

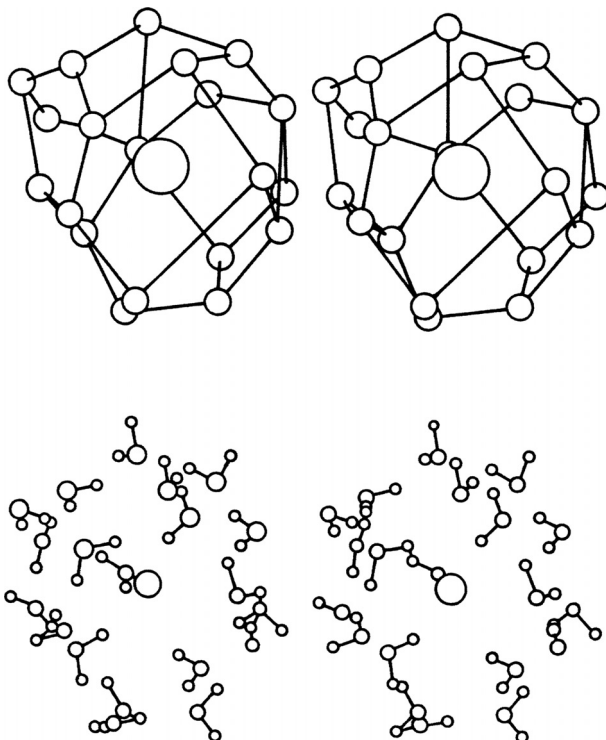


FIGURE 3.3 Stereographic view of water molecules cluster alignment by a dissolved apolar molecule (large circles) from Monte Carlo computer simulation studies. Top figure shown with lines connecting water. (Reproduced from Swaminathan, S., Harrison, S.W., Beveridge, D.L., *J. Am. Chem. Soc.*, **100**, 5705 (1978). With permission from the American Chemical Society.)

Typically, hydrate nucleation and growth will occur within the metastable region before entering the spinodal region. Cooling into the region to the left of line CD (into the spinodal region), nucleation will occur readily (Mullin and Jancic, 1979), due to the high degree of supersaturation, or driving force. Line CD is shown as a broad band, because it has been calculated (e.g., Englezos and Bishnoi, 1988), and only determined experimentally for some systems (e.g., for ice but not for hydrates).

Mullin (1993, p. 117) describes the crystallization regions in Figure 3.4a as the following:

1. The stable zone to the right of equilibrium line AB where crystallization is impossible.
2. The metastable (supersaturated) zone between lines AB and CD where spontaneous crystallization is improbable. However, if a crystal seed were placed in such a metastable solution, growth would occur on the seed.

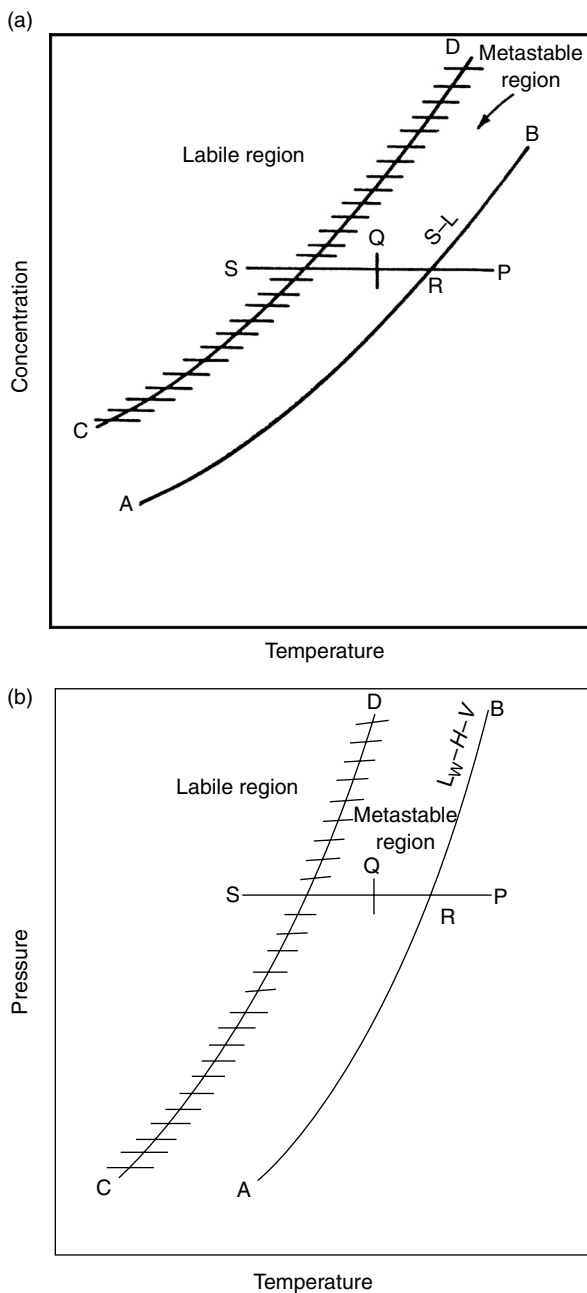


FIGURE 3.4 (a) Crystal and (b) hydrate formation as a function of subcooling relative to the equilibrium line (AB) and the spinodal line (CD; supersaturation limit).

3. The unstable or labile (supersaturated) zone to the left of line CD, where spontaneous crystallization occurs.

A direct analogy is shown in [Figure 3.4b](#) for hydrates if the concentration axis of Figure 3.4a is replaced by a logarithmic pressure axis. The lines CD and AB have effectively the same meaning in Figure 3.4b as in Figure 3.4a. However, it is not known where the spinodal line (CD) occurs for hydrates. To the left of line CD on a $\ln P$ versus T plot, nucleation will readily occur due to the fact that the driving force is very high (see [Section 3.1.3](#)). However, between lines AB and CD there is substantial evidence that the hydrate induction period is not subject to correlation or prediction at the lower driving forces of subcooling or overpressure.

To determine the relationship between hydrate nucleation (requiring three phases) and the more usual type (two-phase nucleation) consider the theory of homogeneous and heterogeneous nucleation in crystallization, as reviewed by Mullin (1993, p. 172) and Kashchiev and Firoozabadi (2002b), from which much of the below discussion has been excerpted.

3.1.1.3.1 Homogeneous nucleation

Homogeneous nucleation (HON) is rarely encountered in the real world. However, despite its shortcomings, the classical nucleation theory (first originating from the work of Volmer and Weber, 1926) still forms the basis of most modern treatments of nucleation. Therefore, only a brief discussion of the fundamental concepts of homogeneous nucleation is included here for completeness.

Homogeneous nucleation is a solidification process occurring in the absence of impurities. It involves many more molecules than could collide simultaneously, so a sequence of bimolecular collisions of an autocatalytic nature is more probable (see [Figure 3.5](#)). That is, there is a sequential formation of clusters (embryos) within the supercooled liquid of increasing cluster size (A_2 = cluster containing two molecules, A_3 = cluster containing three molecules, etc.), until the critical cluster size, A_n is reached. The critical cluster size (also called critical nucleus) is the cluster size that must be reached before nuclei/clusters can grow spontaneously (see [Figure 3.5](#)).

Before achieving the critical size, clusters (or embryos) of molecules form in the bulk metastable liquid, and these clusters may either grow or shrink as a result of density or composition fluctuations. When the cluster attains a critical size, monotonic growth occurs. Such a phenomenon of critical cluster size formation and spontaneous growth may be interpreted by the excess Gibbs free energy (ΔG) between a small solid particle of solute and the solute in solution. ΔG is equal to the sum of the surface excess free energy ΔG_s (for solute molecules becoming part of the surface of the crystal nuclei), and the volume excess free energy ΔG_v (for solute molecules ending up in the bulk/interior of the crystal nuclei).

$$\Delta G = \Delta G_s + G_v = 4\pi r^2 \sigma + \frac{4}{3}\pi r^3 \Delta g_v \quad (3.1)$$

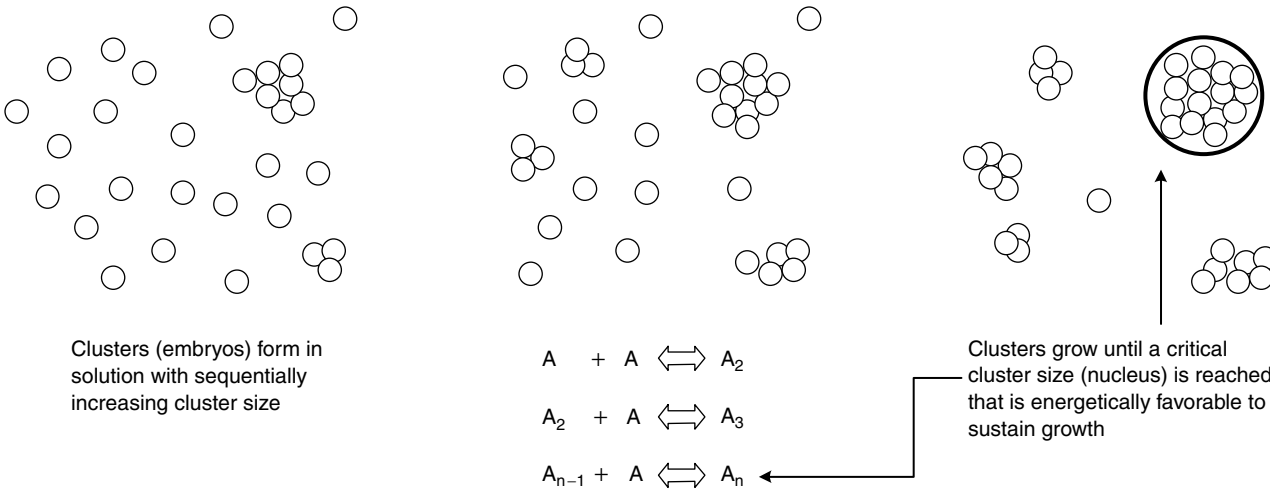


FIGURE 3.5 Schematic of the formation of a critical nucleus according to Classical Nucleation Theory. (T. Strobel, Personal Communication, October 24, 2006.)

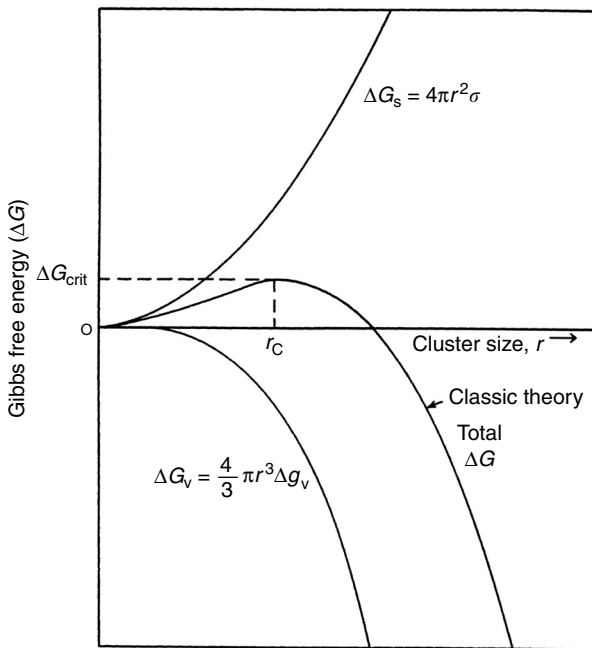


FIGURE 3.6 Comparison of surface excess free energy (ΔG_s) and volume excess free energy (ΔG_v) as functions of cluster size. (Reproduced and modified from Larson, M.A., Garside, J., *Chem. Eng. Sci.*, **41**, 1285 (1986). With permission from Elsevier.)

where Δg_v is the free energy change per unit volume and σ is the surface tension (of the crystal–liquid interface). As shown in Figure 3.6 because Δg_v is negative, ΔG_s and ΔG_v are of opposite sign and are different functions of r , the radius of the solid particle. The addition of the surface and volume effects causes a maximum (ΔG_{crit}) in the value of ΔG at the radius corresponding to the critical nucleus, r_c . That is, the free energy barrier, ΔG_{crit} must be surmounted to form a cluster of a critical size, beyond which the nuclei/clusters grow spontaneously.

The maximum value of ΔG and the critical radius are obtained by differentiating Equation (3.1) and setting the result to zero to obtain:

$$r_c = -2\sigma/\Delta g_v \quad (3.2a)$$

and

$$\Delta G_{\text{crit}} = 4\pi\sigma r_c^2/3 \quad (3.2b)$$

The rate at which critical sized clusters are formed is very sensitive to the height of the free energy barrier (ΔG), or equivalent to the extent of penetration into the metastable region. As the critical cluster size becomes smaller, so does the free energy barrier that must be overcome to form the critical cluster. With increasing

supersaturation, the free energy barrier eventually becomes small enough for nucleation to become spontaneous.

Englezos et al. (1987a) and Englezos and Bishnoi (1988) determined an expression for the radius of the hydrate critical nucleus using the Gibbs free energy per unit volume of hydrate formed (Δg_v) in a modification of Equations 3.2a and b as

$$r_c = \frac{-2\sigma}{\Delta g_v} \quad (3.3a)$$

$$(-\Delta g_v) = \frac{RT}{v_h} \left[\sum_1^2 \theta_j \ln \left(\frac{f_{b,j}}{f_{\infty,j}} \right) + \frac{n_w v_w (P - P_\infty)}{RT} \right] \quad (3.3b)$$

where the surface tension σ is the value of ice in water, v_h and v_w are the molar volumes of hydrate and water, respectively, θ_j is the fractional filling of the hydrate cages on a water free basis, $f_{b,j}$ and $f_{\infty,j}$ are the bulk phase experimental and equilibrium fugacities, respectively, of component j at temperature T , $(P - P_\infty)$ represents the overpressure, and n_w is the number of water molecules per gas molecule. The equation contains the assumption that the hydrate phase is at equilibrium, rather than at operating conditions. In Equation 3.3b the summation term on the right should be divided by the hydration number in order to make it dimensionally consistent.

Using Equations 3.3a and b, Englezos et al. (1987a) calculated the critical radius of methane hydrate to be 30–170 Å. In comparison, critical cluster sizes using classical nucleation theory are estimated at around 32 Å (Larson and Garside, 1986), while computer simulations predict critical sizes to be around 14.5 Å (Baez and Clancy, 1994; Westacott and Rodger, 1998; Radhakrishnan and Trout, 2002).

Chen (1980, p. 7) suggested that the use of bulk phase properties, such as those in Equations 3.1 through 3.3, may be satisfactory only in qualitative analyses. Microscopic critical clusters contain several tens to thousands of molecules, and as such have a spectrum of sizes and properties, which may be difficult to quantify with a single number on a macroscopic scale.

3.1.1.3.2 Heterogeneous nucleation

In practice, homogeneous nucleation is very difficult to achieve, unless very small droplets of ultrapure water are dispersed within an oil emulsion, or very small droplets are formed by expansion through a supersonic (Lavel) nozzle (Wyslouzil et al., 1997).

As also noted by Mullin (1993, pp. 182, 183):

"homogeneous nucleation is not a common event. Aqueous solutions as normally prepared in the laboratory may contain more than 10^6 particles per cm³. It is virtually impossible to achieve a solution completely free of foreign particles, although careful filtration can reduce the contaminants to less than 10^3 per cm³ which may render the solution . . . immune to spontaneously nucleation."

In the more usual case, heterogeneous nucleation (HEN) occurs in the presence of a foreign body (e.g., dust microparticles) or surface (e.g., fluid interface, container, or pipe wall), at smaller supercoolings than that required for homogeneous nucleation. From a free energy standpoint, it is more probable to grow an ice or hydrate nucleus on a two-dimensional surface (container wall or dust) than in the three-dimensional surface-free volume of water. The angle of contact (θ) between the hydrate crystal and a surface is related to ϕ , a fraction that is multiplied by the value of ΔG_{crit} in homogeneous nucleation to obtain a smaller $\Delta G'_{\text{crit}}$ for heterogeneous nucleation:

$$\Delta G'_{\text{crit}} = \phi \Delta G_{\text{crit}} \quad (3.4a)$$

$$\phi = [(2 + \cos \theta)(1 - \cos \theta)^2]/4 \quad (3.4b)$$

When the angle of contact $\theta = 180^\circ$ (complete nonwetting of the substrate) then $\Delta G'_{\text{crit}} = \Delta G_{\text{crit}}$ and when $\theta = 0^\circ$ (complete wetting of the substrate) then $\Delta G_{\text{crit}} = 0$. The foreign surface effectively lowers the $\Delta G'_{\text{crit}}$ and critical radius (r_c) required for catastrophic growth, as shown in Equations 3.4a and b. Homogeneous nucleation of hydrates is an anomaly. Hence, heterogeneous nucleation occurs much more frequently.

The kinetics of nucleation of one-component gas hydrates in aqueous solution have been analyzed by Kashchiev and Firoozabadi (2002b). Expressions were derived for the stationary rate of hydrate nucleation, J , for heterogeneous nucleation at the solution–gas interface or on solid substrates, and also for the special case of homogeneous nucleation. Kashchiev and Firoozabadi's work on the kinetics of hydrate nucleation provides a detailed examination of the mechanisms and kinetic expressions for hydrate nucleation, which are based on classical nucleation theory. Kashchiev and Firoozabadi's (2002b) work is only briefly summarized here, and for more details the reader is referred to the original references.

Thus, the work, $W(J)$, to form a hydrate cluster of n building units can be determined using the classical theory of nucleation.

$$W(n) = -n \Delta \mu + C v_h^{2/3} \sigma_{\text{ef}} n^{2/3} \quad (3.5)$$

where $\Delta \mu$ is the supersaturation. Physically, this term represents the work gained on assembling n hydrate building units into an n -sized hydrate cluster (nucleation can only occur when $\Delta \mu > 0$). C is the shape factor. A spherical cluster is formed in homogeneous nucleation ($C = (36\pi)^{1/3}$; Figure 3.7a). In heterogeneous nucleation, a cap-shaped cluster is formed on a solid substrate, while a lens-shaped cluster is formed at the interface between the solution and gas phase (Figures 3.7b,c, respectively). The volume of the hydrate building unit, v_h (m^3), is composed of one gas molecule and n_w (hydration number) water molecules. The effective specific surface energy, σ_{ef} (J/m^2), is the work done to create the interface between the cluster and the solution (in HON), or the solution and substrate (HEN), or solution and gas (HEN).

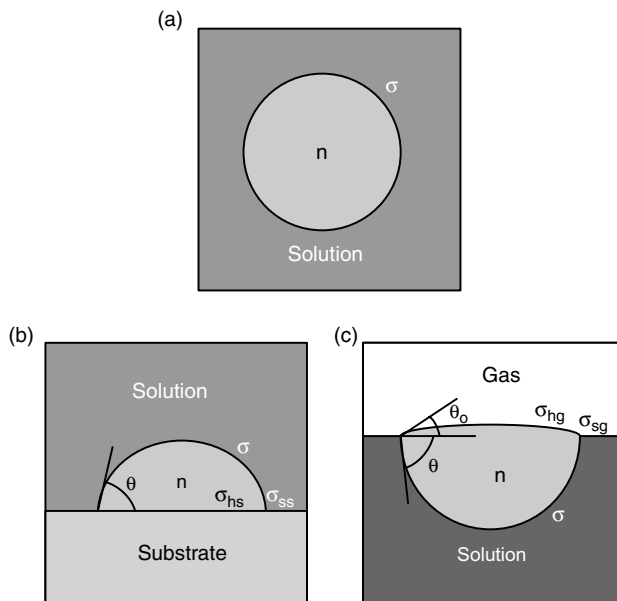


FIGURE 3.7 Schematic of (a) spherical cluster of n building units in HON; (b) cap-shaped cluster of n building units in 3D HEN on a substrate; (c) lens-shaped cluster of n building units in 3D HEN at the solution–gas interface. σ_{ss} , σ_{hs} , σ_{sg} , σ_{hg} are specific energies of the solution–substrate, hydrate–substrate, solution–gas and hydrate–gas interfaces. (Reproduced from Kashchiev, D., Firoozabadi, A., *J. Cryst. Growth*, **243**, 476 (2002b). With permission from Elsevier.)

In Figure 3.7, the wetting angle is given by θ . The nonwetting case ($\theta = 180^\circ$) is given by HON, which is the energetically limiting case of HEN. Kashchiev and Firoozabadi note that the HEN cap-shaped hydrate cluster on the hydrate-wetted solid surface in solution is thermodynamically favored over HON. The better the substrate/hydrate wetting (i.e., the smaller the wetting angle θ), the greater the probability of HEN.

The authors further note that although visual observations have shown that hydrate crystallizes at the solution–gas interface, this may also be because of nucleation and subsequent growth within a thin solution layer adjacent to the solution–gas interface. For kinetic reasons, the supersaturation in the thin solution layer can be locally high, and therefore hydrate nucleation and subsequent growth in this layer would in fact be more probable than in the bulk of the solution.

3.1.1.4 Site of hydrate nucleation

Long and Sloan (1996) performed a series of measurements to investigate the site of nucleation for natural gas and carbon dioxide hydrate initiation in a sapphire tube.

A hydrate nucleating agent (precipitated amorphous silica) and a quiescent surface inhibitor (sodium dodecyl sulfate) were used in an attempt to initiate hydrates in the bulk phase. While the induction time (for detectable hydrate formation) was not predictable, in every case hydrate was initiated at a surface—usually at the vapor–water interface, but infrequently along the sides of the sapphire tube in the gas phase, and at the metal end-plate below the liquid phase.

A number of other researchers have also confirmed that nucleation and subsequent growth typically occurs at the water–hydrocarbon interface: for methane hydrate (Huo et al., 2001; Østergaard et al., 2001; Taylor, 2006) and carbon dioxide hydrate (Kimuro et al., 1993; Fujioka et al., 1994; Hirai et al., 1995; Mori, 1998).

Molecular dynamics (MD) simulation studies also indicate that the initial formation of methane hydrate occurs preferentially near the water–methane interface where there is a significant concentration gradient (Moon et al., 2003).

Hydrate formation usually occurs at the vapor–liquid interface (or within a thin film located at the vapor–liquid interface; Kashchiev and Firoozabadi, 2002b), not only because the interface lowers the Gibbs free energy of nucleation, but also because the interface is the location of the required very high concentrations of host and guest molecules. The hydrate guest composition may be as high as 0.15 mole fraction, with the remainder being water. Yet the water mole fraction in the hydrocarbon phase is typically less than 0.05, while the mole fraction of hydrocarbon in the aqueous phase is never greater than 0.001.

With such low concentrations of components available to form critical nuclei, hydrate formation seems unlikely in the bulk phases. However, at an interface where higher concentrations exist through adsorption (particularly at the vapor–liquid interface where both phases appear in abundance) cluster growth to a supercritical size is a more likely event. High mixing rates may cause interfacial gas + liquid + crystal structures to be dispersed within the liquid, giving the appearance of bulk nucleation from a surface effect.

3.1.2 Conceptual Picture of Hydrate Nucleation at the Molecular Level

Since hydrate initiation usually occurs at the vapor–liquid interface, molecular models of hydrate nucleation have focused on that surface. The earliest conceptual picture for hydrate nucleation is the labile cluster mechanism. A labile cluster is an unstable entity that readily undergoes change. The labile clusters are composed of a guest molecule surrounded by 20 and 24 (cf. 5^{12} , $5^{12}6^2$ cages of sI) or 20 and 28 (cf. 5^{12} , $5^{12}6^4$ cages of sII) water molecules in the first solvation shell. This model considers nucleation to occur by the agglomeration of labile clusters either on the liquid or the vapor side of the interface (Figure 3.9). A modification of the labile cluster model is based on adsorption and clustering on the vapor side of the interface (Figure 3.11). An alternative more recent mechanism is the local structuring hypothesis that focuses on the development of guest molecules being arranged (ordered) in configurations similar to that in the hydrate and a

hydrogen-bonded water network ([Figures 3.12](#) and [3.13](#)). These three postulated mechanisms will be discussed in Sections 3.1.2.1 through 3.1.2.3.

It is plausible that hydrate nucleation proceeds via some combination of these mechanisms. The hydrate nucleation and growth processes may be analogous to the corresponding processes occurring during ice formation. This analogy may be suggested from the recent MD simulation of ice nucleation and growth resulting in water freezing (Matsumoto et al., 2002). These simulations were run for an extremely long time compared to typical simulations, capturing timescales of up to 500 ns (nanoseconds). Ice nucleation occurs when a sufficient number of relatively long-lived hydrogen bonds develop at the same location to form a compact initial nucleus. The initial nucleus, on reaching a critical size, expands rapidly resulting in the entire system freezing ([Figure 3.8](#)).

3.1.2.1 Labile cluster nucleation hypothesis

Using the fact that water clusters around dissolved gas molecules (Section 3.1.1.2), it was proposed that clusters may grow to achieve a critical radius, as shown schematically in [Figure 3.9](#) (Sloan, 1990; Sloan and Fleyfel, 1991; Muller-Bongartz et al., 1992). Christiansen and Sloan (1994) extended the model, with the following key elements:

1. Pure water exists without guests, but with many transient, labile ring structures of pentamers and hexamers.
2. Water molecules form labile clusters around dissolved guest molecules. The cluster size depends on the dissolved guest size range. The number of water molecules in each cluster shell (i.e., coordination number of water molecules surrounding a guest molecule) for natural gas components are: methane (20), ethane (24), propane (28), iso-butane (28), nitrogen (20), hydrogen sulfide (20), and carbon dioxide (24).
3. Clusters of dissolved species combine to form unit cells. To form sI coordination numbers of 20 and 24 are required for 5^{12} and $5^{12}6^2$ cavities, while sII requires coordination numbers of 20 and 28 for the 5^{12} and $5^{12}6^4$ cavities. Nucleation is facilitated if labile clusters are available with both types of coordination numbers for either sI (e.g., $\text{CH}_4 + \text{CO}_2$ mixtures) or sII (e.g., $\text{CH}_4 + \text{C}_3\text{H}_8$ or most unprocessed natural gases). If the liquid phase has clusters of only one coordination number, nucleation is inhibited until the clusters can transform to the other size, by making and breaking hydrogen bonds.
4. An activation barrier is associated with the cluster transformation. If the dissolved gas is methane, the barrier for transforming the cluster coordination number from 20 (for the 5^{12}) to 24 (for the $5^{12}6^2$) is high, both because the guest cannot lend much stability to the larger cavity (see [Section 2.1.3.2](#)) and because the $5^{12}6^2$ cavities outnumber the 5^{12} in sI by a factor of 3. Transformation of methane–water clusters from

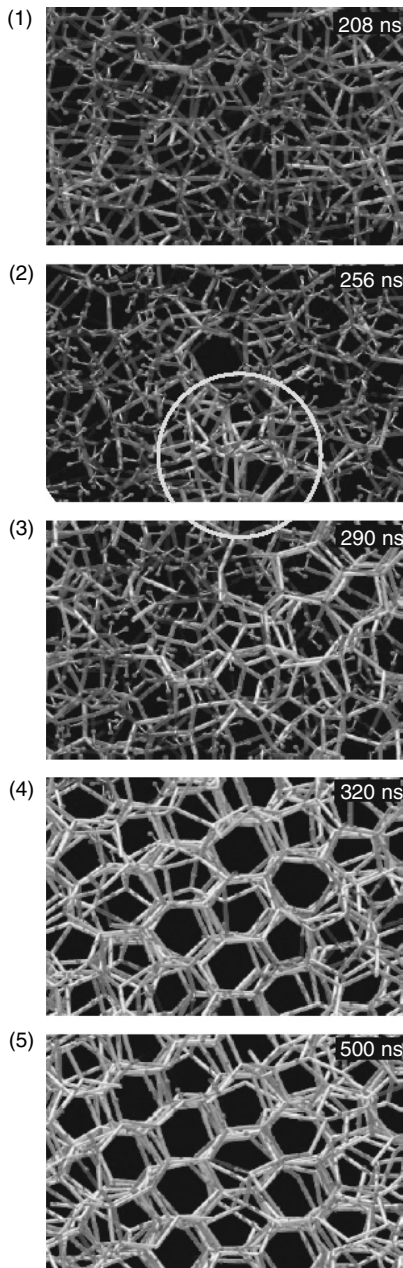


FIGURE 3.8 MD simulation of ice nucleation and growth showing the hydrogen-bond network structure of water at a given time. At time $t = 208$ ns (1), $t = 256$ ns (2), $t = 290$ ns (3), $t = 320$ ns (4), $t = 500$ ns (5). Lines indicate hydrogen bonds between water molecules. Bright white lines indicate long-lasting H-bonds (lifetimes >2 ns). An initial nucleus is formed in the circled region (in 2). (Reproduced from Matsumoto, M., Saito, S., Ohmine, I., *Nature*, **416**, 409 (2002). ©With permission.)

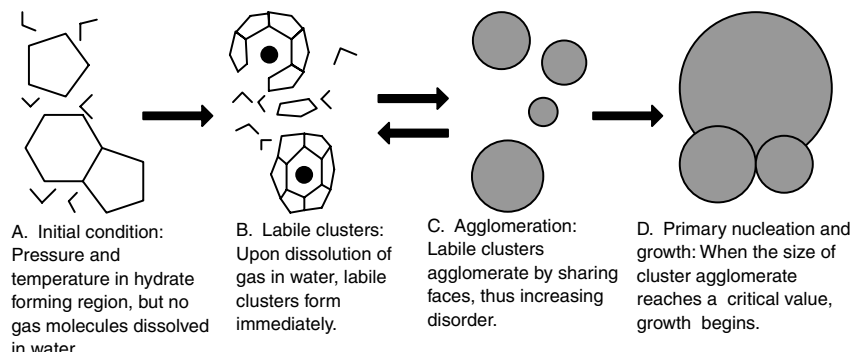


FIGURE 3.9 Schematic model of labile cluster growth. (Reproduced from Christiansen, R.L., Sloan, E.D., in *Proc. First International Conference on Natural Gas Hydrates* (1994) New York Academy of Sciences. With permission.)

20 to 28 has an even higher energy barrier, because methane is not large enough to stabilize the $5^{12}6^4$ cavity (unless at very high pressure).

5. If the dissolved gas is ethane with a water coordination number of 24, the transformation of empty cavities (with a coordination number of 20) is likely to be rapid, due to the high ratio (3:1) of $5^{12}6^2$ to 5^{12} cavities in sI. If the dissolved gas is propane with a coordination number of 28, transformation to sII is likely to be slow because $5^{12}6^4$ cavities are outnumbered by 5^{12} cavities by a factor of two.
6. Figure 3.10 shows the cluster mechanism imposed on the pressure–temperature trace presented in Figure 3.1b. At Point A after pressurization of the system, guest molecules are dissolved in water and short-lived cages have been formed. The linking of clusters to each other occurs after cooling from Point A until a critical radius cluster is formed at Point B, where catastrophic nucleation and growth occurs. On heating the system from Point C, the reaction is driven to dissociate the hydrate (to the right in Figure 3.10).
7. At temperatures higher than Point D (and at $T < 28^\circ\text{C}$) in Figure 3.10, clusters continue to persist, so that the solid phase is not totally disrupted upon the transition to a liquid and vapor. Only after a matter of some hours or days will the clusters be dispersed to a more normal water distribution.
8. Alternative structures arise that provide parallel formation pathways and consequently slow nucleation kinetics.

In the hypothesis, Points 5 and 8 above (alternative structures) have come under criticism, first by Skovborg et al. (1992) and then by Natarajan et al. (1994). However, Skovborg noted that alternating structures may account for some of his nucleation data. A further criticism of the labile cluster hypothesis is that the energy barrier for agglomeration of clusters is far larger than cluster disintegration (Radhakrishnan and Trout, 2002).

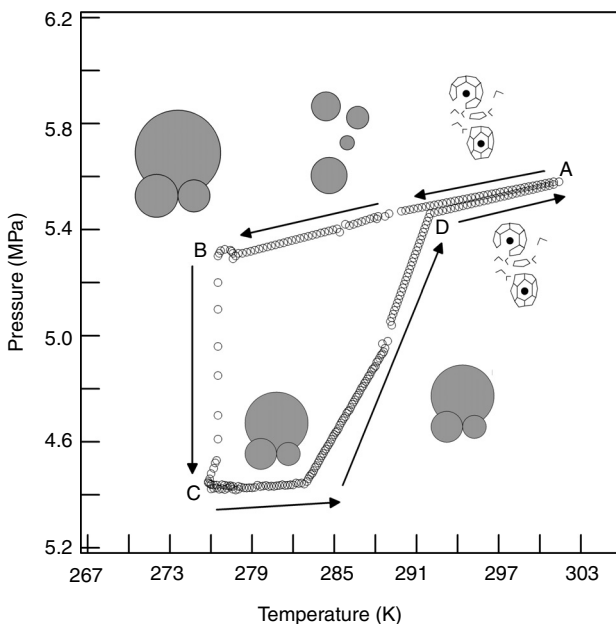


FIGURE 3.10 Hydrate labile cluster growth mechanism imposed on a pressure-temperature trace. (Reproduced from Christiansen, R.L., Sloan, E.D., in *Proc. First International Conference on Natural Gas Hydrates* (1994) New York Academy of Sciences. With permission.)

3.1.2.2 Nucleation at the interface hypothesis

Long (1994) and Kvamme (1996), suggested that nucleation arises on the vapor side of the interface. A conceptual picture is shown in Figure 3.11, with the following components for heterogeneous nucleation on the vapor side of the interface:

1. Gas molecules are transported to the interface. Long (1994) notes that the gas impingement rate is 10^{22} molecules/(cm²s) at the normal temperatures and pressures of hydrate formation. Kvamme (1996) indicates this step is transport of molecules through a stagnant boundary.
2. Gas adsorbs on the aqueous surface. While both Long and Kvamme list adsorption as a separate step before either surface diffusion or clustering of the water, adsorption may occur in a partially completed cavity.
3. The gas migrates to a suitable location for adsorption through surface diffusion. At this location the water molecules form first partial, and then complete cages around the adsorbed species.
4. Labile clusters join and grow on the vapor side of the surface until a critical size is achieved. This can occur either by the addition of water and gas molecules to existing cavities, via the joining of cavities along the interface (as indicated in the cluster aggregation mechanism) or both.

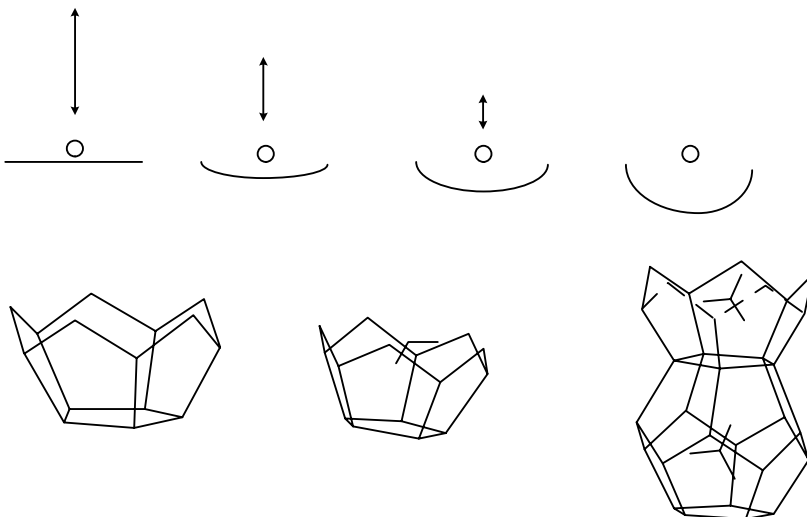


FIGURE 3.11 Adsorption of gas molecules onto labile hydrate cavities at gas–water interface. (From Long, J., *Gas Hydrate Formation Mechanism and Its Kinetic Inhibition*, Ph.D. Thesis, Colorado School of Mines, Golden, CO, 1994. With permission.)

As noted in Section 2.1.2.1, the outside of hydrate cavities are never smooth, but have hydrogen atoms pointing outward that serve as positive attractions for other molecules and cavities, just as the cavity oxygen atoms with no outwardly pointing hydrogen atoms serve as negative charges for further attachments.

The interfacial cluster hypothesis should not be viewed as an orderly progression from small water clusters to large hydrate masses. In contrast, one might envision every combination of hydrogen bonds possible, with some clusters growing, but other clusters shrinking. A better conception is a very large number of clusters at every instant—not just one or a few clusters progressing in time.

3.1.2.3 Local structuring nucleation hypothesis

Molecular simulation methods have been applied to investigate the nucleation mechanism of gas hydrates in the bulk water phase (Baez and Clancy, 1994), and more recently at the water-hydrocarbon interface (Radhakrishnan and Trout, 2002; Moon et al., 2003). The recent simulations performed at the water-hydrocarbon interface provide support for a local structuring nucleation hypothesis, rather than the previously described labile cluster model.

Radhakrishnan and Trout (2002) performed Landau free energy calculations to investigate the (homogeneous) nucleation mechanism of carbon dioxide hydrate at the liquid water-liquid carbon dioxide interface. These free energy calculations showed that it was thermodynamically more favorable for labile clusters to disintegrate than to agglomerate. The authors therefore suggested that it is highly

unlikely that carbon dioxide hydrate nucleation occurs via the labile cluster mechanism. Instead, they proposed the local structuring hypothesis, in which:

1. Thermal fluctuations cause a group of guest (CO_2) molecules to be arranged in a configuration similar to that in the clathrate hydrate phase. The structure of water molecules around locally ordered guest molecules is perturbed compared to that in the bulk. The thermodynamic perturbation of the liquid phase is due to the finite temperature of the system. This process is stochastic.
2. The number of guest molecules in a locally ordered arrangement exceeds that in the critical nucleus. Guest–guest and host–host cluster order parameters take on values that are very close to the clathrate hydrate phase, which results in formation of a critical nucleus.

Moon et al. (2003) also proposed a local order (or structure) model similar to that of Radhakrishnan and Trout (2002), on the basis of MD simulations of methane hydrate nucleation at a methane–water interface over a timescale of around 7 ns. Within this timescale, there is steady growth of water clusters of critical sizes comparable to previous reports (see [Section 3.1.1.3](#)). However, full crystallization cannot be seen on this timescale. Simulated radial distribution functions of the methane–methane distances as a function of time are shown in Figure 3.12. Initially, a strong peak at around 4 Å is present due to the methane–methane close contacts within water. As time progresses, this peak at 4 Å disappears and a strongly symmetric peak at 6.5 Å appears, which corresponds to the nearest inter-methane distance in methane hydrate, consistent with two methane molecules separated by a planar water ring. A third peak at 10.5 Å is shown to also grow throughout the simulation. The radial distribution functions up to 7 Å are qualitatively consistent with corresponding functions determined

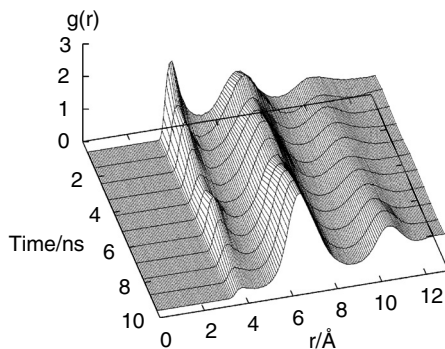


FIGURE 3.12 Methane–methane radial distribution functions calculated from successive 0.9 ns portions of the simulation, indicating ordering of the methane molecules during hydrate nucleation. (Reproduced from Moon, C., Taylor, P.C., Rodger, P.M., *J. Am. Chem. Soc.*, **125**, 4706 (2003). With permission from the American Chemical Society.)

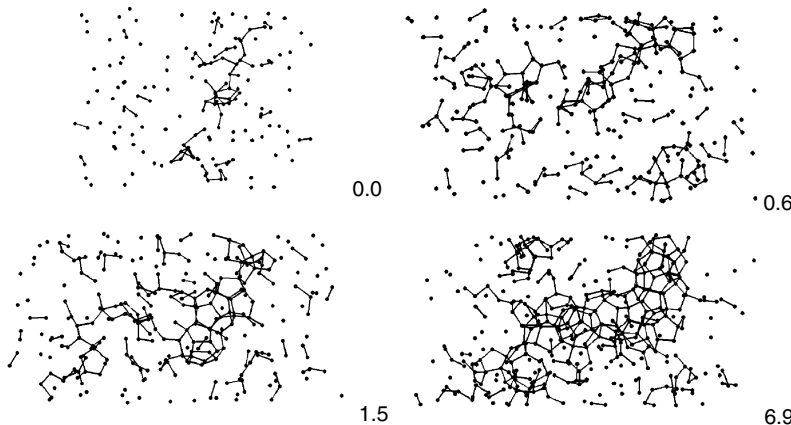


FIGURE 3.13 Snapshots of clathrate clusters at given times (ns). Only hydrate-like waters are shown; lines indicate the hydrogen-bond network. (Reproduced from Moon, C., Taylor, P.C., Rodger, P.M., *J. Am. Chem. Soc.*, **125**, 4706 (2003). With permission from the American Chemical Society.)

from neutron diffraction (Koh et al., 2000). Increasing structural order is also shown in the simulated water radial distribution functions.

Figure 3.13 shows snapshots of the hydrate nucleation simulations by Moon et al. (2003). Initially, there is no evidence of clustering, after 0.6 ns there is aggregation to form a two-dimensional sheet-like structure. The first complete clathrate cage (5^{12}) is formed after 0.8 ns, with numerous incomplete cages evident even earlier. After 7 ns a structured chain of clathrate cages (6 complete 5^{12} cages and another 20 incomplete/fluxional cages) is seen that spans the width of the simulation box; that is, unlike the case of the labile cluster hypothesis, which involves a buildup of individually solvated methane molecules, the simulation results showed a more concerted rearrangement of water over longer ranges than an individual solvation cage. The larger clusters formed contain long-range ordering of the guests, which therefore supports the local ordering hypothesis.

A further interesting feature of this simulation study is the identification of face-sharing doublets of 5^{12} cages at around 6 ns, which remain stable for the remainder of the simulation (Figure 3.14). Conversely, there was no evidence of water bridged 5^{12} cages. The 5^{12} cages pack by sharing faces in sII hydrate, while in sI hydrate 5^{12} cages are bridged by additional water molecules. This is consistent with experimental diffraction studies, which suggest that for the sI hydrate former, CO₂, a metastable sII hydrate phase can be formed prior to the formation of the more stable sI hydrate (Staykova and Kuhs, 2003).

Despite the formation of clathrate-like clusters and complete 5^{12} cages during these simulations, the increased ordering observed from the radial distribution functions and local phase assignments resulted in the authors concluding that their simulation results are consistent with a local order model of nucleation, and therefore do not support the labile cluster model.

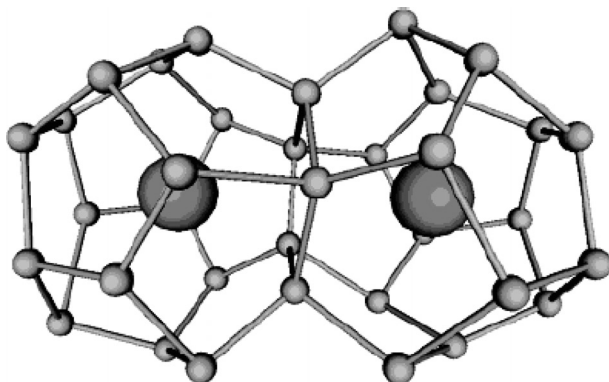


FIGURE 3.14 A stable face-sharing dimer of 5^{12} cages, formed by 6 ns. (Reproduced from Moon, C., Taylor, P.C., Rodger, P.M., *J. Am. Chem. Soc.*, **125**, 4706 (2003). With permission from the American Chemical Society.)

A number of studies have indicated that a labile cage-like (5^{12}) cluster of 20 water molecules around a hydrate guest former may not form preferentially at the initial stages of nucleation. MD simulations of xenon hydrate formation from a xenon–ice system showed that there is no preferential formation of cavities with 20 water molecules, which would be similar to the small hydrate cage. Rather, the statistical mean cage size distribution was found to be between 24 and 27 water molecules. Tse et al. (2002) suggest that this supports the experimental observation that sII SF_6 hydrate formation does not require occupation of small cages.

In order to verify which of the above nucleation mechanisms accurately represents hydrate nucleation, it is clear that experimental validation is required. This can then lead to such qualitative models being quantified. However, to date, there is very limited experimental verification of the above hypotheses (labile cluster or local structuring model, or some combination of both models), due to both their stochastic and microscopic nature, and the timescale resolution of most experimental techniques. Without experimental validation, these hypotheses should be considered as only conceptual aids. While the resolution of a nucleation theory is uncertain, the next step of hydrate growth has proved more tenable for experimental evidence, as discussed in Section 3.2.

3.1.3 Stochastic Nature of Heterogeneous Nucleation

As an example of the difference between stochastic and deterministic properties consider Figure 3.15. A deterministic property is illustrated by any common thermodynamic property, such as temperature, as illustrated by the vertical line in Figure 3.15. For a specific equilibrium state, the probability of observing a specific temperature is 1, that is, a certainty that is called deterministic.

However, for some properties, the probability of observation is distributed over a range of values, so that observation of a certain value (at the peak of the

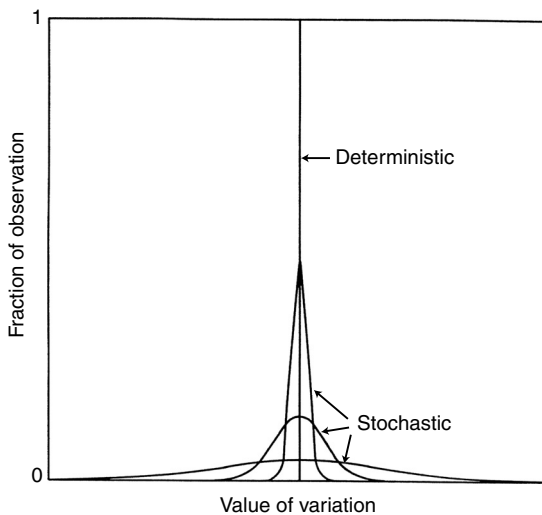


FIGURE 3.15 Comparison of stochastic and deterministic properties. (Reproduced from Rowley, J.L., *Statistical Mechanics for Thermophysical Property Calculations* (1994). With permission from Prentice Hall Inc.)

curve) is most likely but not certain. In such cases, normal distributions are shown in the lower three curves in Figure 3.15, for which the integral of each is unity. Ideally we hope to observe the mean value (the maximum in each curve), but there is a significant chance that other values (distributed about the mean) will be also observed. Distributions with uncertainty in the observed value, such as shown in the lower curves of Figure 3.15, are called stochastic.

Therefore, the key question arises: is hydrate nucleation stochastic or deterministic? The measurements performed to date (summarized in this section) indicate that the induction period (including hydrate nucleation and growth onset until hydrate formation is detected) is stochastic, particularly at low driving forces in the region such as shown between lines AB and CD in Figure 3.4b. However, with a higher driving force, the system becomes less stochastic, with a narrower distribution range.

Haymet and coworkers used an automated lag-time apparatus (ALTA) to obtain statistical data on the supercooling point (SCP, also known as freezing temperature) of water freezing to ice (Wilson et al., 2003) and water/tetrahydrofuran (THF) freezing to hydrate/ice (Wilson et al., 2005). The SCP is the temperature of spontaneous freezing of a solution (Zachariassen, 1982). A small sample (300 μL) was cooled linearly (at 4.5 K/min) until the sample froze. The frozen sample was melted, and then refrozen. This freezing–melting cycle was repeated over 300 times on the same sample.

Wilson et al. (2003, 2005) demonstrate the stochastic nature of the SCP, and that many measurements should be performed on a single sample in order to obtain statistically valid measurements of the SCP. However, a particularly

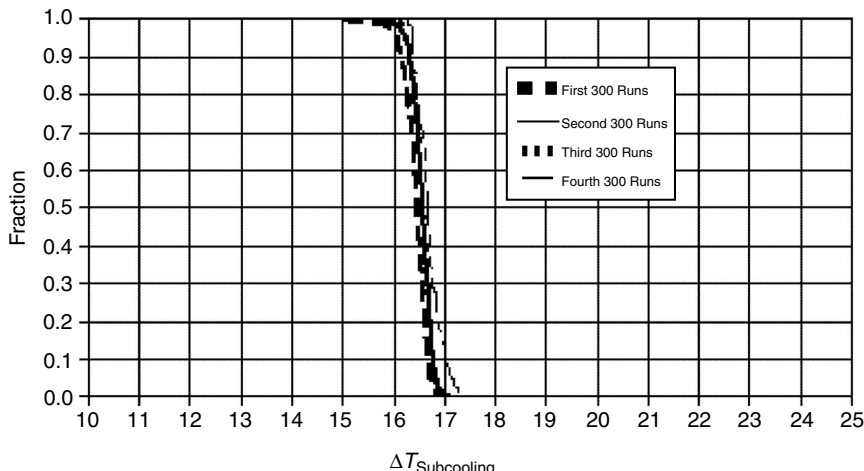


FIGURE 3.16 Survival curves for four back-to-back series of 300 runs each on the same THF/water (10 wt% THF) sample in the same tube. The nucleation temperature is not changed significantly between each data series. (Reproduced from Wilson, P.W., Lester, D., Haymet, A.D.J., *Chem. Eng. Sci.*, **60**, 2937 (2005). With permission from Elsevier.)

startling feature of the results is the narrow range of SCP values obtained from these measurements (i.e., within ± 2.5 K).

In order to determine the SCP (or freezing temperature), a survival curve was constructed by plotting the fraction of unfrozen samples at a given temperature (or time) versus the degree of supercooling (Figure 3.16). That is, the same sample did not always freeze at the same temperature on each run, instead there was a distribution of freezing temperatures. To provide accurate statistics for the system, 300 runs were found to be sufficient, that is, the survival curve did not change magnitude or shape with further repeat measurements. The results of four back-to-back series of 300 runs on the same sample are shown in Figure 3.16 and show that the SCP temperature is not changed significantly when comparing these series of data.

Each survival curve clearly shows that at smaller supercooling temperatures (i.e., higher experimental temperatures) all runs remained unfrozen, while at larger supercooling temperatures (i.e., lower experimental temperatures) all runs were frozen. From these survival curves, Wilson et al. (2003, 2005) defined the nucleation temperature for a given sample, also called the SCP, or kinetic freezing point, as the temperature at which half the runs of the same sample have frozen (T_{50}). The inherent width of each survival curve was considered as an indication of the stochastic nature of nucleation, with the “10–90” width (i.e., the range of temperature from 10% samples unfrozen to 90% samples frozen) to be an indicator of the error bars for the SCP.

One key question arises from the above results. That is, considering the measurement temperatures were well below the ice melting point, was ice formed

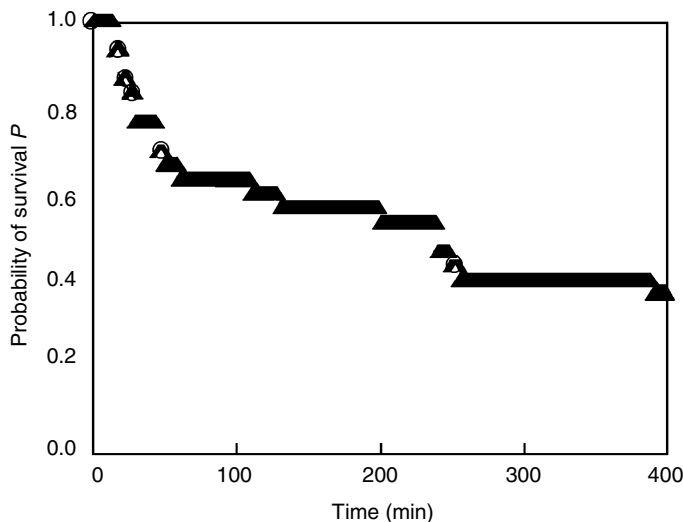


FIGURE 3.17 Probability of survival of $\text{CH}_3\text{CCl}_2\text{F}$ hydrate free samples plotted vs. the induction time. The triple liquid–water/hydrate/liquid– $\text{CH}_3\text{CCl}_2\text{F}$ equilibrium temperature is 281.6 K. The sample is cooled to 277.2 K (within 90 s), and held at this temperature until nucleation occurs and hydrate growth is detected. (Reproduced and modified from Ohmura, R., Ogawa, M., Yasuka, K., Mori, Y.J., *J. Phys. Chem. B*, **107**, 5289 (2003). With permission from the American Chemical Society.)

instead of, or in addition to hydrate? Also, would these results for a simple system of a miscible solution of tetrahydrofuran–water be transferable to the more complex system of a gas–water mixture? To address these questions, the freezing temperature (SCP) of xenon hydrate formed from a xenon gas–water mixture was measured repeatedly using differential scanning calorimetry (Hester, K.C., unpublished data). Twelve repeat samples were measured, with the preliminary results indicating that the scatter of the data was only within a 2°C range, which is a similar scatter range to that reported by Wilson et al. (2005). Therefore, repeated induction time–temperature measurements (at high driving force with a constant cooling rate) may vary only within a narrow range of values. This suggests that the induction time–SCP measured using a constant cooling rate may be a more probabilistic parameter.

In contrast, induction time measurements of $\text{CH}_3\text{CCl}_2\text{F}$ hydrate performed at constant temperature (measuring hold times), demonstrated a much higher degree of stochastic or random behavior (Ohmura et al., 2003). In these experiments the induction time was detected, using video imaging, as the first change in morphology of the $\text{CH}_3\text{CCl}_2\text{F}$ droplet that was immersed in water. The probability of survival curves tend to vary over a far wider distribution of nucleation times (Figure 3.17). These results show that the induction time in these cases (where the sample is held at constant temperature) can be more stochastic than those obtained during cooling.

Several other studies have been performed to measure hydrate induction times where the sample was held at constant temperature (e.g., Muller-Bongartz et al., 1992; Parent, 1993; Bansal, 1994; Nerheim et al., 1994; Cingotti et al., 1999; Kelland et al., 2000). In all these studies significant scatter in the induction time data were reported.

The above studies support the notion that nucleation is a very stochastic phenomenon when the sample is held at constant temperature, compared to when the sample was cooled at a constant cooling rate. As suggested previously, the magnitude of the driving force can affect the degree of stochastic or random behavior of nucleation. For example, on the basis of extensive induction time measurements of gas hydrates, Natarajan (1993) reported that hydrate induction times are far more reproducible at high pressures (>3.5 MPa) than at lower pressures. Natarajan formulated empirical expressions showing that the induction time was a function of the supersaturation ratio.

3.1.4 Correlations of the Nucleation Process

Data and correlations for the nucleation process should be used with extreme caution. One major conclusion of this section is that induction time correlations may be applied (if at all) under very restricted conditions for the following three reasons:

1. Induction times are very scattered and, particularly at low driving forces (under isothermal conditions), nucleation is stochastic and therefore unpredictable.
2. Induction times appear to be apparatus-dependent, for example, the times depend on the degree of agitation (cavitation or turbulency), surface area of the system, and the rate of heat or mass transfer.
3. Induction times appear to be also a function of time-dependent variables such as the history of the water, the gas composition, and the presence of foreign particles.

Despite 1–3 above, recent statistical measurements performed by Wilson et al. (2003, 2005) suggest that the freezing temperature for hydrate/ice nucleation varies only within around 2°C at high driving forces under continuous cooling. In essence, there is only a limited number of statistical data sets available in the literature, with varying reports of the extent of reproducibility of induction times from different groups. Statistical analyses are required in order for reliable induction times to be obtained for gas hydrate systems. To date, statistical analyses of hydrate induction times have not been performed for gas hydrate systems. Furthermore, there is a need for induction time measurements to be performed and correlated between different apparatus setups. In order to be able to assess whether the induction time–freezing temperature of gas hydrates can be predicted to an acceptable level of accuracy, much work still remains to be performed. It may be however, that such a task is intractable.

TABLE 3.2
Different Driving Forces Used for Nucleation

Investigators	Year	Driving force
Vysniauskas and Bishnoi	1983b	$T^{\text{eq}} - T^{\text{exp}}$
Skovborg and Rasmussen	1992	$\mu_{\text{WH}}^{\text{exp}} - \mu_{\text{WL}}^{\text{exp}}$
Natarajan et al.	1994	$f_i^{\text{exp}}/f_i^{\text{eq}} - 1$
Christiansen and Sloan	1995	Δg^{exp}
Kashchiev and Firoozabadi	2002	$\Delta\mu$, supersaturation
Anklam and Firoozabadi	2004	Δg
Arjmandi et al.	2005b	$T^{\text{eq}} - T^{\text{exp}}$

3.1.4.1 Driving force of nucleation

A number of driving forces for the nucleation process are used in the hydrate literature, as listed in Table 3.2. Apart from a few works (Sloan et al., 1998; Kashchiev and Firoozabadi, 2002a; Arjmandi et al., 2005a), limited justifications have been provided for these driving forces, based upon equilibrium or nonequilibrium thermodynamics. The purpose of this subsection is to provide a brief justification for a general nucleation driving force, and to show other driving forces to be special cases of the more general case. The driving force is the key component of a hydrate nucleation correlation. In essence, the general case driving force is shown below to incorporate all the driving forces proposed (Table 3.2), though the term $\ln(f_i^{\text{eq}}/f_i^{\text{exp}})$ dominates (f_i^{eq} and f_i^{exp} are the fugacity of component i at the equilibrium and experimental pressure, respectively, that is, indicating overpressure). The subcooling driving force is shown to be the isobaric equivalent of the isothermal general case driving force.

Christiansen and Sloan (1995) presented the total molar change in Gibbs free energy of hydrate formation, Δg^{exp} as the driving force. The driving force derived by Christiansen and Sloan has been shown to be the general case for all driving forces for nucleation presented by previous researchers. Under constraints of constant temperature and pressure, processes move toward the minimum value of Gibbs free energy. Figure 3.18 illustrates an isothermal route for calculating such a state variable by devising a convenient calculable path between the two end points—the products (superscript “pr”) and reactants (rx) at the operating temperature and pressure. In this system, only the gas and water converted to hydrate are considered as reactants while hydrate represents the product.

$$\Delta g^{\text{exp}} = \Delta g^{\text{rx}} - \Delta g^{\text{pr}} \quad (3.6a)$$

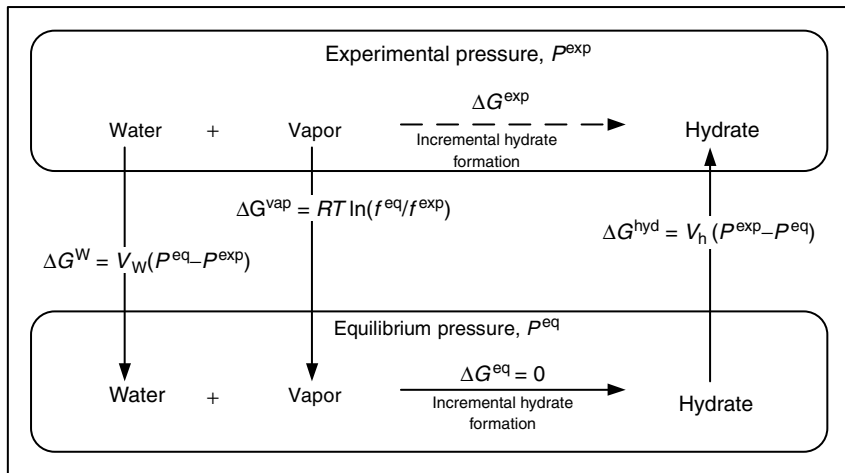


FIGURE 3.18 Isothermal path for calculating ΔG for hydrate formation from water and vapor. (Reproduced and modified from Christiansen, R.L., Sloan, E.D., Jr. in *Proc. 74th Gas Processors Association Annual Convention* (1995). With permission from the Gas Processors Association.)

with

$$\Delta g^{\text{rx}} = \sum_{i=1}^N x_i(\mu_i^{\text{eq}} - \mu_i^{\text{exp}}) \quad (3.6\text{b})$$

and

$$\Delta g^{\text{pr}} = \sum_{i=1}^N x_i(\mu_i^{\text{exp}} - \mu_i^{\text{eq}}) \quad (3.6\text{c})$$

The molar Gibbs free energy difference is obtained between the end points by adding five components of the path:

1. Separation of reactants (gas and liquid) at the experimental pressure ($\Delta g^{\text{sep}} = 0$).
2. Decreasing the pressure of each reactant to the equilibrium value.
3. Combining water and gas at equilibrium to hydrate ($\Delta g^{\text{eq}} = 0$).
4. Compression of product hydrate from equilibrium to experimental pressure.
5. Combining hydrate and unreacted gas and water at experimental pressure ($\Delta g^{\text{comb}} = 0$).

The above path only considers gas and water that react to hydrate. If the molar Gibbs free energy of (1) separation, (3) reaction at equilibrium, and (5)

recombination are all taken as zero, then the Δg^{exp} value is the sum of steps (2) and (4), as in Equation 3.7b.

$$\Delta g^{\text{exp}} = \Delta g^1 + \Delta g^2 + \Delta g^3 + \Delta g^4 + \Delta g^5 \quad (3.7\text{a})$$

$$\Delta g^{\text{exp}} = 0 + \Delta g^2 + 0 + \Delta g^4 + 0 \quad (3.7\text{b})$$

In Equations 3.7a and b, Δg^4 is the isothermal compression of hydrate from equilibrium to experimental pressure, in which the hydrate is assumed incompressible.

$$\mu_{\text{H}}^{\text{exp}} - \mu_{\text{H}}^{\text{eq}} = v_{\text{H}}(P^{\text{exp}} - P^{\text{eq}}) \quad (3.8)$$

In Equations 3.6b and 3.7b in which reacting water and gas are taken from experimental to equilibrium conditions, Δg^2 is divided into two parts, one for the water and a second for the gas: (1) the water (L) value is similar to Equation 3.8, and (2) the gas phase uses a fugacity ratio for each component I:

For the water phase (assumed to be pure water):

$$\mu_{\text{L}}^{\text{eq}} - \mu_{\text{L}}^{\text{exp}} = v_{\text{L}}(P^{\text{eq}} - P^{\text{exp}}) \quad (3.9\text{a})$$

and for each component in the gas phase (assumed to contain no water) we obtain:

$$\mu_i^{\text{exp}} - \mu_i^{\text{eq}} = RT \ln(f_i^{\text{eq}}/f_i^{\text{exp}}) \quad (3.9\text{b})$$

When Equations 3.8 and 3.9a and b are inserted into Equation 3.6, we obtain:

$$\Delta g = v_{\text{L}}(P^{\text{eq}} - P^{\text{exp}}) + RT \sum x_i \ln(f_i^{\text{eq}}/f_i^{\text{exp}}) + v_{\text{H}}(P^{\text{exp}} - P^{\text{eq}}) \quad (3.10)$$

Equation 3.10 is the general case for all driving forces shown in [Table 3.2](#) for three reasons:

1. The $(\mu_{\text{WH}}^{\text{exp}} - \mu_{\text{WL}}^{\text{exp}})$ driving force of Skovborg and Rasmussen is a part of Equation 3.6), shown as the leftmost term in Equations 3.8 and 3.9a.
2. For all hydrates, the second term on the right dominates Equation 3.10, and the first and last terms effectively cancel, because the molar volume of water is within 15% of that of hydrates. The Natarajan et al. driving force of $[(f_i^{\text{exp}}/f_i^{\text{eq}}) - 1]$ is the first term in an infinite series expansion of the second term $[\ln(f_i^{\text{exp}}/f_i^{\text{eq}})]$ in Equation 3.10—acceptable when $(f_i^{\text{exp}}/f_i^{\text{eq}}) < 1.3$.
3. The ΔT driving force is the isobaric equivalent of the isothermal Δg in Equation (3.10). The Gibbs–Helmholtz relation may be applied to

obtain:

$$\Delta g = -(s)\Delta T \quad (3.10a)$$

where the $-(s)$ term relates the Gibbs free energy term to the temperature change.

Arjmandi et al. (2005b) reviewed the work by Christiansen and Sloan (1995) and Kashchiev and Firoozabadi (2002a,b). Arjmandi et al. (2005b) used these previously proposed driving force equations to investigate the effect of pressure on the driving force, and the relationship between driving force and subcooling. Using the equations derived by Christiansen and Sloan (1995) and Kashchiev and Firoozabadi (2002b), the driving force for hydrate formation in a methane–water system was found to be proportional to the degree of subcooling at isothermal and isobaric conditions. In general, at constant subcooling, the driving force decreased with increasing pressure, though the magnitude of the decreased driving force was not considerable above 20 MPa. Therefore, the authors noted that at normal operation conditions of above 20 MPa, subcooling could be used solely to represent the driving force for hydrate formation (see Figure 3.19).

However, for a multicomponent natural gas mixture, at 5–20 MPa, the subcooling was found to significantly underestimate the driving force (the pure methane–water system showed a far better match between driving force and subcooling). However, above 20 MPa, the driving force was matched well by

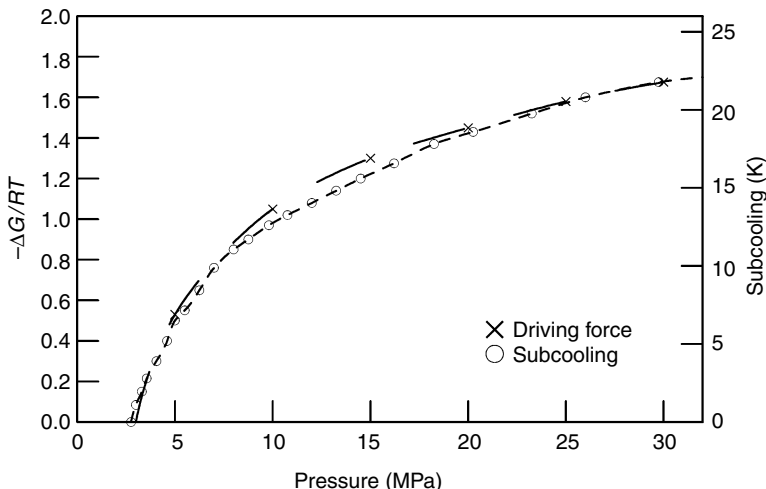


FIGURE 3.19 Variations in driving force and subcooling with pressure calculated at constant temperature, $T = 273.2$ K, for a methane–water hydrate system. (Reproduced from Arjmandi, M., Tohidi, B., Danesh, A., Todd, A.C., *Chem. Eng. Sci.*, **60**, 1313 (2005b). With permission from Elsevier.)

subcooling. Induction time measurements were also reported by Arjmandi et al. (2005b), indicating that the induction times were not a function of pressure for a natural gas–water system.

3.1.5 The “Memory Effect” Phenomenon

There has been a general consensus among hydrate researchers that hydrates retain a “memory” of their structure when melted at moderate temperatures. Consequently, hydrate forms more easily from gas and water obtained by melting hydrate, than from fresh water with no previous hydrate history. Conversely, if the hydrate system is heated sufficiently above the hydrate formation temperature at a given pressure, the “memory effect” will be destroyed. Some experimental observations of the memory effect phenomenon are summarized in Table 3.3.

The observations of the memory effect phenomenon summarized in Table 3.3 have been explained by two opposing hypotheses:

1. Hydrate structure (which is not visible to the naked eye) remains in solution (or on an ice surface) after hydrate dissociation in the following forms:
 - Residual structure (Makogon, 1974; Lederhos et al., 1996; Takeya et al., 2000; Ohmura et al., 2003) consisting of partial hydrate cages or polyhedral clusters (short-range ordered structure). For a significant

TABLE 3.3
Some Experimental Observations of the Memory Effect Phenomenon

Key observation	Researcher(s)
Hydrates form more readily from melted hydrate	Makogon (1974)
Thermal history of water affects hydrate induction times, that is, t_{ind} (hot/warm water) $> t_{\text{ind}}$ (thawed ice or hydrate)	Vysniauskas and Bishnoi (1983); Lederhos (1996); Parent and Bishnoi (1996); Takeya et al. (2000); Ohmura et al. (2003)
Successive cooling curves S_1 , S_2 and S_3 show decreased metastability from the vapor–liquid–hydrate line (Figure 3.20)	Schroeter et al. (1983)
Induction period is eliminated by re-forming hydrate on an ice surface preexposed to xenon	Moudrakovski et al. (2001b)
Induction times decrease when hydrate is reformed from hydrate decomposed for 1 h compared to 12 h	Lee et al. (2005)
Hydrate morphology depends on the dissociation conditions before reformation. A rough surface forms from hydrates decomposed for ≥ 24 h, while a smooth surface forms from hydrates decomposed for only 30 min	Servio and Englezos (2003a)

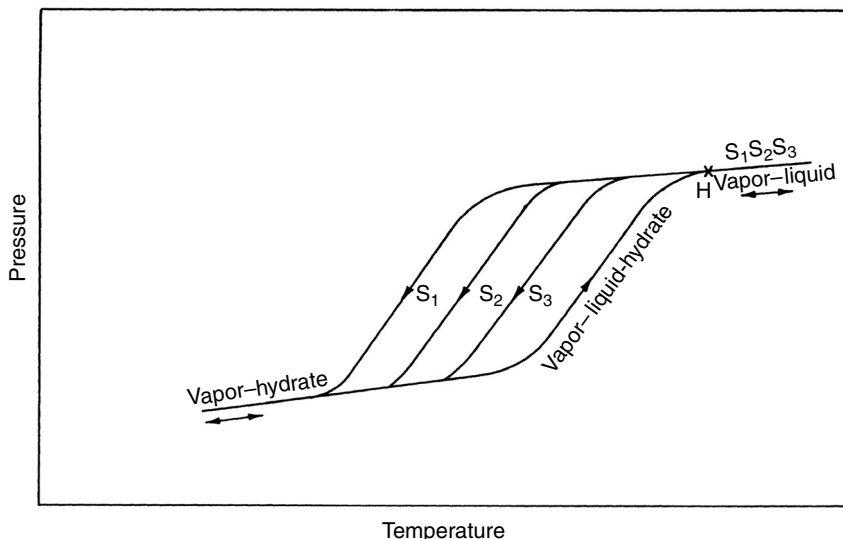


FIGURE 3.20 Successive cooling curves for hydrate formation with successive runs listed as $S_1 < S_2 < S_3$. Gas and liquid water were isochorically cooled into the metastable region until hydrates formed in the portion of the curve labeled S_i . The container was then heated and hydrates dissociated along the vapor–liquid water–hydrate (V–L_w–H) line until point H was reached, where dissociation of the last hydrate crystal was visually observed. (Reproduced from Schroeter, J.P., Kobayashi, R., Hildebrand, M.A., *Ind. Eng. Chem. Fundam.* **22**, 361 (1983). With permission from the American Chemical Society.)

period of time after hydrate dissociation a substantial amount of water structure remains, in a manner analogous to Bridgman's (1912) suggestion that "the disappearance of nuclei (dissociation of ice) is a matter of extraordinary slowness."

- Persistent hydrate crystallites (long-range ordered structure), which were shown from neutron scattering to remain in solution for several hours after increasing the temperature above the hydrate dissociation temperature (Buchanan et al., 2005).
- 2. Dissolved gas remains in solution after the hydrate has decomposed (Rodger, 2000).

Although the evidence of the memory effect phenomenon is plentiful, and clearly not in question, there have been only a limited number of direct molecular-level investigations to verify the above hypotheses. Furthermore, the results of these investigations have so far presented opposing conclusions on which hypothesis is correct.

For example, Chen's (1980) MD simulations seemed to confirm suggestions by Makogon (1974) and Long and Sloan (1996) that both the pentamer ring and the residual structure (short-range order) are stable up to 315 K (cf. simulations by Baez and Clancy, 1994). Conversely, Rodger suggests, based on MD simulations,

that the memory effect is due more to the persistence of a high concentration and retarded diffusion of methane in the melt, than it does to the persistence of metastable hydrate precursors.

The memory effect has important implications for the gas industry. For example, after hydrates initially form in a pipeline, hydrate dissociation should be accompanied by the removal of the water phase. If the water phase is not removed, the residual entity (i.e., residual structure, persistent crystallites, or dissolved gas) will enable rapid reformation of the hydrate plug. Conversely, if hydrate formation is desired, the memory effect suggests that hydrate formation can be promoted by multiple dissociation and reformation experiments (provided the melting temperature is not too high, or melting time is not too long).

3.1.6 State-of-the-Art for Hydrate Nucleation

Hydrate nucleation phenomena are qualitatively summarized with the following statements:

1. Induction times are stochastic, with limited predictability for hydrate onset, particularly at low driving forces, and tend to be apparatus-dependent.
2. At high driving forces and with constant cooling hydrate formation is less stochastic than that at a low driving force or at constant temperature.
3. Hydrate induction times from water are approximately proportional to the displacement from equilibrium conditions (e.g., subcooling). Other variables, which affect nucleation include guest size and composition, geometry, surface area, water contaminants and history, the degree of agitation or turbulence.
4. There are two hypotheses for hydrate nucleation, which are given below:
 - Labile cluster: liquid water molecules are arranged around a dissolved solute molecule in a “prehydrate” structure, with essentially the correct coordination number. A conceptual hypothesis exists for clusters growing to larger structures at an interface.
 - Local structuring: the “prehydrate” structure consists of a locally ordered water–guest structure rather than individual hydrate cavities.
5. Formation of hydrate nuclei (from aqueous liquid) occurs as heterogeneous nucleation, usually at an interface (either fluid + solid, gas + liquid, or liquid + liquid). When both a nonaqueous liquid and vapor are present with water, hydrates form at the liquid–liquid interface.
6. If the temperature for melting hydrate is close to the dissociation temperature, or insufficient time is given to melt hydrate, a memory effect is observed (attributed to residual structure, persistent hydrate crystallites remaining in solution, or dissolved gas) to promote future more rapid hydrate formation. This memory effect is destroyed at temperatures greater than 28°C, or after several hours of heating.

3.2 HYDRATE GROWTH

After the stochastic nature of hydrate crystal nucleation, the quantification of the hydrate growth rate provides some relief for modeling hydrate formation. However, only a limited amount of accurate data exist for the crystal growth rate after nucleation. Most of the nucleation parameters (displacement from equilibrium conditions, surface area, agitation, water history, and gas composition) continue to be important in hydrate growth.

However, during the growth process mass and heat transfer become of major importance. In [Figure 3.1b](#) (the P - T schematic of hydrate growth from water and gas in a closed system) the growth regime is the period between points B and C, in which a significant amount of gas is incorporated into the hydrate phase. The analogous period is labeled “2” in [Figure 3.1a](#). Because the hydrate contains up to 15 mol% gas (at least two orders of magnitude greater than the methane gas solubility) the mass transport of the gas to the hydrate surface is of major importance, and may dominate the process. In addition, the exothermic heat of hydrate formation can also control growth.

3.2.1 Conceptual Picture of Growth at the Molecular Level

On the molecular level, hydrate growth can be considered to be a combination of three factors: (1) the kinetics of crystal growth at the hydrate surface, (2) mass transfer of components to the growing crystal surface, and (3) heat transfer of the exothermic heat of hydrate formation away from the growing crystal surface (see [Section 3.2.3](#) for heat transfer models).

3.2.1.1 Crystal growth molecular concepts

A hypothesis picture of hydrate growth at a crystal is shown in [Figure 3.21](#), modified from Elwell and Scheel (1975). This conceptual picture for crystal growth may be combined with either the labile cluster or local structuring hypotheses for nucleation.

In the figure, step growth of the hydrate crystal is depicted with the following components:

- (i) A guest in a temporal water cluster is transported to the growing crystal surface. Evidence for such clusters is provided in [Section 3.1.1.2](#). The cluster is driven to the surface by the lower Gibbs free energy provided at the crystal surface.
- (ii) The cluster adsorbs on the crystal surface. The solid crystal exerts a force field into the fluid which results in the cluster adhering to the surface. Upon adsorption, some of the water molecules detach from the cluster and diffuse away.

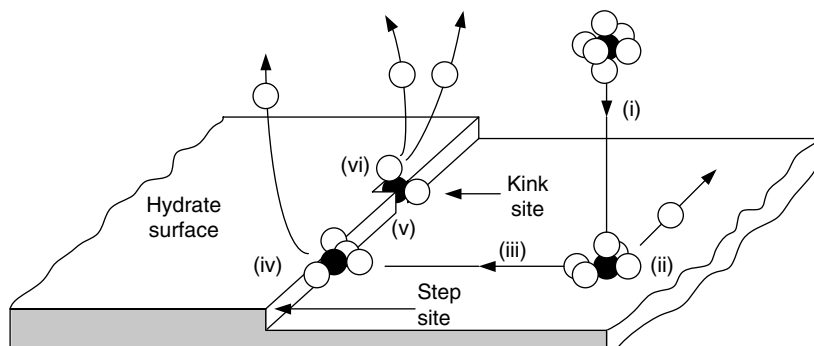


FIGURE 3.21 Hypothesis picture of hydrate growth at a crystal. (Reproduced and modified from Elwell, D., Scheel, H.J. *Crystal Growth from High Temperature Solution* (1975). With permission from Academic Press.)

- (iii) The cluster diffuses over the surface to a step in the crystal. Since the solid force field is perpendicular to the crystal face, the adsorbed species can diffuse only in two dimensions along the surface.
- (iv) The cluster attaches to a crystal step, releasing further solvent molecules. The step is an attractive site because two solid faces of the step exert a force (with two surface–reactant interactions) on the mobile species, in contrast to a single force field (with one surface–reactant interaction) on the flat surface.
- (v) The cluster can now move only in a single dimension, along the step. The cluster diffuses along the step to a kink or defect point in the step.
- (vi) The cluster adsorbs at the kink. The kink is an attractive site because three or more solid faces of the kink exert a larger force on the species than the two forces exerted by the step alone, and
- (vii) The cluster is now immobilized in three dimensions (not shown).

At (ii), (iv), (vi) where the cluster is integrated into the crystal surface, the cluster rearranges itself into the proper cavity and excess solvent molecules are released. If the guest is too large for a cavity (e.g., C₃H₈ cannot fit into a 5¹²) then some time is involved while the empty cavity rearrangement is completed. Water rearrangement into the proper cavity may be the rate-limiting kinetic step. Cavity bonds are completed with the final integration of the cluster into the kink. The final excess cluster molecules are released and the species loses any residual energy of mobility or translation along the crystal surface.

With Avogadro's number of molecules participating in the above process, it would be a mistake to suppose all molecules progress through the above steps in a deterministic manner. With so many particles in motion, every possible combination of attachment is tried. For example, some clusters adsorb directly at a kink without significant diffusion. Other clusters detach from the surface and diffuse away in contrast to our macroscopic observations of growth. However,

in hydrate growth the number of attaching particles (through any number of the above steps) exceed those detaching.

If all possible combinations were equally probable, we would observe stochastic behavior like primary nucleation, so that crystal growth kinetics would be virtually unpredictable. However, a few molecular paths for crystal growth are highly preferred over others, these paths combine in an ensemble to provide the macroscopic observations of crystal growth described in the next section.

The reader should be warned that the above conceptual picture has little supporting evidence from hydrate growth experiments, other than the few single crystal growth studies in Section 3.2.2.1. Nevertheless, it is hoped that such a conceptual picture can promote some understanding of the phenomena involved, if only to serve as a basis for improvement.

All seven steps require time, resulting in a rate of incorporating clusters into the growing crystal surface, which is called crystal growth kinetics. The following two sections consider translation of such a rate into a macroscopic equation for correlation and prediction. It is difficult to say which of the steps control the process, or even if the conceptual picture is valid. However, the first step—species transport to the solid surface—is well established and a brief description is given in Section 3.2.1.2.

3.2.1.2 The boundary layer

All modern pictures and models of hydrate crystal growth include mass transfer from the bulk phases to the hydrate. Unfortunately, some confusion arises due to the fact that two interfaces are usually considered, and the driving forces may not be intuitive for those not familiar with the area. In order to provide a basis for the modeling section, a brief overview of the diffusional boundary layer is given.

The following discussion is excerpted from Mullin (1993) and Elwell and Scheel (1975). Diffusional boundary theory is well-established (see e.g., Bird et al., 1960) and the concept of a boundary “unstirred” layer was introduced a century ago. Noyes and Whitney (1897) proposed that the change in the rate of crystal growth (dm/dt) was controlled by diffusion from the bulk concentration to the crystal (equilibrium) interface.

$$dm/dt = k_d A(c - c^{eq}) \quad (3.11)$$

where c and c^{eq} are the solution concentrations in supersaturated solution and at equilibrium respectively, A is the crystal surface area, and k_d is the coefficient of mass transfer. In his classical work on crystallization, Nernst (1904) stressed the importance of k_d that he equated to (D/δ) , where D is the solute coefficient of diffusion, and δ represents the thickness of a stagnant boundary layer adjacent to the crystal.

Physical evidence for the existence of such a layer was established using interferometry by Berg (1938) and Bunn (1949). Berthoud (1912) and Valeton (1924) modified the concept to include two steps: (1) diffusion to the interface and (2) reaction at the interface. The diffusion step was represented by modifying the

driving force in Equation 3.11 for the solute concentration at the crystal–solution interface, c_i :

$$\frac{dm}{dt} = k_d A(c - c_i) \quad (3.12)$$

The second (reaction) step was for incorporation of the substance into the crystal at the interface:

$$\frac{dm}{dt} = k_r A(c_i - c^{\text{eq}}) \quad (3.13)$$

where k_r is a rate constant for the surface reaction.

In this model (shown conceptually in Figure 3.22) a stagnant boundary layer exists on the fluid side of the crystal interface. Across this layer there exists a concentration gradient taken as the bulk fluid concentration (c) minus the interfacial concentration (c_i) in the fluid. Because the interfacial concentration (c_i) is difficult to measure, Equations 3.12 and 3.13 are usually combined by eliminating c_i to obtain:

$$\frac{dm}{dt} = K' A(c - c^{\text{eq}}) \quad (3.14)$$

where the overall transfer coefficient K' is expressed in terms of the coefficients for diffusion k_d and reaction k_r as:

$$1/K' = 1/k_d + 1/k_r \quad (3.15)$$

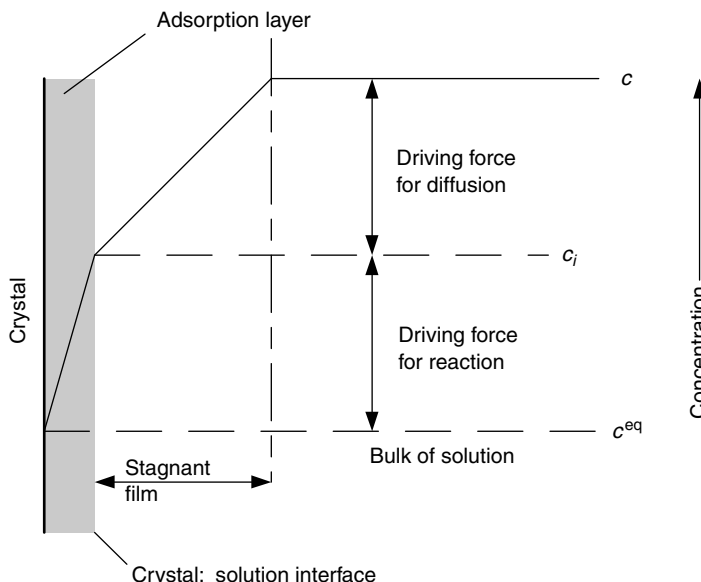


FIGURE 3.22 Conceptual model of mass transfer from bulk phases to hydrate.

Equations 3.12, 3.13, and the final Equation 3.14 are all forms of the classic engineering expression [Rate = (Driving force)/Resistance] where the driving force is expressed as concentration differences. The overall resistance ($1/K'$) can be controlled by a low value of either individual coefficient. The mass transfer coefficient (k_d) controls crystallization when the reaction is very rapid relative to diffusion, but the reaction coefficient (k_r) controls crystallization when diffusion is much more rapid than reaction. In such cases the overall coefficient K' may be approximated by the smaller k value. However, the concentrations in the driving force remain measurable (c) or calculable (c^{eq}) rather than non-measurable (c_i).

Three modifications are often made to the basic Equation 3.14:

1. The crystal growth rate (dm/dt) is represented as the rate of gas consumption,
2. The concentrations (c) are replaced with fugacities, and
3. The controlling process is sometimes considered to be neither reaction nor diffusion through the liquid–crystal boundary layer, but diffusion through the boundary layer at the vapor–liquid interface, as in the Skovborg–Rasmussen model.

When the hydrate growth rate (dm/dt) is measured by the rate of gas consumption (dn_i/dt) the pseudo-steady-state approximation is made. That is, at any instant the rate of gas consumption by the hydrate is assumed equal to the rate of gas consumption from the gas phase. Frequently, experimenters monitor the amount of gas needed to keep the pressure constant in the hydrate vessel so that the driving force remains constant. In such cases, the rate of gas consumption from a separate supply reservoir is measured.

In Equation 3.14, the liquid concentration may be replaced by fugacity if three assumptions are made: (a) constant temperature and pressure, (b) ideal liquid solutions, and (c) constant total molar concentration (c_{tot}). With these assumptions the fugacity (f_i) is related to the concentration (c_i) by the expression:

$$f_i = \left(\frac{\phi_i^L P}{c_{tot}} \right) c_i \quad (3.16)$$

where ϕ_i^L is the fugacity coefficient. With assumptions (a), (b), and (c), the bracketed term in Equation 3.16 is a constant, so that Equation 3.14 may be rewritten as

$$\frac{dn_i}{dt} = KA(f_i - f_i^{eq}) \quad (3.17)$$

where

$$K = \left(\frac{c_{tot}}{\phi_i^L P} \right) K' \quad (3.17a)$$

In the Skovborg and Rasmussen (1994) model discussed in Section 3.2.3.2, Equation 3.17 is replaced with the transfer of the component across the liquid side of the vapor–liquid interface, so that

$$\frac{dn_i}{dt} = k_L A_{(g-l)} (x_i^{\text{int}} - x_i^{\text{b}}) \quad (3.17\text{b})$$

where k_L is mass transfer coefficient across the liquid boundary at the gas–liquid interface, $A_{(g-l)}$ is the area of the gas–liquid interface, and x_i^{int} and x_i^{b} are the interfacial (equilibrium) and bulk mole fractions of “ i ” at the system temperature and pressure.

Equation 3.17b may be regarded as the starting point for the models discussed in Section 3.2.3. In all hydrate growth models the coefficient K is a parameter fitted to kinetic data.

3.2.2 Hydrate Crystal Growth Processes

The different types of hydrate crystal growth processes may be divided into: (1) single crystal growth, (2) hydrate film/shell growth at the water–hydrocarbon interface, (3) multiple crystal growth in an agitated system, and (4) growth of metastable phases. Each of these different growth processes will be discussed in this section.

3.2.2.1 Single crystal growth

Hydrates can grow as single crystals in a water–hydrocarbon solution, particularly under low driving force conditions. Single crystal growth of hydrates is a useful method to investigate the effect of additives on hydrate crystal growth and morphology. Single crystal growth is also required for detailed structural analysis using x-ray and neutron diffraction (see Section 2.1.2.2). Single crystals of tetrahydrofuran and ethylene oxide hydrate, in which both hydrate formers are completely miscible in water, can be readily grown in the laboratory and isolated for structural analysis. Conversely, single crystals of gas hydrates are less easily obtained and isolated, and only a few studies have successfully obtained single crystals of gas hydrates for structural analysis (Udachin et al., 2002).

Figure 3.23 shows single hydrate crystals of structures I and II grown from stoichiometric solutions of ethylene oxide (b) and tetrahydrofuran (a) respectively in quiescent conditions (Larson et al., 1996). The single crystals shown in Figure 3.23 exhibit (110) and (111) crystal planes for structure I and II, respectively. In single crystal growth, it is important to realize that the slowest-growing planes are observed (Mullin, 1993, p. 203), while rapidly growing single crystal planes disappear. Smelik and King (1997) reported similar single crystal shapes from their high pressure single crystal system.

From such single crystal growth studies it is hypothesized that the (111) plane in sII grows slowest because it contains a predominance of hexagonal faces relative

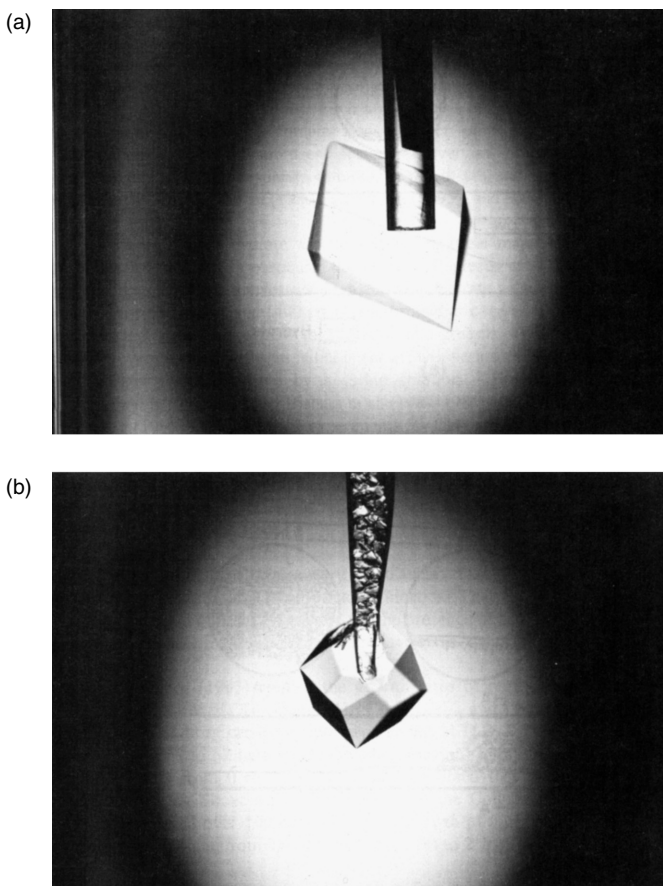


FIGURE 3.23 Photograph of single hydrate crystals of (a) tetrahydrofuran (sII); (b) ethylene oxide (sI). (Photographs by Larsen, 1996.)

to other crystal planes in sII. Crystal planes containing hexagonal faces may grow slowest because hexagonal faces are considerably more strained (120° between O–O–O angles) than are pentagonal faces (108°), relative to either the tetrahedral O–O–O angle (109°) or the water angle (H–O–H of 104.5°). A similar argument is made for the appearance of the (110) plane in sI.

3.2.2.2 Hydrate film/shell growth at the water–hydrocarbon interface

Hydrate growth is typically initiated at the water–hydrocarbon interface (as discussed in Section 3.1.1.4). Measurements of the growth of a hydrate film (or shell) at the water–hydrocarbon interface provides insight into the growth mechanism(s), which can be incorporated into realistic hydrate growth models.

TABLE 3.4
Experimental Studies of Film/Shell Growth at the Water–Hydrocarbon Interface

Hydrate film/shell measurement	Water–hydrocarbon interfacial system	Research group(s)
Film growth at liquid water–hydrate former interface	Water–methane	(Smelik and King, 1997; Makogon et al., 1998; Freer et al., 2001; Taylor, 2006)
Film growth at liquid water–hydrate former interface	Water–fluorocarbon	(Sugaya and Mori, 1996; Ohmura et al., 2000; Ito et al., 2003)
Film growth at liquid water–hydrate former interface	Water–carbon dioxide	(Uchida et al., 1999b; Hirai et al., 2000; Mori, 2001; Uchida et al., 2002; Hirai and Sanda, 2004)
Shell growth on gas (hydrate former) bubble surface	Natural gas bubble in salt water	(Maini and Bishnoi, 1981; Topham, 1984)
Shell growth on gas (hydrate former) bubble surface	Air bubble–ice interface	(Salamatin et al., 1998)
Shell growth on gas (hydrate former) bubble surface	Hydrofluorocarbon gas bubble in water	(Nojima and Mori, 1994)
Shell growth on liquid hydrate former droplet surface	Hydrofluorocarbon droplet in water	(Kato et al., 2000; Ohmura et al., 1999, 2003)
Shell growth on liquid hydrate former droplet surface	Cyclopentane droplet in water	(Taylor, 2006)
Shell growth on liquid hydrate former droplet surface	Liquid carbon dioxide droplet in water	(Shindo et al., 1993)
Shell growth on droplet surface of aqueous solution of hydrate former	Aqueous THF solution droplet in <i>n</i> -decane	(Taylor, 2006)
Shell growth on water droplet surface	Water droplet in methane or carbon dioxide gas	(Servio and Englezos, 2003a; Moudrakovski et al., 2004)
Shell growth on water droplet surface	Water droplet in fluorocarbon gas	(Fukumoto et al., 2001)

Table 3.4 summarizes the different studies that have been performed to measure the growth and morphology of a hydrate film/shell at the water–hydrocarbon interface (where the hydrocarbon can be gas or liquid).

Some common features arising from these studies suggest that the morphology changes are generally similar irrespective of the hydrate former, that is, the supersaturation (or driving force) affects morphology, and there are analogous features between growth behavior at a water–hydrate former planar interface and at the surface of a liquid droplet.

Servio and Englezos (2003a) examined the effect of pressure driving force on the morphology of methane and carbon dioxide hydrates grown from water droplets

(5 and 2.5 mm in diameter) immersed in a hydrate-forming gas atmosphere. The growth experiments were performed at 274.6 K and 2150 kPa (high driving force) or 1000 kPa (low driving force) above the corresponding three-phase hydrate equilibrium pressure ($P_{\text{eq},\text{CH}_4} = 2900 \text{ kPa}$ and $P_{\text{eq},\text{CO}_2} = 1386 \text{ kPa}$ at 274.6 K). The water droplets were placed on a Teflon-coated 316 stainless steel surface to prevent the water droplets from wetting the surface. Each experiment used two or three water droplets in the crystallizer tank. At high driving force, within 5 s after nucleation the surface of the droplet appeared roughened (and dull) with many fine needle-like crystals extruding away from the gas hydrate–water interface (see [Figure 3.24a](#)). This morphological development was the same for methane and carbon dioxide hydrate former gases.

At high driving force, Servio and Englezos suggested hydrate formation comprises three growth phases: (1) the appearance of a hydrate layer (shell) around the water droplet with needle-like crystals, and up to 10 h after nucleation the needle-like crystals grow in size and thickness, (2) the crystal needles collapse onto the hydrate layer covering the droplet, and (3) appearance of depressions in the hydrate layer surrounding the water droplet, which occurred within 10–15 h to a couple of days in some experiments. At a high driving force, hydrate is likely to nucleate and grow at many different locations, compared to a low driving force, where hydrates can form in a more regular manner and location.

Conversely, at low driving force conditions, there was no evidence of needle-like crystals on the droplet surface, which instead had a smooth and shiny texture ([Figure 3.24b](#)). This contrast in morphologies at high and low driving forces was suggested to be because of a larger number of nucleation sites being formed at high driving force compared to that at low driving force. This is consistent with Mullin's (2001) suggestion that the rate of nucleation (number of nuclei formed per unit time per unit volume) increases with the degree of supersaturation. The degree of supersaturation is proportional to the driving force. Therefore, at high driving force many nucleation sites are present with faster nucleation kinetics and therefore this may result in more random crystal growth and hence a rougher surface. Associated with this faster kinetics is the heat limited growth process, as indicated by the formation of needle-like dendritic crystals. In contrast, at low driving force there are fewer nucleation sites, with growth occurring more slowly and across the droplet surface until it is covered with a smooth hydrate layer.

The three growth phases suggested from the work of Servio and Englezos (2003b) above, are analogous to the results obtained by Taylor (2006) on the growth of cyclopentane hydrate on the surface of a water droplet immersed in cyclopentane. In these studies a water droplet was placed on a cantilever and submersed in cyclopentane, before being nucleated by another hydrate particle ([Figure 3.25a](#)). On contact, nucleation occurs, followed by the formation of a thin porous hydrate shell around the water droplet within a few minutes ([Figure 3.25b](#)). About 0.5 h after nucleation, depressions were observed on the droplet surface ([Figure 3.25c](#)).

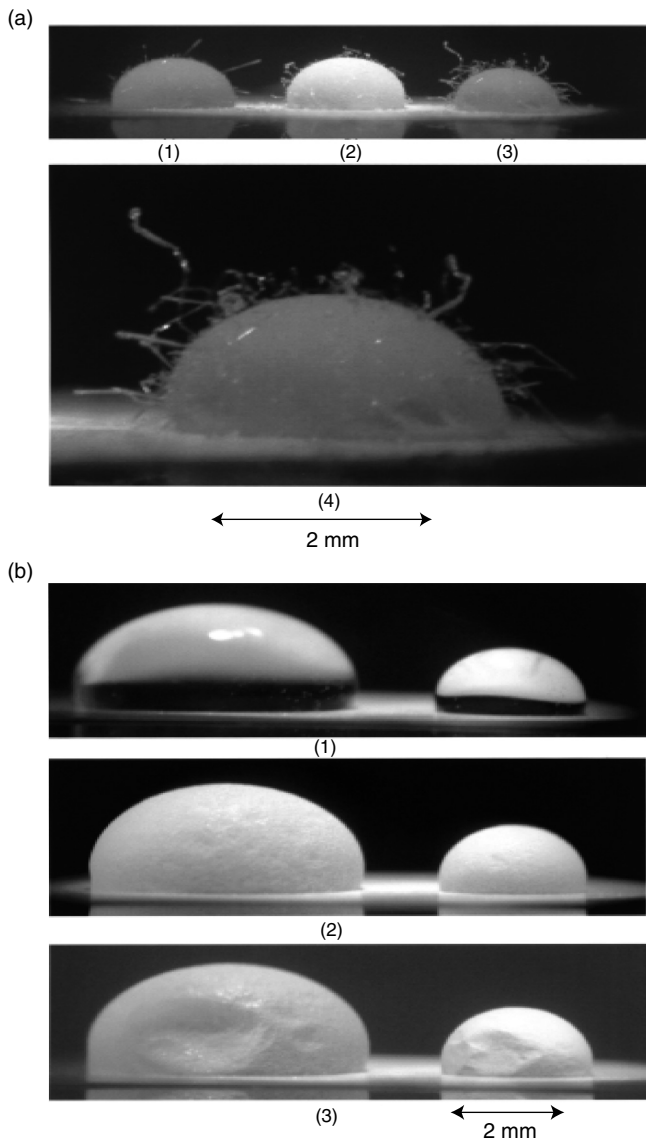


FIGURE 3.24 (a) Methane hydrate covering the surface of water droplets (1, 2, 3) under high driving force, 10 min after nucleation. Image (4) is a magnified view of droplet (3), and (b) methane hydrate covering two water droplets under low driving force at three different times: (1) at $t = 0$, (2) at $t = 10$ h where the water droplet is covered by hydrate, (3) at $t = 25$ h where the water droplet is covered by hydrate and depressions in the hydrate layer appear. (Reproduced from Servio, P., Englezos, P., *AIChE J.*, **49**, 269 (2003a). With permission from Wiley Interscience.)

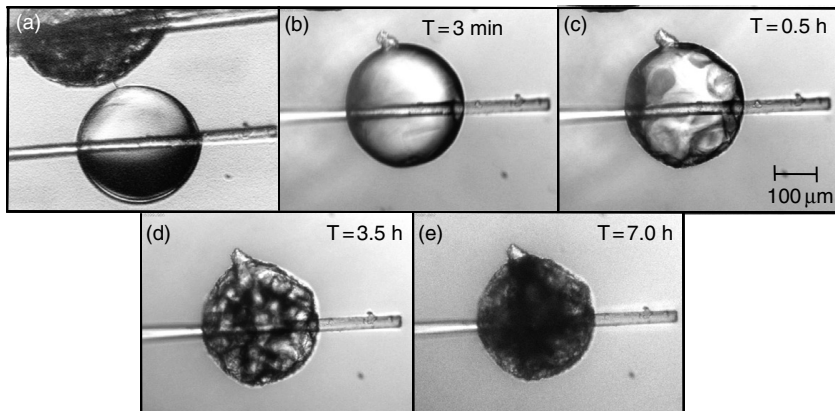


FIGURE 3.25 Cyclopentane hydrate formation from a water droplet: (a) initial contact, (b) hydrate shell formation around the water droplet, (c) depressions formed on the hydrate shell, (d) conversion of interior water to hydrate, indicated by darkening, (e) almost completely converted hydrate. (From Taylor, C.J., *Adhesion Force between Hydrate Particles and Macroscopic Investigation of Hydrate Film Growth at the Hydrocarbon/Water Interface*, Master's Thesis, Colorado School of Mines, Golden, CO, (2006). With permission.)

The depressions may be because of cyclopentane diffusing through the porous hydrate layer converting the interior of the shell into hydrate. The internal droplet volume is decreased as the water is converted to hydrate and part(s) of the droplet collapse. Alternatively, water may diffuse from the interior droplet to the outer shell surface to react with hydrate former, also resulting in a decrease in internal droplet volume. Staykova et al. (2003) suggest that both hydrate former and water mass transport should easily occur through the porous hydrate layer. Further hydrate conversion was indicated by darkening of the droplet (Figures 3.25d,e).

The above growth processes of the conversion of a water droplet to hydrate particle appear analogous to film growth occurring at a planar water-hydrocarbon surface. Growth studies at a planar interface show the hydrate film grows laterally across the entire interface. Over time, the hydrate layer thickens to a final thickness that depends on the degree of subcooling. The hydrate film thickness and growth rate have been determined using gas consumption coupled with video imaging (Freer et al., 2001; Taylor, 2006), or from measurements using a micrometer (Makogon et al., 1998). The hydrate film thickness is shown to increase with increasing subcooling (Figure 3.26). An initial film thickness of 12 and 6 μm was measured for cyclopentane hydrate and methane hydrate, respectively. A similar initial film thickness of 10 μm was measured using laser interferometry for a liquid hydrofluorocarbon (CH_2FCF_3)–liquid water interface (Ohmura et al., 2000).

Raman measurements and solubility predictions of the guest molecule concentration within the bulk aqueous phase suggest that the hydrate film thickens into the water phase (Makogon et al., 1998; Subramanian and Sloan, 2000; Subramanian, 2000). The Raman peak area for methane (C–H

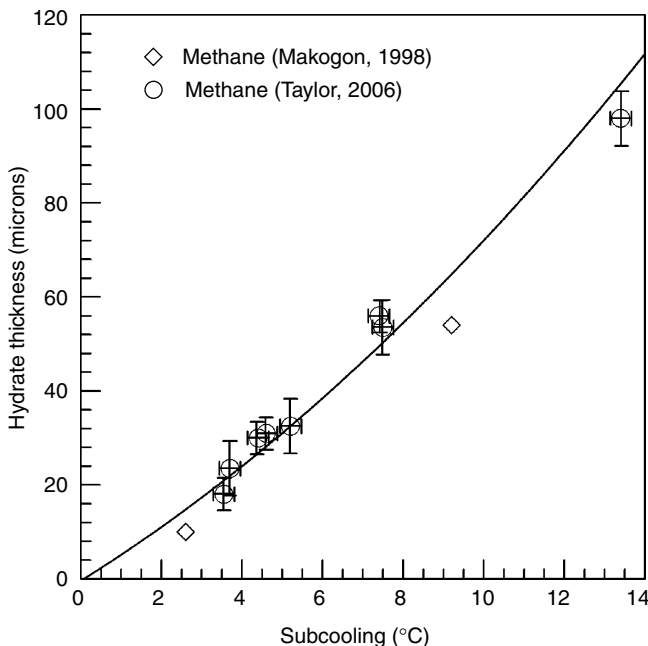


FIGURE 3.26 Final methane hydrate film thickness vs. subcooling. (From Taylor, C.J., *Adhesion Force between Hydrate Particles and Macroscopic Investigation of Hydrate Film Growth at the Hydrocarbon/Water Interface*, Masters Thesis, Colorado School of Mines, Golden, CO (2006). With permission.)

symmetric stretching vibration) dissolved in water is directly proportional to the concentration of dissolved methane. On decreasing the temperature below the hydrate equilibrium temperature (Points A to B, Figure 3.27a), the intensity of the dissolved methane peak increases slightly, indicating a slight increase in methane concentration in the aqueous phase. However, after hydrate formation occurs (Point C), the intensity of the dissolved methane peak decreases, indicating a decrease in the methane concentration. Upon further cooling (Points D and E), the intensity again decreases. This corresponds to the predicted decrease in methane concentration as the temperature is decreased along the C_{sh} curve (C_{sh} is the methane solubility curve with hydrate present; Figure 3.27b; dashed line). Throughout the cooling process, the methane concentration was qualitatively predicted from the solubility curves (C_s , without hydrate and C_{sh} , with hydrate; determined from CSMGem).

The trends shown from the predicted curves, C_{sh} and C_s , are in qualitative agreement with corresponding dissolved methane Raman peak intensities. Therefore, the Raman spectra (Figure 3.27a) support the proposed mechanism that hydrate growth occurs in part as a result of methane diffusing from the bulk aqueous phase to the hydrate film formed at the vapor–liquid interface. This decreases the methane concentration in the bulk water phase. Hydrate growth from an aqueous

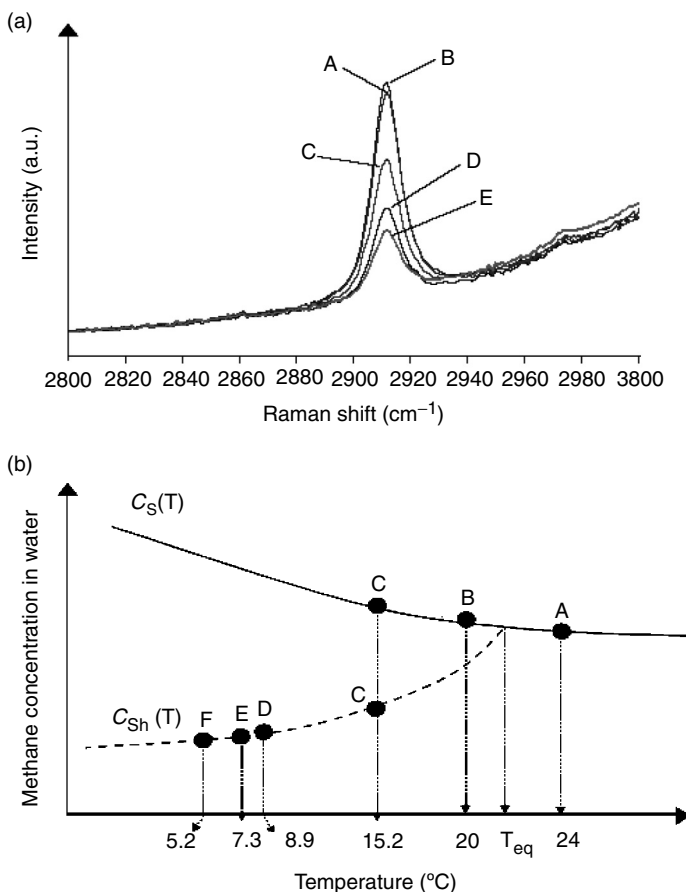


FIGURE 3.27 Methane hydrate film development at the water–methane interface from dissolved methane in the aqueous phase, as indicated from Raman spectroscopy (a) and methane solubility predictions (b). (a) A series of Raman spectra of dissolved methane collected at different temperatures during the continuous cooling process. Spectra marked A through E correspond to temperatures of 24°C, 20°C, 15.6°C, 10.2°C, and 2.8°C, respectively. (b) A schematic illustration of temperature dependencies of the equilibrium methane concentration in liquid water (C_S = without hydrate, C_{Sh} = with hydrate). The scale of the vertical axis is arbitrary, but the Raman peak area is proportional to methane dissolved in water. Points A through F correspond to different temperatures during the continuous cooling process. (From Subramanian, S., *Measurements of Clathrate Hydrates Containing Methane and Ethane Using Raman Spectroscopy*, Ph.D. Thesis, Colorado School of Mines, Golden, CO (2000). With permission.)

solution of water and dissolved methane has been also suggested by Tohidi et al. (2001, 2002) from glass micromodel experiments.

A conceptual picture of the proposed mechanism for hydrate film growth at the hydrocarbon–water interface based on the above experimental results is given

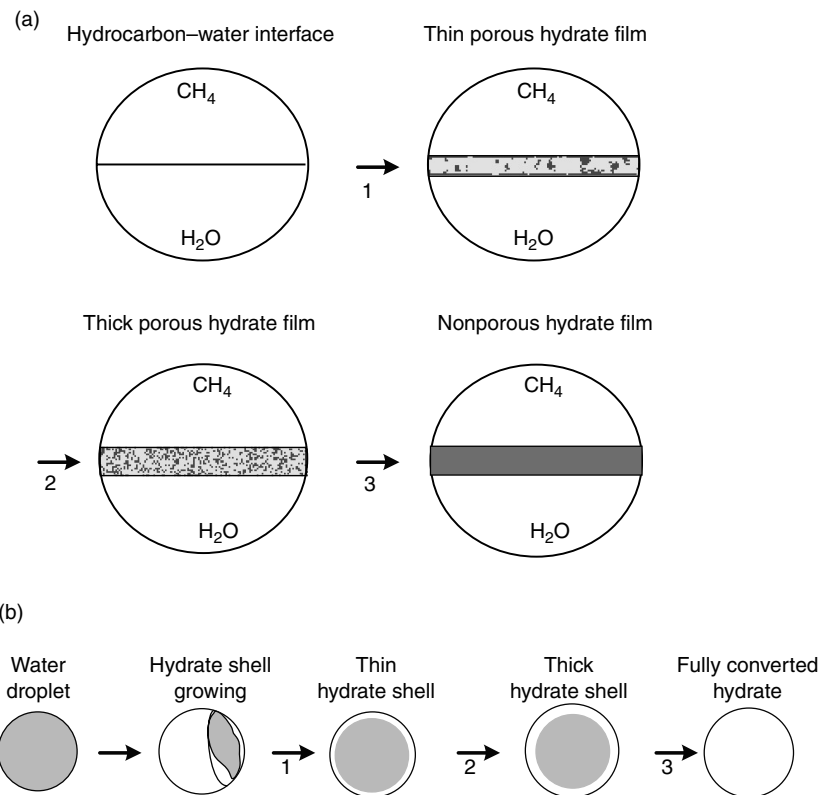


FIGURE 3.28 (a) Schematic of the proposed mechanism for hydrate film formation at a hydrocarbon–water interface. Step 1: Propagation of a thin porous hydrate film across the hydrocarbon–water interface. Step 2: Film development. Step 3: Hydrate film solidification (Taylor, 2006; Subramanian, 2000) and (b) Schematic of the proposed mechanism for hydrate formation from a water droplet. Step 1: Propagation of a thin porous hydrate shell (film) around the water droplet. Step 2: Shell development. Step 3: Bulk conversion of the droplet interior to hydrate (Taylor, 2006).

in Figure 3.28a. This model is extended to hydrate formation from the surface of a water droplet in Figure 3.28b. Figure 3.28b is based on both the film growth and droplet conversion experiments detailed above.

Information on the mesoscopic and microscopic processes occurring at the surface of ice particles during hydrate particle formation has been obtained from scanning electron microscopy (SEM; Staykova, 2003; Kuhs et al., 2005; Stern et al., 2005), nuclear magnetic resonance (NMR) microimaging (Moudrakovski et al., 2004), and neutron diffraction (Henning et al., 2000). Direct evidence for hydrate shell formation has been obtained from scanning electron micrographs recorded for methane hydrate samples (Stern et al., 2005). In these experiments, hydrate was formed from ice grains by cycling the temperature below and just

above the ice point. The authors suggest that the mesoporous structure (Figures 3.29c,d) of the hydrate surface (or shell around the melted ice/water droplet) allows liquid water from the interior of the shell to leak out of the shell, hence leaving hollow shells of hydrate (Figures 3.29a,b).

Figure 3.30 shows a field emission FE-SEM image of the porous structure of a typical methane hydrate single crystal formed from an ice particle (Staykova, 2003). Mean pore sizes on the order of several hundred nm (macropores) were determined from the FE-SEM images for single crystals of methane, argon and nitrogen hydrate. Pore sizes of several 10's of nm (mesopores) were identified for carbon dioxide hydrate. These pore channels would allow water and gas to be transported through the hydrate layers. As the permeability of the hydrate layer decreases, transport would become more difficult.

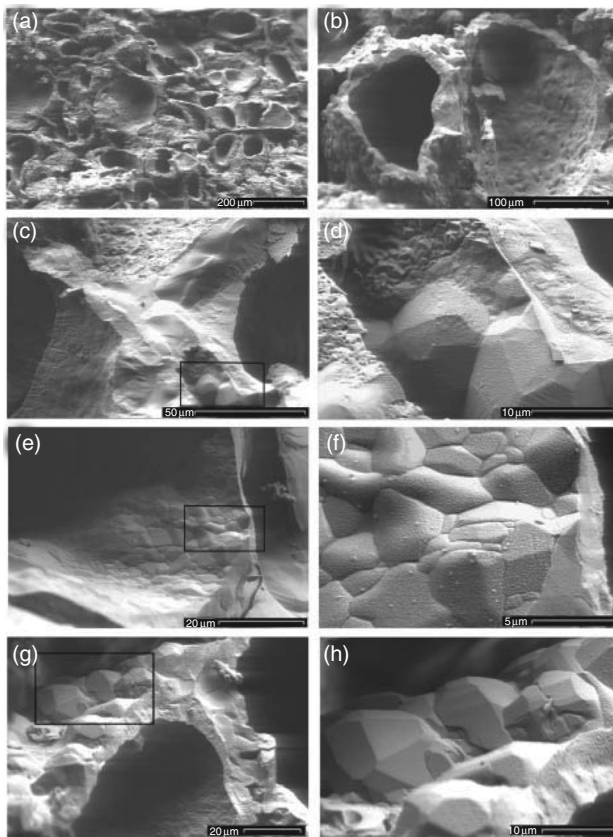


FIGURE 3.29 Scanning Electron Micrographs (SEM) of methane hydrate. (a, b) Hydrate shells; (c, d) mesoporous hydrate surface, (e, f) quenched hydrate, (g, h) hydrate crystal edges. (Reproduced from Stern, L., Circone, S., Kerby, S., Durham, W., in *Proc. Fifth International Conference on Gas Hydrates* (2005). With permission.)

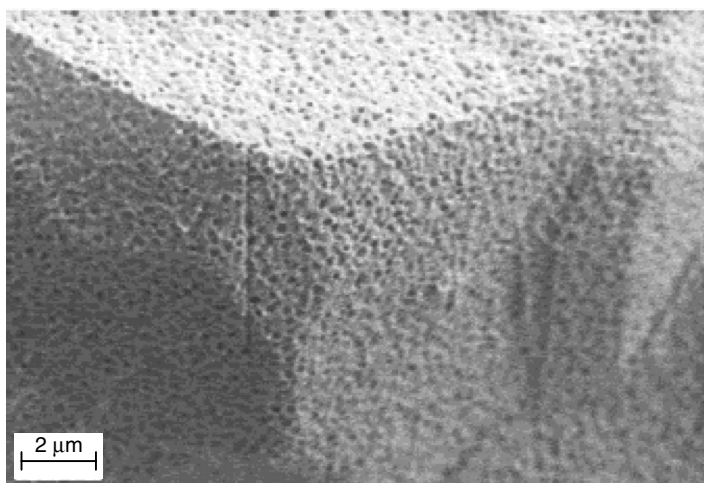


FIGURE 3.30 Field emission scanning electron microscopy image of the submicron porous structure of methane hydrate after 2 weeks of reaction at 60 bar, 265 K. (Reproduced from Staykova, D.K., Kuhs, *J. Phys. Chem. B*, **107**, 10299 (2003). With permission from the American Chemical Society.)

Similarly, hydrate shell formation has been observed directly using ^1H NMR microimaging (Moudrakovski et al., 2004). In these measurements ice particles were converted above the ice point to hydrate particles of methane (at 172 bar, 277 K) and carbon dioxide (58 bar, 275 K). The microimaging method was able to clearly detect hydrate shells around water droplets (Figure 3.31). The results also show that in less common cases, the thickness of the hydrate shells increases indicating the reaction is limited to gas diffusion through the hydrate shell. After some time the interior of the droplet then converts to hydrate. However, the most common observation was that on formation of the hydrate shell around the water droplet, rather than shell thickening, the bulk water of the droplet was converted to hydrate. Similar results were obtained for methane hydrate formation from water droplets suspended in iso-octane. The microimaging results also revealed the heterogeneous nature of the nucleation and growth of the water droplets to hydrate particles.

In summary, the microimaging technique provides a powerful tool to study directly the mechanism of converting water droplets to hydrate particles. The results reported indicate that provided the gas hydrate former can diffuse into the interior droplet, hydrate growth can proceed in the bulk interior droplet away from the hydrate shell–water interface, as well by growing out from the hydrate shell resulting in shell thickening.

In situ neutron diffraction studies have provided insight into the mechanism of surface conversion of ice particles to carbon dioxide hydrate particles (Henning et al., 2000). The experiments were performed at 230–276 K and around 6.2 MPa. It was proposed from these measurements that after the initial period of fast

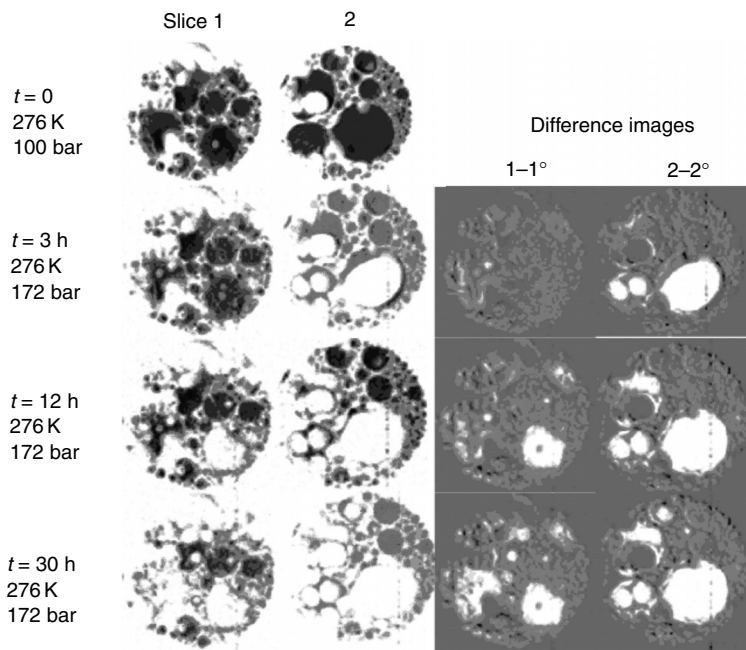


FIGURE 3.31 ^1H NMR microimages of methane hydrate formation as a function of time. Left: Images for two slices; right: difference images; in both, white represents hydrates. (Reproduced from Moudrakovski, I.L., McLaurin, G.E., Ratcliffe, C.I., Ripmeester, J.A., *J. Phys. Chem. B*, **108**, 17591 (2004). With permission from the American Chemical Society.)

conversion to hydrate on the surface of the ice particles, the process is controlled by diffusion of carbon dioxide molecules through the hydrate layer. After diffusion through the hydrate layer, hydrate formation proceeds from carbon dioxide and water molecules in a quasi-liquid layer (or premelting layer). This is in agreement with the findings of Stern et al. (1998) who reported enhanced methane hydrate formation at a liquid-like surface film on fine ice grains (about 200 micrometers) from optical cell experiments.

3.2.2.3 Crystal growth with interfacial agitation

Analysis of hydrate formation data can be obtained from a tabulation of gas consumption during hydrate formation as a function of time measured in stirred reactors. Formation data thus require either a table (or a plot) of individual experiments. Such a prospect is not viable in this monograph, since the literature hydrate formation data contain a large number of experiments with questionable transferability between apparatuses. Instead an overview of experimental conditions is presented below. The reader is referred to theses and subsequent publications of Englezos (1986), Dholobhai (1989), Skovborg (1993), Bansal (1994), and Turner (2005) for typical data.

As with most hydrate kinetic studies, multiple major works have come from Bishnoi's laboratory. In particular, the work of Englezos et al. (1987a,b) and Englezos and Bishnoi (1988) is a milestone in quantifying hydrate growth. Englezos' experiments were performed in a mixed (400 rpm) reactor held at constant pressure (0.6–8.9 MPa) and constant temperature (274–282 K). The growth of CH₄, C₂H₆, and CH₄ + C₂H₆ hydrates were measured for an initial linear growth period (<2 h) after appearance of the hydrate phase, indicated by a turbid solution. The data for these studies are summarized in two reports by Bishnoi et al. (1984–1985, 1986) and have been digitized by Skovborg (1993). A total of 17 experiments for CH₄ were performed by Englezos in the temperature range from 274 to 282 K and the pressure range of 2.3–9.3 MPa. For C₂H₆ a total of 9 experiments were done in the same temperature range, but at a pressure range from 0.7 to 2.2 MPa. For mixtures of CH₄ + C₂H₆ 23 kinetic data sets were measured; 8 sets for mixtures of 75%CH₄ + 25%C₂H₆, 6 sets for equimolar mixtures, and 9 sets for 25%CH₄ + 75%C₂H₆. Clarke and Bishnoi (2005) performed further measurements on CO₂ hydrate growth and found the intrinsic rate constant varied from 3.214×10^{-3} to 6.423×10^{-3} mol/(m²Pa s) over the temperature range 274–279 K and pressure range 1.6–3.0 MPa.

Also in Bishnoi's laboratory, Dholabhai et al. (1993) studied the effect of electrolytes on methane hydrate formation kinetics. They found that after the equilibrium fugacity (or driving force) is adjusted for the presence of salt, hydrate growth kinetics are quantitatively described by the pure water kinetics model of Englezos.

Skovborg (1993) studied the growth rates of pure components of CH₄, C₂H₆, C₃H₈, and mixtures of CH₄ + C₂H₆, CH₄ + C₂H₆ + C₇H₁₆, and a North Sea fluid. Skovborg carried out 98 experiments at D.B. Robinson, Ltd. over a pressure range from 0.75 to 52 bars with subcooling ranging from 1.2°C to 7.5°C and hydrocarbon liquid volumes from 0% to 92%. It should be noted that the pressure (driving force) decreased during Skovborg's experiments. At the Colorado School of Mines, Bansal (1994) performed over 100 experiments on growth of C₂H₆ and CH₄ + C₃H₈ hydrates at temperatures ranging from 0°C to 4°C and pressures of up to 2.7 MPa.

Laser light scattering has been also applied to measure hydrate growth rates and particle size distributions in high pressure stirred reactors (Nerheim, 1993; Parent and Bishnoi 1996; Nesterov and Feklistov, 1999; Servio et al., 2000; Clarke and Bishnoi, 2000; Clarke and Bishnoi, 2001, 2005; Turner, 2005) and in a flow loop system (at the ExxonMobil facility). An *in situ* particle size analyzer (FBRM, focused beam reflectance measurement method; Lasentec) has been recently applied at CSM together with a particle video microscopy method (PVM, which visualizes particles illuminated with an array of near-infrared lasers; Lasentec) to measure hydrate particle formation and agglomeration.

3.2.2.4 Growth of metastable phases

The appearance of metastable phases during hydrate growth can provide valuable insight into the molecular mechanism of hydrate growth, as well as an increased

level of understanding of the possible origin of thermodynamic structural transitions. Molecular measuring tools such as Raman and NMR spectroscopy, and neutron and x-ray diffraction can be used to detect the appearance of metastable phases. That is, the characteristic spectroscopic or diffraction peak(s) for a hydrate structure that is not thermodynamically stable can be detected during hydrate growth.

Coexistence of sI and sII carbon dioxide hydrate has been detected from x-ray diffraction measurements during hydrate growth (Staykova and Kuhs, 2003). Similarly, metastable sII hydrate phases were detected using NMR spectroscopy during sI xenon hydrate formation (Moudrakovski et al., 2001a) and during sI methane/ethane hydrate formation (Bowler et al., 2005; Takeya et al., 2003).

Changes in the large-to-small cage occupancy during hydrate growth detected using NMR spectroscopy also suggest the presence of metastable phases. NMR studies showed that the large-to-small cage occupancy of sI xenon hydrate was around 1.0 initially and changed to a value of around 3–4 after rapid growth commenced. Therefore, during the induction period, the hydrate clusters were composed of a larger number of occupied small cages than large cages (Moudrakovski et al., 2001b). Similar results were found for methane hydrate using Raman spectroscopy (Subramanian, 2000).

3.2.3 Correlations of the Growth Process

Table 3.5 summarizes the different hydrate growth models that have been developed by various research groups. Three major correlations for hydrate growth exist:

1. Intrinsic growth kinetics
2. Mass transfer limited
3. Heat transfer limited

This section presents models from each of the correlations (1–3), with a brief critique. One should approach the use of any kinetic model with extreme caution for three reasons:

1. Hydrate nucleation (the initiation of growth, occurring during the induction period) is a stochastic process (with significant scatter in the data at low driving force under isothermal conditions).
2. Every model for hydrate formation may be apparatus-dependent. If the data for the model were generated in a high pressure reactor, there is no assurance that the data would be translatable to (for example) a natural gas pipeline.
3. Most of the data were determined for sI while natural gas typically forms sII; crystal structure is a significant factor in the rate of crystal growth.

TABLE 3.5
A Summary of the Different Hydrate Growth Models

Growth model	Driving force/model features	Researchers
Growth kinetics	$(f - f_{eq})$	(Englezos et al., 1987a,b)
Growth kinetics	$(f - f_{eq})$ Minor modification to Englezos' model	(Malegaonkar et al., 1997)
Mass transfer	$(x_{int}^i - x_b^i)$ Simplification/modification to Englezos' model	(Skovborg and Rasmussen, 1994)
Mass transfer	Based on phase field theory	(Svandal et al., 2005)
Mass transfer	Based on Monte Carlo cellular automata	(Buanes et al., 2005)
Heat transfer	Curved film front growth on water–hydrate former interface	(Uchida et al., 1999a)
Heat transfer	Curved film front growth on water–hydrate former fluid interface	(Mori, 2001)
Heat transfer	Straight film front growth on water side of water–hydrate former interface	(Freer et al., 2001; Mochizuki and Mori, 2005, 2006)

3.2.3.1 Growth kinetics—the Englezos–Bishnoi model

The role of hydrate intrinsic kinetics has been more recently suggested to play a smaller role in hydrate growth in real systems than heat and mass transfer effects. In view of this, the discussion on the kinetics models is only briefly presented here. For a more thorough treatment, the reader is referred to the original references (Englezos et al., 1987a,b; Malegaonkar et al., 1997).

Englezos et al. (1987a,b) generated a kinetic model for methane, ethane, and their mixtures to match hydrate growth data at times less than 200 min in a high pressure stirred reactor. Englezos assumed that hydrate formation is composed of three steps: (1) transport of gas from the vapor phase to the liquid bulk, (2) diffusion of gas from the liquid bulk through the boundary layer (laminar diffusion layer) around hydrate particles, and (3) an adsorption reaction whereby gas molecules are incorporated into the structured water framework at the hydrate interface.

Modifications to the model by Englezos et al. were later made to remove some minor inconsistencies and to account for the high solubility of carbon dioxide in water (Malegaonkar, et al., 1997). The last two steps are concepts with initial basic equations discussed in Section 3.2.1. Similarly to Equation 3.17, Englezos modeled steps (2) and (3) using Equation 3.18, where at steady state the rates of the two steps are assumed equal. Therefore, the rate of growth per particle is given by:

$$(dn_i/dt)_p = K^* A_p (f_i^b - f_i^{eq}) \quad (3.18)$$

with

$$1/K^* = 1/k_r + 1/k_d \quad (3.19)$$

where

$(dn_i/dt)_p$ = number of gas moles consumed per second by the hydrate

A_p = the surface area of each particle

f_i^b = fugacity of component i in the bulk liquid

f_i^{eq} = equilibrium fugacity of component i in the liquid at the hydrate interface

K^* = hydrate formation growth rate constant, representing a combined rate constant for diffusion (mass transfer) and adsorption (reaction) processes

k_r = reaction rate constant

k_d = mass transfer coefficient through the film around the particle

$(f_i^b - f_i^{eq})$ defines the overall driving force.

However, as with any model, it is well to recognize the limitations before attempting usage. Below are some inherent restrictions in the Englezos–Bishnoi–Malegoankar model:

1. The data were modeled with one fitted parameter (K^*) for hydrate growth of simple hydrate formers of methane, ethane, carbon dioxide. Since all these model components form sI hydrate, the model should be used with caution for sII and sH.
2. The model was for linear growth during the first 100 min after hydrate nucleation, starting from the time of visual observation of hydrates (the turbidity point). In their critique, Skovborg and Rasmussen (1994) note that, when the model is extrapolated by an order of magnitude, increasing growth (curvature) is observed with time, in contrast to long-time data.
3. The model is very sensitive to the number of moles consumed at the turbidity point, to which there is no easy access.
4. In calculating the critical radius it was assumed that the hydrate remains at the equilibrium pressure, not the system pressure. This assumption indicates a system force imbalance and ignores the final term in Δg .
5. From our current knowledge, it is suggested that intrinsic kinetics typically plays a minor role in hydrate formation in real systems (turbulent pipeline flow), and instead mass and heat transfer may play a larger role in determining the rate of hydrate formation.

Even with the above restrictions, the Englezos–Bishnoi model was a pioneering exercise that provided a foundation for further work. The data obtained were measured very carefully, and thus can be fit with all kinetic models. It is fair to say that other macroscopic kinetic experiments follow in the footsteps of the Englezos–Bishnoi work.

3.2.3.2 Mass transfer—the Skovborg–Rasmussen model

Skovborg and Rasmussen (1994) studied the Englezos–Bishnoi model and noted two restrictions in addition to limitations 2 and 3 in the last section:

1. The secondary nucleation constant was very low (10^{-3}) suggesting that no secondary nucleation exists, and that all particles were of the same size and grow at the same rate. Therefore, Skovborg and Rasmussen suggested that the crystallization population balance could be removed from the model.
2. The value of K^* may have been too high, caused by an error in the mass transfer coefficient through the liquid film, k_L . Skovborg suggests that values of k_L were obtained at solubility conditions without hydrate formation, perhaps leading to an error. (See Handa's solubility predictions in [Section 4.1.6](#)). Skovborg noted that a 50% error in k_L will result in an error of two orders of magnitude in K^* .

The above observations encouraged Skovborg and Rasmussen to simplify the Englezos–Bishnoi model. They assumed that the entire hydrate process could be modeled as a mass transfer restriction of the gas through the liquid film at the gas–liquid interface. As such, their model reduced the number of differential equations to a single equation:

$$\frac{dn}{dt} = k_L A_{(g-l)} c_{wo} (x_{int} - x_b) \quad (3.20)$$

where

$A_{(g-l)}$ = gas–liquid interface area, (79.3 cm^2 at 300 rpm in Englezos et al.,

1987a)

c_{wo} = initial concentration of water

x_{int} = bulk liquid mole fraction of the component.

Skovborg re-analyzed the Englezos kinetic data and obtained mass transfer coefficients of 4.076×10^{-5} and $5.457 \times 10^{-5} \text{ m/s}$ for CH_4 and C_2H_6 , respectively.

A Perspective on the Skovborg–Rasmussen Model. With its simplification, the Skovborg–Rasmussen model represents perhaps the most approachable mathematical treatment for mass transfer controlled growth. As with all models, it should be studied carefully and used with caution. There are several limitations to the model:

1. Absolute average deviations to the fit of the Englezos–Bishnoi data for CH_4 , C_2H_6 , and their mixtures, are 22%, 14%, and 30% respectively, relative to the experimental inaccuracies on the order of 10–20%. That is, the mixture predictions may be in error by $\pm 30\%$. While many predictions work well, others failed for methane at long times.

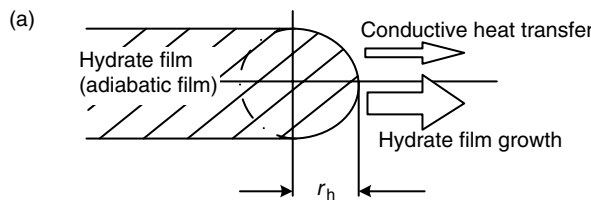
2. There is no published evidence that the model parameters are apparatus-independent, or that the fit can be extended to other systems.
3. Surface area A deviations from 30% to 70% were calculated for identical runs of methane and ethane, suggesting a self-consistency problem.
4. The model is sensitive to errors in driving force, and the driving force errors are systematic in the model.
5. The model appears to be a data fit, rather than have theoretical significance.

3.2.3.3 Heat transfer models

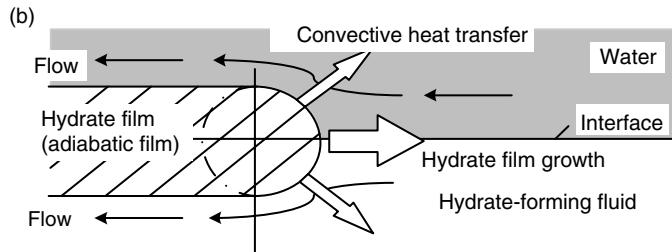
Lateral growth of a hydrate film across the water–gas interface can be described by various models (Figures 3.32a through d). The Uchida et al. (1999a) model (Figure 3.32a) has been based on their experiments performed on a water droplet surface submerged in liquid carbon dioxide. In this model, hydrate crystals form only at the front of the hydrate film and the front is maintained at the three-phase (water–guest–hydrate) equilibrium temperature. Steady heat transfer from the front to the water and guest fluid is assumed. Assuming that heat removed from the front is balanced with heat generated by hydrate formation (exothermic process), Uchida et al. related the linear growth rate of the hydrate film along the interface (v_f) to the hydrate film thickness (δ), and the degree of subcooling (ΔT). δ was determined by fitting the calculated $v_f - \Delta T$ plot to the corresponding experimental data.

Mochizuki and Mori (2005, 2006) suggest that the major problem with the Uchida et al. (1999a) model is the formulation of the conductive heat transfer from the film front, which has little physical reasoning. Direct measurements of the hydrate film thickness under pressure are generally far more difficult than lateral film growth measurements. Therefore, it was recognized that the Uchida et al. (1999a) model provides a method of determining the hydrate film thickness.

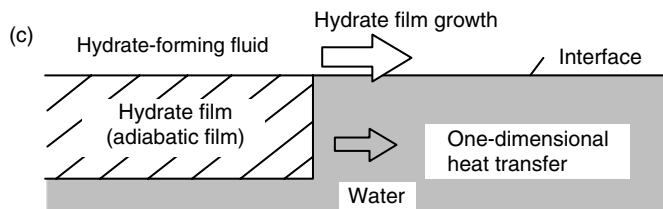
An alternative model is that presented by Mori in 2001 (Figure 3.32b), which is again based on lateral growth of the hydrate film on the interface between a stagnant water pool and a guest fluid. However, in this model, there is a countercurrent flow that occurs at a velocity opposite in sign but equal in magnitude to the velocity of the film front. The heat of hydrate formation released at the film front is assumed to be removed away from the front to the liquid phases by steady convective heat transfer. The film front is semicircular in shape and held at the three-phase equilibrium temperature, as in the Uchida et al. (1999a) model. This second model gives better agreement with the experiments for the $v_f - \Delta T$ relations than the first model. However, Mochizuki and Mori (2005, 2006) suggest that the second model's countercurrent convection is unrealistic since the hydrate mass density is very similar to liquid water. Hence, lateral growth of the hydrate film should not displace the water in the front, but instead result in transformation of the water into hydrate almost at its location. Convection in the guest fluid should be small since the guest fluid has a far lower thermal conductivity than liquid water, and so would play no more than a minor role in heat removal.



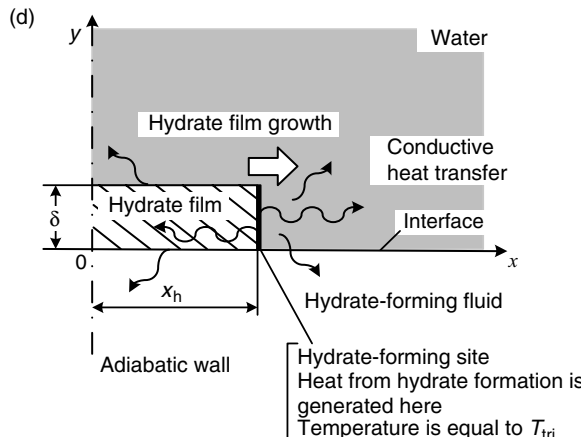
Hydrate film model by Uchida et al. (1999)



Hydrate film model by Mori (2001)



Hydrate film model by Freer et al. (2001)



Hydrate film model by Mochizuki and Mori (2006)

FIGURE 3.32 Physical models of hydrate film growth along the water–hydrate former fluid interface. (Reproduced from Mochizuki, T., Mori, Y.H., *J. Cryst. Growth*, **290**, 642 (2006). With permission from Elsevier.)

The Freer et al. (2001) model (Figure 3.32c) was based on experimental data on methane hydrate film growth at the methane–water interface. The v_f of the film was modeled assuming one-dimensional conductive heat transfer from the front of the film to the water phase extending beyond the front. As the computed v_f was much lower than that from experiment, Freer et al. (2001) suggested that hydrate film growth may be controlled by kinetics of hydrate formation. Mochizuki and Mori suggest that since the hydrate films are initially very thin, the fronts are probably convex contours with strong curvatures, rather than straight-edged.

In the most recent model by Mochizuki and Mori (2006), transient two-dimensional conductive heat transfer from the film front to both the water and guest fluid phases and the hydrate film itself is assumed (Figure 3.32d). In this model, as that in the model of Freer et al. the hydrate film is assumed to exist on the water side of the water–guest fluid interface. The hydrate film is assumed homogeneous from a macroscopic scale. Water and guest phases extend infinitely. Lateral hydrate film growth is assumed to be faster than film thickening/thinning. Hydrate forms only on the front of the hydrate film and the temperature of the front is maintained at the three-phase equilibrium temperature. No guest or water movement occurs, and the rate of heat removal from the front is balanced by the rate of heat generation by hydrate formation.

The linear growth rate of the hydrate film along the water/hydrocarbon (hydrate former fluid) interface, v_f ($= dx_h/dt$), is given in Equation 3.21:

$$\rho_h \delta \Delta h_H v_f = \int_0^\delta \left(\lambda_h \frac{\partial T}{\partial x} \Big|_{x=x_h-} - \lambda_w \frac{\partial T}{\partial x} \Big|_{x=x_h+} \right) dy \quad (3.21)$$

where δ = hydrate film thickness; $\partial T/\partial x|_{x=x_h-}$ and $\partial T/\partial x|_{x=x_h+}$ are the hydrate-side and water-side temperature gradients, respectively, at $x = x_h$ (i.e., the x position of the hydrate-film front); Δh_H = heat of hydrate formation per unit mass of hydrate; λ_h and λ_w = thermal conductivity of hydrate and water, respectively.

The interfacial temperature must be higher than the system temperature because the solid molecules have less energy than those in the liquid and dissolved gas, so that heat is released as the molecules transform from fluid to solid. The heat raises the interfacial temperature to its equilibrium value, where it is limited by second law considerations.

Mochizuki and Mori (2005, 2006) indicate that experimentally observed hydrate film growth is typically radial rather than linear. However, reasonable agreement was obtained between the calculated and experimental v_f values using either the straight front or the semicircular-front models. Also, though the heat release rate of the semicircular-front was smaller than the straight-front, for order-of-magnitude estimations of δ , the straight-front model was acceptable. The heat released from hydrate formation was also assumed to be released to the water and guest fluid via the water–hydrate film interface and guest fluid–hydrate film interface within a short distance (about 0.1 mm) from the film front. Heat is

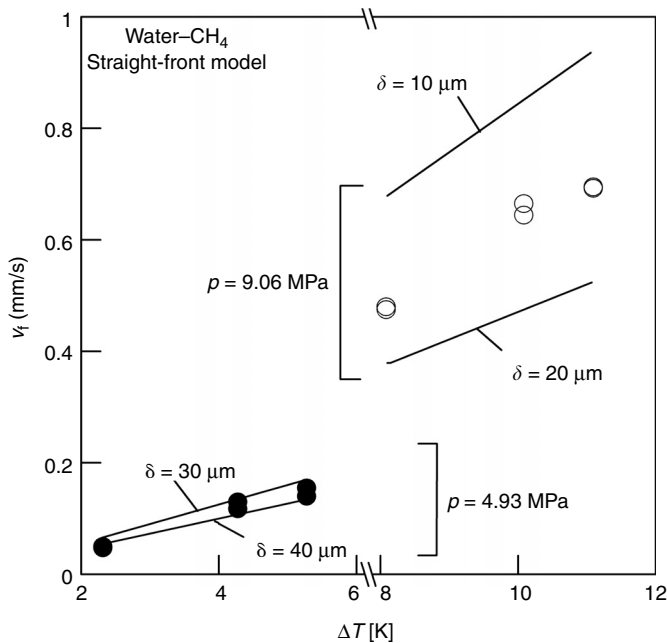


FIGURE 3.33 Comparison between calculated (lines by Mochizuki and Mori, 2006) and measured (points by Freer et al., 2001) hydrate film growth rates as a function of subcooling. (Reproduced from Mochizuki, T., Mori, Y.H., *J. Cryst. Growth*, **290**, 642 (2006). With permission from Elsevier.)

assumed to be directly transferred from the hydrate–water interface to the water phase, and transferred into the film and then diffused away into the water and guest fluid phases.

Comparison of the film growth rates calculated using the model by Mochizuki and Mori (2005, 2006) with experimental data by Freer et al. (2001) for methane hydrate is shown in Figure 3.33. The hydrate film thickness parameter, δ was fit to the experimental data. The δ values obtained from the model are within an order of magnitude agreement with experiment (Makogon et al., 1998; Taylor et al., 2006). However, the experiments suggest that the hydrate film thickness increases with increasing subcooling, which is the opposite trend to that suggested by the model.

Application of the planar hydrate film growth model to hydrate film growth on a water droplet was also tested by comparing Mochizuki and Mori's model (2006) with experiments by Uchida et al. (1999a) for carbon dioxide hydrate growth. The calculated and measured growth rates were again within an order of magnitude agreement. The film thickness obtained by fitting the model to the data was found to be significantly lower for carbon dioxide hydrate than methane hydrate. Mochizuki and Mori (2006) suggest that in the case of droplet conversion the limited system size in the experiment may have an effect on the results. That is, heat transfer from the film front to the surrounding liquid is around 1–3 mm, which is comparable

to the size of the water droplet. This may result in the film front being in close enough proximity to surfaces of the reactor cell to cause mechanical or thermal interactions between the surface and film front.

3.2.4 State-of-the-Art for Hydrate Growth

The state-of-the-art for hydrate growth may be summarized with only a few statements:

1. Hydrate growth data and modeling are more tenable than are nucleation phenomena. In particular, the growth data (after nucleation) appears to be linear for as much as 100 min in Englezos' data.
2. Any existing growth model has been shown to fit only the data on which its parameters were based. Most data were obtained in a high-pressure reactor and may not apply to formation rates in a pipeline. Limited flow loop data are available.
3. Most of the data on which the models are based are obtained for sI, while most pipeline hydrates are sII due to the propane (and higher) constituents of natural hydrocarbons.
4. Heat and mass transfer effects can be more significant than intrinsic kinetics in multiphase systems.
5. Metastable states can form during hydrate growth, which is not accounted for in the simulations or models.

3.3 HYDRATE DISSOCIATION

Hydrate dissociation is of key importance in gas production from natural hydrate reservoirs and in pipeline plug remediation. Hydrate dissociation is an endothermic process in which heat must be supplied externally to break the hydrogen bonds between water molecules and the van der Waals interaction forces between the guest and water molecules of the hydrate lattice to decompose the hydrate to water and gas (e.g., the methane hydrate heat of dissociation is 500 J/gm-water). The different methods that can be used to dissociate a hydrate plug (in the pipeline) or hydrate core (in oceanic or permafrost deposits) are: depressurization, thermal stimulation, thermodynamic inhibitor injection, or a combination of these methods. Thermal stimulation and depressurization have been well quantified using laboratory measurements and state-of-the-art models. [Chapter 7](#) describes the application of hydrate dissociation to gas evolution from a hydrate reservoir, while [Chapter 8](#) describes the industrial application of hydrate dissociation. Therefore in this section, discussion is limited to a brief review of the conceptual picture, correlations, and laboratory-scale phenomena of hydrate dissociation.

3.3.1 Conceptual Picture of Hydrate Dissociation

The modern conceptual picture of dissociation of a hydrate core/plug typically involves radial hydrate dissociation rather than the previously suggested axial

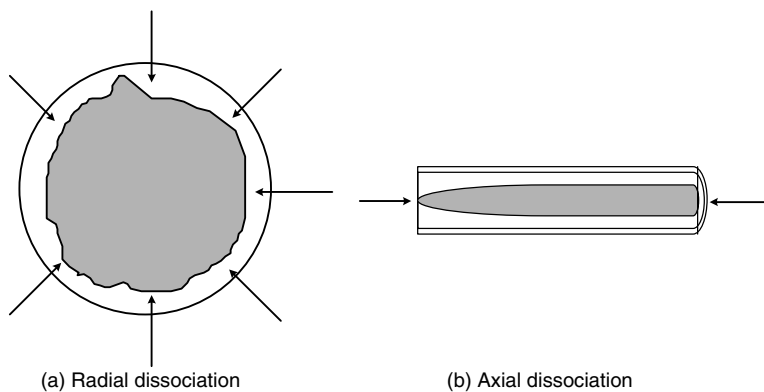


FIGURE 3.34 Current radial dissociation picture (a), compared to old axial dissociation picture (b).

hydrate dissociation (Figure 3.34). The most accurate picture is based on heat-transfer-limited hydrate dissociation, where the hydrate plug remains in the center of the pipe and is surrounded by a stationary water phase. This stationary water phase can conduct heat to the dissociating front of the hydrate (Davies et al., 2006). The nature of radial dissociation is a particularly fortuitous physical phenomenon since this leads to significantly more rapid hydrate plug dissociation than that for axial dissociation. This is due to (1) the radial plug dimensions being always smaller than the longitudinal dimensions and (2) the larger radial surface heat transfer area compared to the axial surface for heat transfer.

This radial dissociation model is supported by direct evidence obtained from x-ray computed tomography (CT) measurements of the dissociation of a methane hydrate core (Gupta, 2007). X-ray CT measurements capture images and density profiles of the hydrate core, showing that hydrate dissociates radially (Figure 3.35). At each time interval, different stages of radial dissociation of the hydrate plug were observed from the CT images, with the final step being water draining. No evidence of axial dissociation was observed (cf. Peters et al., 2000; Bollavaram and Sloan, 2002).

3.3.2 Correlations of Hydrate Dissociation

The different hydrate dissociation models that have been developed by various research groups are summarized in Table 7.10. The majority of these models are based on heat transfer limited dissociation. Some of the models have been developed to incorporate both heat transfer and kinetics.

On the basis of comparisons with experimental data on hydrate dissociation it has been shown by a number of research groups that heat transfer plays the dominant role in hydrate dissociation, rather than intrinsic kinetics (Moridis, 2002; Hong et al., 2003; Davies et al., 2006). This is analogous to studies showing that the ice melting process is controlled by heat transfer (Galwey and Brown, 2000). Hong et al. (2003) suggest that at the very early stage of hydrate dissociation, the

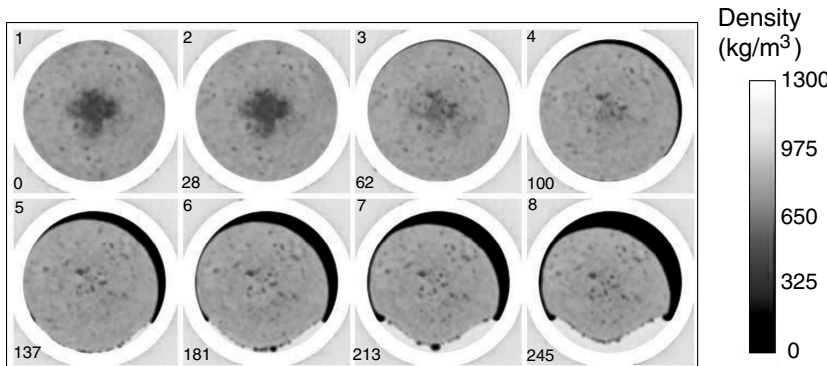


FIGURE 3.35 (See color insert following page 390.) X-ray CT imaging shows radial dissociation of a hydrate core. Image number 1–8 (top number on each image) recorded over 0–245 min (bottom number on each image). The cell pressure was decreased from 4.65 to 3.0 MPa over 248 min. The hydrate core temperature decreased from 277 to 274 K with time, following the three-phase methane hydrate equilibrium line. (From Gupta, A., *Methane Hydrate Dissociation Measurements and Modeling: The Role of Heat Transfer and Reaction Kinetics*, Ph.D. Thesis Colorado School of Mines, Golden, CO (2007). With permission.)

process can be controlled by intrinsic kinetics. Because heat is removed during decomposition, the temperature will quickly drop at the interface. Therefore, a temperature gradient is present in the hydrate zone, with heat being conducted from the hydrate zone to the interface. Hence, the dissociation process is controlled by heat transfer throughout the later stages.

From the extensive experimental and model development work performed at CSM (during a period of over 15 years), it has been demonstrated that a heat transfer controlled model is able to most accurately predict dissociation times (comparing to laboratory experiments) without any adjustable parameters. The current model (CSMPlug; see Appendix B for details and examples) is based on Fourier's Law of heat transfer in cylindrical coordinates for the water, ice, and hydrate layers, and is able to predict data for single- and two-sided depressurization, as well as for thermal stimulation using electrical heating (Davies et al., 2006). A heat transfer limited process is controlled by the rate of heat supplied to the system. Therefore, a measurable intermediate (cf. activated state) is not expected for heat transfer controlled dissociation (Gupta et al., 2006).

Rehder et al. (2004) measured the dissociation rates of methane and carbon dioxide hydrates in seawater during a seafloor experiment. The seafloor conditions provided constant temperature and pressure conditions, and enabled heat transfer limitations to be largely eliminated. Hydrate dissociation was caused by differences in concentration of the guest molecule in the hydrate surface and in the bulk solution. In this case, a solubility-controlled boundary layer model (mass transfer limited) was able to predict the dissociation data. The results showed that carbon dioxide hydrate dissociated much more rapidly than methane hydrate due to the higher solubility in water of carbon dioxide compared to methane.

Nuclear magnetic resonance studies of methane hydrate dissociation suggest that intrinsic kinetics is not likely to play a dominant role in the dissociation process (Gupta et al., 2006). Methane hydrate dissociation was shown to progress in the absence of an intermediate state (or activated state), with no preferential decay of large to small cavities. Similar measurements have been performed for Xe hydrate dissociation (Moudrakovski et al., 2001b).

3.3.3 Anomalous Self-Preservation

“Self-preservation” is the phenomenon where hydrates can remain stable for extended periods outside the hydrate stable region (Figure 3.36). Self-preservation or anomalous self-preservation has been experimentally observed by a numerous researchers (Davidson et al., 1986; Yakushev and Istomin, 1992; Stern et al., 2001a, 2001b, 2003; Takeya et al., 2002; Kuhs et al., 2005; Shimada et al., 2005). However, little is understood of this phenomenon. The ability to increase and prolong the stability of gas hydrates is desirable for gas storage applications.

As shown in Figure 3.36, the anomalous preservation region is observed over the temperature range 242–271 K on rapid depressurization to 0.1 MPa. This anomalous behavior has been also called “anomalous self-preservation.” The latter consists of a short rapid dissociation phase with a release of 5–20 vol%

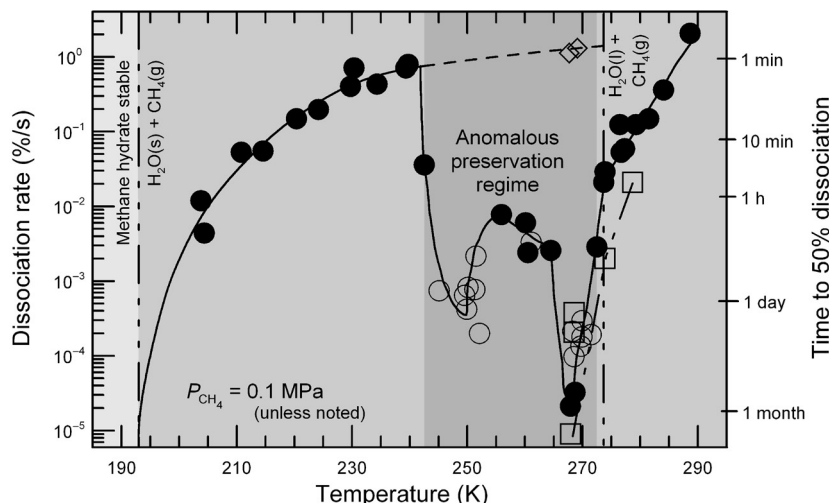


FIGURE 3.36 Average rates for methane hydrate samples reaching 50% dissociation at 0.1 MPa, following destabilization by rapid release of P . The anomalous preservation regime is between 242 and 271 K. Square symbols: experiments in which P is maintained at 2 MPa, Diamonds: 0.1 MPa rapid depressurization tests on sII methane–ethane hydrate, showing no comparable preservation behavior at 268 K. (Reproduced from Stern, L.A., Circone, S., Kirby, S.H., Durhan, W., *Can. J. Phys.*, **81**, 271 (2003). With permission from the National Research Council.)

of the total methane in the hydrate sample. During this gas release, adiabatic cooling of methane as well as general heat absorption occurs. After this rapid dissociation phase, the methane hydrate remains “metastably preserved” for up to 2–3 weeks depending on the dissociation temperature (Stern et al., 2003). Carbon dioxide hydrate (sI) also exhibits this anomalous self-preservation behavior (Stern et al., 2001a). Conversely, sII hydrates of ethane–methane (Stern et al., 2003) and propane (Stern et al., 2005) show no preservation effects.

The cause of the anomalous “self-preservation” behavior is not well-understood. Stern et al. (2003) acknowledge that ice-shielding could explain self-preservation of residual gas hydrate (<8%) in temperature-ramping tests and in low-temperature rapid-depressurization tests. However, they suggest such an ice protective rind cannot adequately explain anomalous preservation of methane hydrate at 242–271 K, particularly as sII hydrate does not exhibit anomalous preservation. Kuhs et al. (2005) suggest, from neutron diffraction and SEM data, that anomalous “self-preservation” could be due to significant annealing of ice stacking faults (ice defects) at around 240 K. They suggest that below 240 K, the ice covering the hydrate has gaps between ice crystallites, which allow gas diffusion.

3.3.4 State-of-the-Art for Hydrate Dissociation

The following summary statements are made about hydrate dissociation, based upon the previous subsections:

1. A hydrate plug or core dissociates radially, not axially.
2. X-ray CT provides a powerful means of imaging the hydrate core during the dissociation process, and obtaining real time density profiles of the core.
3. Hydrate dissociation is an endothermic process, typically controlled by heat transfer.
4. Using a heat transfer limited model based on Fourier’s Law in cylindrical coordinates (developed at the Colorado School of Mines), hydrate dissociation under field conditions provides an order of magnitude (higher) prediction, which is acceptable in the industrial setting (see [Chapter 8](#) and [Appendix B](#) for more details, including a description of CSMPPlug to determine dissociation dimensions and times).
5. Anomalous self-preservation stabilizes methane hydrate and carbon dioxide hydrate particles at atmospheric pressure at 242–271 K for up to 2–3 weeks. This phenomenon can have implications for natural gas storage.

3.4 SUMMARY

The time-dependent phenomena of hydrate nucleation and growth are challenging to both measure and model. This is in contrast to hydrate thermodynamics that

are well understood at typical industrial temperature and pressure conditions. The difficulties of measuring and correlating hydrate formation processes are largely because of the stochastic nature and apparatus dependence of the data. However, the state-of-the-art indicates that hydrate formation is controlled primarily by heat and mass transfer, with kinetics playing a more minor role in most cases. Hydrate decomposition on the other hand appears more tractable, and can be predicted in most cases using a heat transfer model. Sophisticated meso- and microscopic tools have been developed and applied to study the mechanisms of hydrate growth and decomposition.

REFERENCES

- Alexander, D.M., Hill, D.T., White, L.R., *Australian J. Chem.*, **24**, 1143 (1971).
- Angell, C.A., in *Water: A Comprehensive Treatise*, Vol. 7 (Franks, F., ed.) Plenum Press, New York, p. 1 (1982).
- Angell, C.A., *Ann. Rev. Phys. Chem.*, **34**, 593 (1983).
- Angell, C.A., *J. Phys. Chem. B*, **103**, 3977 (1999).
- Anklam, A.F., Firoozabadi, A., *J. Chem. Phys.*, **121**, 11867 (2004).
- Arjmandi, M., Ren, S., Tohidi, B., in *Proc. Fifth International Conference on Gas Hydrates*, Trondheim, Norway, June 13–16, Paper 4011 (2005a).
- Arjmandi, M., Tohidi, B., Danesh, A., Todd, A.C., *Chem. Eng. Sci.*, **60**, 1313 (2005b).
- Baez, L.A., Clancy, P., in *Proc. First International Conference on Gas Hydrates*, (Sloan, E.D., Happel, J., Hnatow, M.A., eds) *Ann. N.Y. Acad. Sci.*, **715**, 177 (1994).
- Bansal, V., *Kinetic Study of Clathrate Hydrates*, M.S. Thesis, Colorado School of Mines, Golden, CO (1994).
- Berg, W.F., *Proc. Roy. Soc. (London)*, **A164**, 79 (1938).
- Berthoud, A., *J. de Chim. Phys.*, **10**, 624 (1912).
- Bird, R.B., Stewart, W.E., Lightfoot, E.N., *Transport Phenomena*, Wiley & Sons Inc., New York, (1960).
- Bishnoi, P.R., Kalogerakis, N.E., Jeje, A.A., Dholabhai, P.D., Englezos, P., in *Final Report to Department of Energy, Mines, and Resources, Earth Physics Branch*, Ottawa, Ontario K1A 0X3, Canada, DSS File No.: 20SU.23235 (1986).
- Bishnoi, P.R., Saeger, R.B., Kalogerakis, N.E., Jeje, A.A., in *Annual Report to Department of Energy, Mines, and Resources, Earth Physics Branch*, Ottawa, Ontario K1A 0X3, Canada, pp. 20SU.23235 (1984–1985).
- Bollavarapu, P., Sloan, E.D., in *Proc. Fourth International Conference on Gas Hydrates*, Yokohama, Japan, May 19–23, 947 (2002).
- Bowler, K., Stadterman, L.L., Creek, J.L., Koh, C.A., Sloan, E.D., Dec, S.F., in *Proc. Fifth International Conference on Gas Hydrates*, Trondheim, Norway, June 13–16, Paper 5030 (2005).
- Bridgman, P.W., in *Proc. American Academy of Arts and Sciences*, **XLVII**, N13, 530 (1912).
- Buchanan, P., Soper, A.K., Westacott, R.E., Creek, J.L., Koh, C.A., *J. Chem. Phys.*, **123**, 164507 (2005).
- Bunn, C.W., *Discussions Faraday Soc.*, **5**, 132 (1949).
- Buanes, T., Kvamme, B., Svaldal, A., *J. Cryst. Growth*, **287**, 491 (2006).
- Carroll, J.J., *Phase Behavior in the System Water–Hydrogen Sulfide*, Ph.D. Thesis, University of Alberta, Edmonton, Canada (1990).

- Chen, S.H., Gallo, P., Scioritino, F., Tartaglia, P., *Supercooled Liquids—Advances and Novel Applications*, ACS, Washington DC, p. 264 (1997).
- Chen, T.-S., *A Molecular Dynamics Study of the Stability of Small Prenucleation Water Clusters*, Dissertation, U. Missouri-Rolla, University Microfilms No. 8108116, Ann Arbor, MI (1980).
- Christiansen, R.L., Sloan, E.D., in *Proc. First International Conference Natural Gas Hydrates*, (Sloan, E.D., Happel, J., Hnatow, M.A., eds) *Ann. N.Y. Acad. Sci.*, New Paltz, NY, June 13–16, 1993 (1994).
- Christiansen, R.L., Sloan, E.D., Jr., in *Proc. Annual Convention of Gas Processors Association*, San Antonio, Tx, **74**, 15 (1995).
- Cingotti, B., Sinquin, A., Pic, J.S., Herri, J.M., Cournil, M., in *Proc. SPE International Symposium on Oilfield Chemistry*, Houston, TX, Feb. 16–19, 549 (1999).
- Clarke, M., Bishnoi, P.R., *Chem. Eng. Sci.*, **55**, 4869 (2000).
- Clarke, M.A., Bishnoi, P.R., *Chem. Eng. Sci.*, **56**, 4715 (2001).
- Clarke, M.A., Bishnoi, P.R., *Chem. Eng. Sci.*, **60**, 695 (2005).
- Comini, G., Guidice, S.D., Saro, O., *Intl. J. Numer. Methods Eng.*, **30**, 697 (1990).
- Davidson, D.W., Garg, S.K., Gough, S.R., Handa, Y.P., Ratcliffe, C.I., Ripmeester, J.A., Tse, J.S., Lawson, W.F., *Geochim. Cosmochim. Acta*, **50**, 619 (1986).
- Davies, S.R., Selim, M.S., Sloan, E.D., Bollavarapu, P., Peters, D.J., *AIChE J.*, **52**, 4016 (2006).
- Debenedetti, P.G., *Metastable Liquids, Concepts and Principles*, Princeton University Press, Princeton, NJ (1996).
- Debenedetti, P.G., *J. Phys.: Condens. Matter*, **15**, R1669 (2003).
- Dholabhai, P.D., *Incipient Equilibrium Conditions for Methane Hydrate Formation in Aqueous Mixed Electrolyte Solutions*, M.Sc. Thesis, University of Calgary, Calgary (1989).
- Dholabhai, P.D., Kalogerakis, N., Bishnoi, P.R., *Can. J. Chem. Eng.*, **71**, 68 (1993).
- D’Orazio, L.A., Wood, R.H., *J. Phys. Chem.*, **67**, 1435 (1963).
- Dore, J., *Phys. World*, **1**, 25 (1988).
- Elwell, D., Scheel, H.J., *Crystal Growth from High Temperature Solutions*, Academic Press, London (Chapters 4–6), 273 (1975).
- Englezos, P., *A Model for the Formation Kinetics of Gas Hydrates from Methane, Ethane, and their Mixtures*, M.S. Thesis, University of Calgary, Alberta (1986).
- Englezos, P., *Rev. IFP*, **51**, 789 (1996).
- Englezos, P., Bishnoi, P.R., *Fluid Phase Equilib.*, **42**, 129 (1988).
- Englezos, P., Kalogerakis, N., Dholabhai, P.D., Bishnoi, P.R., *Chem. Eng. Sci.*, **42**, 2647 (1987a).
- Englezos, P., Kalogerakis, N., Dholabhai, P.D., Bishnoi, P.R., *Chem. Eng. Sci.*, **42**, 2659 (1987b).
- Errington, J.R., Debenedetti, P.G., *Nature*, **409**, 318 (2001).
- Frank, H.S., *Science*, **169**, 635 (1970).
- Frank, H.S., Evans, M.W., *J. Chem. Phys.*, **13**, 507 (1945).
- Frank, H.S., Franks, F., *J. Chem. Phys.*, **48**, 4746 (1968).
- Frank, H.S., Wen, W.Y., *Discussions Faraday Soc.*, **24**, 133 (1957).
- Franks, F., Reid, D.S., In *Water: A Comprehensive Treatise*, Vol. 2, Chapter 5 (Franks, F., ed.) Plenum Press, New York (1973).
- Franzese, G., Stanley, H.E., *J. Phys.: Condens. Matter*, **14**, 2201 (2002).
- Freer, E., Selim, M.S., Sloan, E.D., *Fluid Phase Equilib.*, **185**, 65 (2001).
- Fukumoto, K., Tobe, J.-I., Ohmura, R., Mori, Y.H., *AIChE J.*, **47**, 1899 (2001).

- Fujioka, Y., Takeuchi, K., Shindo, Y., Komiyama, H., *Intl. J. Energy Res.*, **19**, 765 (1994).
- Galwey, A.K., Brown, M.E., *J. Therm. Anal. Calorimetry*, **60**, 863 (2000).
- Glew, D.N., *Nature*, **195**, 698 (1962).
- Guo, G.-J., Zhang, Y.-G., Refson, K., *J. Chem. Phys.*, **413**, 415 (2005).
- Gupta, A., *Methane Hydrate Dissociation Measurements and Modeling: The Role of Heat Transfer and Reaction Kinetics*, Ph.D. Thesis, Colorado School of Mines, Golden, CO (2007).
- Gupta, A., Dec, S.F., Koh, C.A., Sloan, E.D., *J. Phys. Chem. C*, **111**, 2341 (2007).
- Henning, R.W., Schultz, A.J., Thieu, V., Halpern, Y., *J. Phys. Chem. A*, **104**, 5066 (2000).
- Himmelblau, D.M., *J. Phys. Chem.*, **63**, 1803 (1959).
- Hirai, S., Okazaki, K., Araki, N., Yoshimoto, K., Ito, H., Hijikata, K., *Energy Convers. Manag.*, **36**, 471 (1995).
- Hirai, S., Tabe, Y., Kamijo, S., Okazaki, K., *Therm. Sci. Eng.*, **8**, 1 (2000).
- Hirai, S., Sanda, H., *Am. Mineral.*, **89**, 1260 (2004).
- Holder, G.D., Angert, P.F., in *Proc. 57th SPE Annual Technical Conference and Exhibition*, New Orleans, September 26–29, pp. SPE 11105 (1982).
- Hong, H., Pooladi-Darvish, M., Bishnoi, P.R., *J. Can. Petrol. Technol.*, **42**, 45 (2003).
- Huo, Z., Freer, E., Lamar, M., Sannigrahi, B., Knauss, D.M., Sloan, E.D., *Chem. Eng. Sci.*, **56**, 4979 (2001).
- Ito, Y., Kamakura, R., Obi, S., Mori, Y., *Chem. Eng. Sci.*, **58**, 107 (2003).
- Jamaluddin, A.K.M., Kalogerakis, N., Bishnoi, P.R., *Can. J. Chem. Eng.*, **67**, 948 (1989).
- Kashchiev, D., Firoozabadi, A., *J. Cryst. Growth*, **241**, 220 (2002a).
- Kashchiev, D., Firoozabadi, A., *J. Cryst. Growth*, **243**, 476 (2002b).
- Kato, M., Iida, T., Mori, Y.H., *J. Fluid Mechanics*, **414**, 367 (2000).
- Kelland, M., Svartaas, T., Ovsthus, J., Namba, T., in *Proc. Gas Hydrates: Challenges for the Future* (Holder, G.D., Bishnoi, P.R., eds), *Ann. N.Y. Acad. Sci.*, **912**, 281 (2000).
- Kimuro, H., Yamaguchi, F., Ohtsubo, K., Kusayanagi, T., Morishita, M., *Energy Convers. Manag.*, **34**, 1089 (1993).
- Kini, R., Dec, S.F., Sloan, E.D., *J. Phys. Chem. A*, **108**, 9550 (2004).
- Koh, C.A., Savidge, J.L., Tang, C.C., *J. Phys. Chem.*, **100**, 6412 (1996).
- Koh, C.A., Wisbey, R.P., Wu, X.P., Westacott, R.E., Soper, A.K., *J. Chem. Phys.*, **113**, 6390 (2000).
- Kuhs, W.F., Genov, G., Staykova, D.K., Hansen, T., in *Proc. Fifth International Conference on Gas Hydrates*, Trondheim, Norway, June 13–16, Paper 1003 (2005).
- Kvamme, B., in *Proc. Second International Conference on Gas Hydrates*, Toulouse, France, June 2–6, p. 139 (1996).
- Larson, M.A., Garside, J., *Chem. Eng. Sci.*, **41**, 1285 (1986).
- Larson, R., Makogon, T., Knight, C., Sloan, E.D., in *Proc. Second International Conference on Gas Hydrates* (Monfort, J.P., ed.) Toulouse, France, June 2–6 (1996).
- Lederhos, J., *The Transferability of Hydrate Kinetic Inhibitor Results between Bench Scale Apparatuses and a Pilot Scale Flow Loop*, Ph.D. Thesis, Colorado School of Mines, Golden, CO (1996).
- Lederhos, J.P., Long, J.P., Sum, A., Christiansen, R.L., Sloan, E.D., *Chem. Eng. Sci.*, **51**, 1221 (1996).
- Lee, J.D., Susilo, R., Englezos, P., in *Proc. Fifth International Conference on Gas Hydrates*, Trondheim, Norway, June 13–16, Paper 1034 (2005).
- Long, J., *Gas Hydrate Formation Mechanism and Its Kinetic Inhibition*, Ph.D. Thesis, Colorado School of Mines, Golden, CO (1994).

- Long, J.P., Sloan, E.D., *Int. J. Thermophysics*, **17**, 1 (1996).
- Maini, B.B., Bishnoi, P.R., *Chem. Eng. Sci.*, **36**, 183 (1981).
- Makogon, Y.F., *Hydrates of Natural Gas*, Moscow, Nedra, Izdatelstro, PennWell Books, Tulsa, Oklahoma, p. 237 in Russian (1981 in English) (1974).
- Makogon, Y., Makogon, T., Holditch, S., in *Proc. Japan National Oil Conference*, 259, Tokyo, (1998).
- Malegaonkar, M.B., Dholabhai, P.D., Bishnoi, P.R., *Can. J. Chem. Eng.*, **75**, 1090 (1997).
- Masuda, Y., Fujinaga, G.A., Naganawa, S., Fujita, K., Hayashi, Y., in *Proc. Third International Conference on Gas Hydrates*, Salt Lake City, UT, July 18–22 (1999).
- Matsumoto, M., Saito, S., Ohmine, I., *Nature*, **416**, 409 (2002).
- Miers, H.A., Isaac, F., *Proc. Roy. Soc. (London)*, **A79**, 322 (1907).
- Miller, K.W., Hildebrand, J.H., *J. Am. Chem. Soc.*, **90**, 3001 (1968).
- Mochizuki, T., Mori, Y.H., In *Proc. Fifth International Conference on Gas Hydrates*, Trondheim, Norway, June 13–16, Paper 1009 (2005).
- Mochizuki, T., Mori, Y.H., *J. Cryst. Growth*, **290**, 642 (2006).
- Moon, C., Taylor, P.C., Rodger, P.M., *J. Am. Chem. Soc.*, **125**, 4706 (2003).
- Mori, Y.H., *Energy Convers. Manag.*, **39**, 1537 (1998).
- Mori, Y.H., *J. Cryst. Growth*, **223**, 206 (2001).
- Moridis, G.J., in *Proc. SPE Gas Technology Symposium*, Calgary, Alberta, April 30–May 2, p. 75691 (2002).
- Moudrakovski, I.L., McLaurin, G.E., Ratcliffe, C.I., Ripmeester, J.A., *J. Phys. Chem. B*, **108**, 17591 (2004).
- Moudrakovski, I.L., Ratcliffe, C.I., Ripmeester, J.A., *Angew. Chem. Intl. Ed.*, **40**, 3890 (2001a).
- Moudrakovski, I.L., Sanchez, A.A., Ratcliffe, C.I., Ripmeester, J.A., *J. Phys. Chem. B*, **105**, 12338 (2001b).
- Muller-Bongartz, B., Wildeman, T.R., E.D. Sloan, Jr., in *Proc. Second International Offshore and Polar Engineering Conference*, p. 628 (1992).
- Mullin, J.W., *Crystallization*, 3rd Edition, Butterworth-Heinemann, Oxford, U.K. (1993).
- Mullin, J.W., Jancic, S.J., *Trans. Chem. Eng.*, **57**, 188 (1979).
- Mullin, J.W., *Crystallization*, 4th Edition, Elsevier Science & Technology Books, Amsterdam (2001).
- Natarajan, V., *Thermodynamics and Nucleation Kinetics of Gas Hydrates*, Ph.D. Thesis, University of Calgary, Alberta (1993).
- Natarajan, V., Bishnoi, P.R., Kalogerakis, N., *Chem. Eng. Sci.*, **49**, 2075 (1994).
- Nemethy, G., Scheraga, H.A., *J. Chem. Phys.*, **36**, 3382 (1962).
- Nerheim, A.R., *Investigation of Gas Hydrate Formation Kinetics by Laser Light Scattering*, D. Ing. Thesis, Norwegian Institute of Technology, Trondheim, Norway (1993).
- Nerheim, A.R., Svartaaas, T.M., Samuelsen, E.J., in *Proc. Fourth International Offshore and Polar Engineering Conference*, Osaka, p. 323 (1994).
- Nernst, W., *Z. fur Physik. Chemie*, **47**, 52 (1904).
- Nesterov, A.N., Feklistov, V.V., *Instruments and Experimental Techniques* (Translation of *Pribory i Tekhnika Eksperimenta*), **42**, 265 (1999).
- Nojima, K., Mori, Y.H., in *Proc. Tenth International Heat Transfer Conference* (Hewitt, G.F., ed.) Brighton, UK, **3**, 377 (1994).
- Noyes, A.A., Whitney, W.R., *J. Am. Chem. Soc.*, **19**, 930 (1897).
- Ohmura, R., Kashiwazaki, S., Mori, Y.H., *J. Cryst. Growth*, **218**, 372 (2000).
- Ohmura, R., Shigetomi, T., Mori, Y.H., *J. Cryst. Growth*, **196**, 164 (1999).
- Ohmura, R., Ogawa, M., Yasuka, K., Mori, Y.J., *J. Phys. Chem. B*, **107**, 5289 (2003).

- Ostergaard, K.K., Tohidi, B., Burgass, R.W., Danesh, A., Todd, A.C., *J. Chem. Eng. Data*, **46**, 703 (2001).
- Ostwald, W., *Zeit. fur Physik Chemie*, **34**, 495 (1900).
- Ouar, H., Cha, S.B., Wildeman, T.R., Sloan, E.D., *Trans I Chem. E.*, **70A**, 48 (1992).
- Parent, J.S., *Investigations into Nucleation Behavior of the Clathrate Hydrates of Natural Gases*, M.Sc. Thesis, University of Calgary, Alberta (1993).
- Parent, J.S., Bishnoi, P., *Chem. Eng. Commun.*, **144**, 51 (1996).
- Pauling, L., *The Structure of Water*, Pergamon Press, New York, p. 1 (1959).
- Peters, D., Selim, S., Sloan, E., in *Proc. Challenges for the Future: Gas Hydrates* (Holder, G.D., Bishnoi, P.R., eds), *Ann. N.Y. Acad. Sci.*, **912**, 304 (2000).
- Poole, P.H., Sciortina, F., Essmann, U., Stanley, H.E., *Nature*, **360**, 324 (1993).
- Radhakrishnan, R., Trout, B.L., *J. Chem. Phys.*, **117**, 1786 (2002).
- Rahman, A., Stillinger, F.H., *J. Am. Chem. Soc.*, **95**, 7943 (1973).
- Rahman, A., Stillinger, F.H., *Phys. Rev. A*, **10**, 368 (1974).
- Rehder, G., Kirby, S., Durham, B., Stern, L., Peltzer, E.T., Pinkston, J., Brewer, P., *Geochimica Cosmochimica Acta*, **68**, 285 (2004).
- Rodger, M., in *Proc. Gas Hydrates: Challenges for the Future*, (Holder, G.D., Bishnoi, P.R., eds), *Ann. N.Y. Acad. Sci.*, **912**, 474 (2000).
- Roettov, L.R., Strobel, T.A., Koh, C.A., Sloan, E.D., *Fluid Phase Equilib.*, **247**, 84 (2006).
- Rowley, J.L., *Statistical Mechanics for Thermophysical Property Calculations*. Prentice-Hall, Englewood, NJ (1994).
- Salamatin, A.N., Hondoh, T., Uchida, T., Lipenkov, V.Y., *J. Cryst. Growth*, **193**, 197 (1998).
- Sastray, S., Debenedetti, P.G., Scioritino, F., Stanley, H.E., *Phys. Rev. Lett.*, **53**, 6144 (1996).
- Schicks, J.M., Naumann, R., Erzinger, J., Hester, K.C., Koh, C.A., Sloan, E.D., *J. Phys. Chem. B*, **110**, 11468 (2006).
- Schroeter, J.P., Kobayashi, R., Hildebrand, M.A., *Ind. Eng. Chem. Fundam.*, **22**, 361 (1983).
- Selleck, F.T., Carmichael, L.T., Sage, B.H., *Ind. Eng. Chem.*, **44**, 2219 (1952).
- Servio, P., Englezos, P., *AICHE J.*, **49**, 269 (2003a).
- Servio, P., Englezos, P., *Crystl. Growth Design*, **3**, 61 (2003b).
- Servio, P., Englezos, P., Bishnoi, P.R., in *Proc. Gas Hydrates: Challenges for the Future*, (Holder, G.D., Bishnoi, P.R., eds), *Ann. N.Y. Acad. Sci.*, **912**, 576 (2000).
- Shimada, W., Takeya, S., Kamata, Y., Uchida, T., Nagao, J., Ebinuma, T., Narita, H., *Proc. Fifth International Conference on Gas Hydrates*, Trondheim, Norway, June 13–16, Paper 1032 (2005).
- Shindo, Y., Lund, P.C., Fujioka, Y., Komiyama, H., *Int. J. Chemical Kinetics*, **25**, 777 (1993).
- Skovborg, P., Gas Hydrate Kinetics, Ph.D. Thesis, Institut for Kemiteknik, Danmarks Tekniske Højskole, Lyngby, Denmark (1993).
- Skovborg, P., Ng, H.J., Rasmussen, P., Mohn, U., *Chem. Eng. Sci.*, **48**, 445 (1992).
- Skovborg, P., Rasmussen, P., *Chem. Eng. Sci.*, **49**, 1131 (1994).
- Sloan, E.D., in *Proc. 69th Annual Gas Processors Convention*, Phoenix, 8 (1990).
- Sloan, E.D., Fleyfel, F., *AICHE J.*, **37**, 1281 (1991).
- Sloan, E.D., Subramanian, S., Matthews, P.N., Lederhos, J.P., Khokhar, A.A., *Ind. Eng. Chem. Res.*, **37**, 3124 (1998).
- Smelik, E.A., King, H.E., *Am. Mineral.*, **82**, 88 (1997).
- Sorensen, C.M., in *Proc. 12th Int. Conf. on Prop. of Water and Steam*, Orlando, FL, September (1994).
- Speedy, R.J., *J. Phys. Chem.*, **91**, 3354 (1987).

- Speedy, R.J., Madura, J.D., Jorgensen, W.L., *J. Phys. Chem.*, **91**, 909 (1987).
- Stanley, H.E., Coniglio, A., Havlin, S., Lee, J., Schwarzer, S., in *On Clusters and Clustering* (Reynolds, P.J., ed.) Elsevier, Amsterdam, pp. 345 (1993).
- Staykova, D.K., Kuhs, *J. Phys. Chem. B.*, **107**, 10299 (2003).
- Stern, L., Hogenboom, D.L., Durham, W.B., Kirby, S.H., Chou, I.M., *J. Phys. Chem.*, **102**, 2627 (1998).
- Stern, L.A., Circone, S., Kirby, S.H., Durham, W.B., *J. Phys. Chem. B.*, **105**, 1756 (2001a).
- Stern, L.A., Circone, S., Kirby, S.H., Durham, W.B., *Energy Fuels*, **15**, 499 (2001b).
- Stern, L.A., Circone, S., Kirby, S.H., Durham, W.B., *Can. J. Phys.*, **81**, 271 (2003).
- Stern, L., Circone, S., Kirby, S., Durham, W., in *Proc. Fifth International Conference on Gas Hydrates*, Trondheim, Norway, June 13–16, Paper 1046, 300 (2005).
- Stillinger, F.H., in *Water in Polymers*, Vol. 1 (Rowland, S.P., ed.) American Chemical Society, Washington DC, p. 11 (1980).
- Subramanian, S., *Measurements of Clathrate Hydrates Containing Methane and Ethane Using Raman Spectroscopy*, Ph.D. Thesis, Colorado School of Mines, Golden, CO (2000).
- Subramanian, S., Sloan, E.D., In *Proc. Gas Hydrates: Challenges for the Future*, 912 (Holder, G.D., Bishnoi, P.R., eds), *Ann. N.Y. Acad. Sci.*, **912**, 583 (2000).
- Sugaya, M., Mori, Y.H., *Chem. Eng. Sci.*, **51**, 3505 (1996).
- Svandal, A., Kvamme, B., Granasy, L., Pusztai, T., *J. Phase Equilib. Diffusion*, **26**, 534 (2005).
- Swaminathan, S., Harrison, S.W., Beveridge, D.L., *J. Am. Chem. Soc.*, **100**, 5705 (1978).
- Takeya, S., Ebinuma, T., Uchida, T., Nagao, J., Narita, H., *J. Crystal Growth*, **237**, 379 (2002).
- Takeya, S., Hori, A., Hondoh, T., Uchida, T., *J. Phys. Chem. B.*, **104**, 4164 (2000).
- Taylor, C.J., Adhesion Force between Hydrate Particles and Macroscopic Investigation of Hydrate Film Growth at the Hydrocarbon/Water Interface, Masters Thesis, Colorado School of Mines, Golden, CO (2006).
- Taylor, C.J., Dieker, L.D., Miller, K.T., Koh, C.A., Sloan, E.D., *J. Colloid Interface Sci.*, (2006).
- Tohidi, B., Anderson, R., Clennell, B., Burgass, R.W., Biderkab, A.-B., *Geology*, **29**, 867 (2001).
- Tohidi, B., Anderson, R., Clennell, B., Yang, J., Bashir, A., Burgass, R., in *Proc. Fourth International Conference on Gas Hydrates*, Yokohama, Japan, May 19–23, 761 (2002).
- Tohidi, B., Burgass, R.W., Danesh, A., Østergaard, K.K., Todd, A.C., in *Proc. Gas Hydrates: Challenges for the Future*, (Holder, G.D., Bishnoi, P.R., eds), *Ann. N.Y. Acad. Sci.*, **912**, 924 (2000).
- Topham, D.R., *Chem. Eng. Sci.*, **39**, 821 (1984).
- Truskett, T.M., Dill, K.A., *J. Chem. Phys.*, **117**, 5101 (2002).
- Tse, J.S., Klug, D.D., *J. Supramol. Chem.*, **2**, 467 (2002).
- Tsyplkin, G.G., in *Proc. Gas Hydrates: Challenges for the Future*, (Holder, G.D., Bishnoi, P.R., eds), *Ann. N.Y. Acad. Sci.*, **912**, 428 (2000).
- Turner, D., *Clathrate Hydrate Formation in Water-in-Oil Dispersions*, Ph.D. Thesis, Colorado School of Mines, Golden, CO (2005).
- Uchida, T., Ebinuma, T., Kawabata, J., Narita, H., *J. Cryst. Growth*, **204**, 348 (1999a).
- Uchida, T., Ebinuma, T., Mae, S., *Formation Rate Measurements of CO₂ Hydrate Film Formed at Liquid CO₂ Water Interface*, *Greenhouse Gas Control Technologies*, (Riemer, P., Eliasson, B., Wokaun, A., eds.) Elsevier, 1073 (1999b).

- Uchida, T., Ikeda, I.Y., Takeya, S., Ebinuma, T., Nagao, J., Narita, H., *J. Cryst. Growth*, **237–239**, 383 (2002).
- Udachin, K.A., Ratcliffe, C.I., Ripmeester, J.A., *J. Supramol. Chemistry*, **2**, 405 (2002).
- Valeton, J.J.P., *Zeit. fur Kristallog*, **59**, 483 (1924).
- Voller, V., Swaminathan, C.R., Thomas, B.G., *Int. J. Numer. Methods Eng.*, **30**, 875 (1990).
- Volmer, M., Weber, A., *Z. Phys. Chem. (Leipzig)*, **119**, 277 (1926).
- Vysniauskas, A., Bishnoi, P.R., *Chem. Eng. Sci.*, **38**, 1061 (1983).
- Walrafen, G.E., Chu, Y.C., *J. Phys. Chem.*, **99**, 10635 (1995).
- Walrafen, G.E., Yang, W.H., Chu, Y.C., *Supercooled Liquids*, **21**, 287 (1997).
- Westacott, R.E., Rodger, P.M., *J. Chem. Soc., Faraday Transactions*, **94**, 3421 (1998).
- Wetlaufer, D.B., Malik, S.K., Stoller, L., Coffin, R.L., *J. Am. Chem. Soc.*, **86**, 508 (1964).
- Wilson, P.W., Heneghan, A.F., Haymet, A.D.J., *Cryobiology*, **46**, 88 (2003).
- Wilson, P.W., Lester, D., Haymet, A.D.J., *Chem. Eng. Sci.*, **60**, 2937 (2005).
- Wyslouzil, B.E., Cheung, J.L., Wilemski, G., Strey, R., *Phys. Rev. Lett.*, **79**, 431 (1997).
- Yakushev, V.S., Istomin, V.A., in *Proc. Physics and Chemistry of Ice* (Maeno, N., Hondoh, T., eds) Hokkaido University Press, Sapporo, 136 (1992).
- Zachariassen, K.E., *Ice Nucleating Agents in Cold-Hardy Insects*, Springer-Verlag, Berlin (1982).